Synthesis of an Aircraft Featuring a Ducted-Fan Propulsive Empennage

N.H.M. van den Dungen

Technische Universiteit Delft

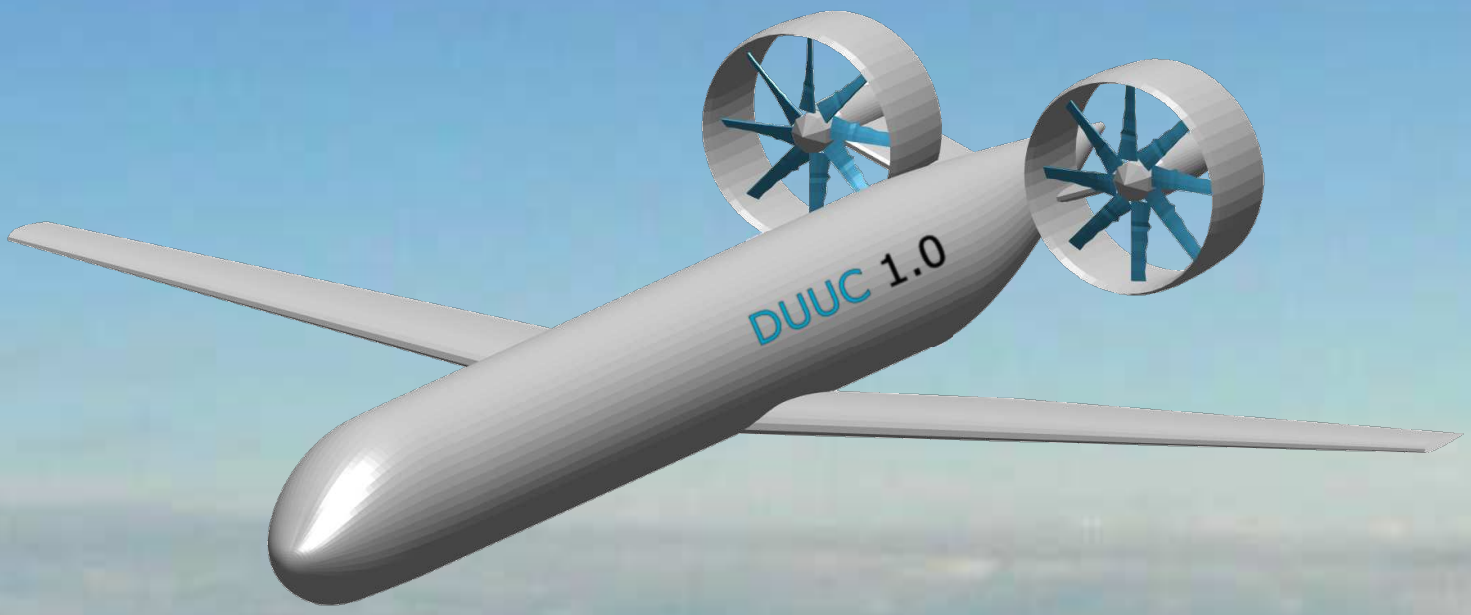

TU Delft Delft University of Technology

Challenge the future

SYNTHESIS OF AN AIRCRAFT FEATURING A DUCTED-FAN PROPULSIVE EMPENNAGE

by

N.H.M. van den Dungen

in partial fulfillment of the requirements for the degree of

Master of Science
in Aerospace Engineering

at the Delft University of Technology,
to be defended publicly on Tuesday April 18, 2017 at 13:00h.

Student number:	4133420		
Thesis registration nr:	156#17#MT#FPP		
Thesis committee:	Prof. dr. ir. L. L. M. Veldhuis	TU Delft	Head of department
	dr. ir. R. Vos	TU Delft	Supervisor
	dr. ir. S. Hartjes	TU Delft	External committee member
	ir. N. van Arnhem	TU Delft	Supervisor

TU Delft Delft University of Technology

PREFACE

The words written in this thesis belong to the last ones I ever put on paper as a Master student of the faculty of Aerospace Engineering at the Delft University of Technology. With the completion of this thesis, and therefore the Master track of Flight Performance & Propulsion, the years of struggling as a student will be over and the decades of working as an engineer will start.

I still remember the day I signed up for the thesis on the Delft University Unconventional Configuration, or simply called the DUUC. Back in November 2015 I was finishing my last month of internship at TUIfly Engineering, when I discovered the DUUC concept on the BlackBoard page while searching for possible thesis topics. By coincidence I met my to become thesis supervisor Roelof Vos on a Thursday morning on Delft Central Station, when I was about to take the train to Schiphol. After having a quick word, we were both convinced that my next challenge would consist of a one year research to an aircraft with a ducted-fan propulsive empennage. My first impression of the concept was: "where is the tail, and why are the engines located aft of the fuselage?" This first impression was a guideline throughout the thesis research and allowed me to be comprehensive and critical towards the findings I discovered in the past year.

At the end I believe that the biggest challenge of my last Master years, was not the fact that I only had a challenging thesis topic, but the combination of working on two complex projects within the same time frame. Shortly two months earlier before I devoted my thesis to the DUUC, my extracurricular activities at Delft Aerospace Rocket Engineering (DARE) took a new turn with the start of project Aether, a supersonic technology demonstrator for future DARE spaceflights featuring active aerodynamic stabilization and high-speed parachute deployment. At the end of the summer of 2015 about 30 motivated DARE students decided to combine their visions into the development of one large research rocket, and it became my duty as project manager to guide Aether and its students towards a successful flight.

The combined research of these two projects made the last year of the Aerospace Master the most difficult challenge I had to face so far. During the daytime I was trying to solve the integration and stability problems of the DUUC, and during the nighttime my team and I were solving the integration problems of a modular supersonic rocket design. Nevertheless, with the right clear engineering focus, dedication and motivation, and support from friends, family, and colleagues, I managed to complete the what seemed to be impossible. By quoting Walter D. Wintle: *"But sooner or later the man who wins is the one who thinks he can."*

The conceptual design of the DUUC was a tough study, in the sense that a large range of aeronautical disciplines had to be investigated, where a balance between detailed analysis and overall integration had to be maintained. And sometimes I found answers to research questions which were not the ones I hoped to find. However, in the end I really enjoyed working on conceptual aircraft design, because that is the main reason why I decided to study Aerospace Engineering in the first place.

First of all I would like to thank my supervisor Roelof Vos, who allowed me to work on the challenging topic of conceptual aircraft design, and who supported me throughout the entire thesis. His willingness to provide feedback on my work at any time has my greatest gratitude. Secondly I would like to thank the members of my graduation committee, Leo Veldhuis and Sander Hartjes, for the time they spent in assessing my work. I would like to thank Nando van Arnhem for his invaluable feedback on the DUUC concept, and the time he was willing to spent with me to solve in depth problems of the aircraft design. Furthermore I would like to thank Vikesh Harinarain, for our cooperation in the research to ducted-fan implementation in aircraft.

I would like to thank all my friends, for the support they gave me during the thesis, and for the fun we had besides all our hard study work. And last but not least, I would like to express my great gratitude towards my family, and especially my parents for the support they gave me throughout my entire studies in Delft.

N.H.M. van den Dungen
Delft, April, 2017

ABSTRACT

Research into more efficient and sustainable aircraft is a driving motivation for aircraft engineers to develop innovative concepts. The advanced conventional airliners of the present day still look similar to those developed in the early years of aviation. In search of revolutionary sustainable concepts, radical out-of-the box designs are being explored.

A thesis research is done to investigate the feasibility of the conceptual design of the Delft University Unconventional Configuration (DUUC), an aircraft featuring a ducted-fan propulsive empennage (DFPE). By integrating the propulsion system with a stabilizing ring-wing lifting surface and jet control vanes, a lighter and more fuel efficient design could be achieved. The main benefit of the ducted fan is an increased static thrust performance, where additionally the efficient ring-wing design contributes to the stability and balance of the aircraft. Secondary benefits include blade-containment protection and noise shielding. This thesis research focuses on ducted-fan system (DFS) performance estimation, propulsion system mass estimation, aircraft sizing for longitudinal static stability and balance, and aircraft performance comparison.

The Aircraft Design Initiator, a program designed to quickly synthesize realistic aircraft for initial performance studies of new concepts, is used to make models of the DUUC and a similar sized conventional reference aircraft. Once both aircraft are modeled within the Initiator, their performances are compared in terms of operational empty mass (OEM), maximum take-off mass (MTOM), fuel consumption, and aircraft drag, to study the effect of the DUUC concept on the overall aircraft design. Based on the operational velocity region of ducted fans and the previous research within the Initiator to turboprop aircraft, the ATR72-600 (high-wing, T-tail, turboprop) is chosen as reference aircraft. A significant update to the Initiator core was done such that the user has the freedom to design each of the following propulsion components individually: motor (gas-generator), centerbody, fan, nacelle (duct) and pylon.

The fan diameter is sized based on the fan rotational velocity, cruise Mach number, and maximum fan tip Mach number. Dividing the fan diameter by the duct aspect ratio yields the duct chord length. Combined with a predefined duct airfoil, fan-duct longitudinal offset, and fan-duct tip clearance, the total DFS geometry is determined. The pylon is sized such that it leaves a clearance between the duct and the fuselage. For the stability and balance calculations, the equivalent tail area results from the horizontal projected surface area of the duct and pylon. The pylon area inside the duct does not contribute to the tail area, only the area between the duct and the fuselage and the pylon area aft of the duct.

Aerodynamic properties of the DFPE are derived from a combination of existing empirical methods for planar wings (for the pylon) and ring-wings (for the duct). Based on windtunnel experiments thrust effects on the lift properties of the DFS are implemented, which increase both the lift gradient as the maximum lift coefficient. Because of unknown interactions between the duct, fan, centerbody, pylon, and jet vanes, it is assumed that the maximum lift coefficient of the entire DFPE is dominated by the DFS only. The geometries of the jet vanes are not sized, however their thrust-vectoring effects are included in the calculation of the lift coefficient, where it is assumed based on experimental windtunnel research that they will increase the lift with 20% for a maximum vane deflection.

A propeller analysis program is developed, which integrates unducted and ducted-fan analysis tools to perform propeller performance comparisons and a parametric ducted-fan design study. Analysis with the Ducted Fan Design Code (DFDC) tool indicates that a large duct aspect ratio is beneficial in terms of the propulsive efficiency. DFDC is implemented in the Initiator, however it is not active in calculating the propulsive efficiencies. The DFDC module requires a detailed design of the fan blade geometries and duct airfoil, to result in realistic output, e.g. thrust, torque, power. Because the fan blade geometry design module is being developed in parallel by another Initiator thesis, the DUUC fan geometry is chosen arbitrarily based on experimental research on ducted fan systems. The propulsive efficiencies of the DUUC are based on the Hamilton Standard F568 propeller installed on the ATR72-600, where it is assumed that the DFS has 10% higher take-off propulsive efficiency due to the increased static thrust performance.

The Initiator Class 2 Weight Estimation method is updated with the modified engine model. An additional component based weight estimation method for the duct is implemented. First of all, the aluminium duct shell thickness is based on the pressure vessel theory, which uses the static pressure and internal duct pressure. The internal duct pressure during maximum thrust at take-off is acquired with the DFDC module.

The duct shell mass scales with airfoil shape. Secondly, the thickness of a Kevlar blade containment liner is calculated in case of a blade release. The mass of the blade containment liner is about one order of magnitude lower than the duct shell mass. A weight correction factor of 1.5 is included to account for the structural reinforcements inside the duct and the jet vanes. The pylon mass is assumed to be 30% of its tip mass, which consists of the engine, centerbody, fan, and duct. Because the duct mass scales with the chord length and duct diameter, the pylon mass scales accordingly.

Sizing for longitudinal static stability and controllability (LSSC), where controllability refers to trimming, is identified as the crux of the DUUC concept. For minimum OEM the DFPE should be as small as possible, however for LSSC it is beneficial to have a certain tail area, to prevent that the DFPE generates too large downforces to maintain a balanced aircraft. Torenbeek's "X-Plot" method is modified, such that his equations can be used to determine the LSSC limits for the DUUC. Because the tail area of the DFPE is fixed by choosing the duct aspect ratio and fan diameter at the beginning of the aircraft design convergence, the DUUC can only modify the wing position to guarantee a stable and trimmable design. A wing-positioning diagram aids the aircraft designer to place the wing as much forward as possible, while complying to the LSSC requirements.

The trim drag of the DUUC is calculated based on the results of the trim diagram, where it is assumed that a linear relation between the tail-off lift and the tail downforce exists. It is assumed that the center of gravity (c.g.) shift during flight is within 1% of the mean aerodynamic chord (MAC), such that the tail arm does not change. By doing so, the forward c.g. location acquired from the aircraft loading diagram can be used to determine the moment arm of the DFPE. A superposition method is applied to combine the tail-off lift drag polar with the tail downforce and trim drag, to acquire the total trimmed aircraft lift-drag polar.

To prevent bookkeeping errors the following rule is maintained: *All DFPE properties which contribute in generating a downforce are booked under the horizontal stabilizer contributions, and all parameters which contribute in generating drag due to the fan frontal area are booked under the propulsion contributions.*

The ATR72-600 baseline model has -2.2% MTOM, -0.8% OEM, and -22.1% harmonic fuel mass, compared to the reference aircraft. The large discrepancy in the fuel mass is caused by an underestimation of the power loading, which is limited by the requirement to have a climb gradient of 2.1% after a balked landing with one engine out. With a higher required engine power, the engine mass increases. This effect is present for both the ATR72-600 and DUUC models, however the DUUC experiences a larger aft shifted OEM c.g.

Including the uncertainties in the DFPE weight estimation, the DUUC indicates that the MTOM varies from +5.8% to +20.2%, OEM varies from +9.1% to +31.8%, and harmonic fuel burn varies from +8.4% to +21.9%, with respect to the ATR72-600 Initiator model. Due to the heavy DFPE, the OEM increases. Therefore the engines need to be more powerful to lift-off the aircraft, which increases the aircraft mass in the next iteration in the design convergence. Secondly, the heavy DFPE shifts the c.g. far aft. This reduces the moment arm between the aerodynamic center (a.c.) of the DFPE and c.g., and therefore the DFPE needs to generate a larger downforce to keep the aircraft balanced during flight. The large downforce results in a large trim drag, which consequently increases the total fuel consumption. The a.c. of the tailless aircraft is located after the most forward c.g. location, due to the contributions of the fuselage shape and the frontal area of the fans.

A sensitivity analysis indicates that smaller ducts, by decreasing its chord or diameter, result in a lighter and more fuel efficient design. Unfortunately the decrement in duct size is limited by the stability and balance constraints, and manual checks are required to verify the feasibility of the wing-positioning design space. If the ducts become too small, the horizontal projected surface area is not big enough to generate a certain downforce, as such the aircraft becomes instable.

A sensitivity analysis of the take-off propulsive efficiency concludes that an increase in static thrust performance has marginal effect on the overall aircraft masses and fuel consumption. The take-off fuel saving is insignificant compared to the cruise phase fuel burn. Therefore the main performance benefit of the ducted fan, the increased static thrust performance compared to similar sized unducted propellers, is not significantly beneficial for the overall DUUC concept.

An "ideal" aircraft comparison with maximum propulsive efficiencies and "super-lightweight" duct design for both the ATR72-600 and DUUC models is performed. The ideal DUUC shows +5.1% MTOM, +7.8% OEM, +7.6% fuel consumption. This result indicates that the stated assumptions on DFPE propulsive performance and weight estimation do not change the overall outcome of the aircraft comparison.

The feasibility study to the DUUC concept shows that the heavy DFPE and large trim drag make it unlikely that a more fuel efficient and lighter design results compared to a similar sized conventional reference aircraft.

Contents

NOMENCLATURE

ACRONYMS

Abbreviation	Definition
AC	Aerodynamic Center
ADT	Actuator Disk Theory
BEM	Blade Element Method
BPR	Bypass Ratio
CG	Center of Gravity
CFD	Computational Fluid Dynamics
DFDC	Ducted Fan Design Code
DFPE	Ducted Fan Propulsive Empennage
DFS	Ducted Fan System
DUUC	Delft University Unconventional Configuration
FBD	Free Body Diagram
HSE	Horizontal Stability Estimation
KPI	Key Performance Indicator
LE	Leading Edge
LEMAC	Leading Edge of the Mean Aerodynamic Chord
LSSC	Longitudinal Static Stability & Controllability
MAC	Mean Aerodynamic Chord
MTOM	Maximum Take-Off Mass
OEI	One Engine Inoperative
OEM	Operational Empty Mass
PAP	Propeller Analysis Program
PWF	Propulsion Weight Factor
SM	Stability/Static Margin
TE	Trailing Edge
VTOL	Vertical Take-Off and Landing

SYMBOLS

Symbol	Description	Unit
a	Speed of sound	m/s
AR	Aspect ratio	-
AF	Activity Factor	-
$\bar{c}$	Mean Aerodynamic Chord	m
C_D	Drag coefficient	-
C_L	Lift coefficient	-
C_{L_α}	Lift gradient	1/rad
C_m	Moment coefficient	-
C_T	Thrust coefficient	-
C_P	Power coefficient	-
C_Y	Side force coefficient	-
D	Diameter	m
J	Advance Ratio	-
L, l	Length	m
M	Mach number	-
M	Bending moment	Nm
n	Revolutions per second	1/s
N	Normal force	N
N	Number of arbitrary components	-
P	Power	W
r	Radial distance	m
R	Blade radius	m
$\overline{R}$	Centroid fan radius	m
Re	Reynolds number	-
S	Surface area	m^2
V	Velocity	m/s
$\overline{V}$	Tail volume coefficient	-
W	Weight	lb, N
$\overline{x}$	Longitudinal location of an arbitrary point, normalized with the mean aerodynamic chord	-
$\overline{X}$	Longitudinal location of an arbitrary point, normalized with the fuselage length	-

GREEK SYMBOLS

Symbol	Description	Unit
α	Angle of attack	deg
β	Blade pitch angle	deg
	Side slip angle	deg
η	Efficiency	-
γ	Climb gradient	%
Λ	Sweep angle	deg
ω	Angular velocity	rad/s

SUB- & SUPERSCRIPTS

Symbol	Description
0	Parasite drag (in combination with C_D)
	Initial
0.75	At 75% of fan blade radius (in combination with β)
Al	Aluminium
bl	Blades
br	Brake
cb	Centerbody
con	Containment
crit	Critical
dyn	Dynamic
eng	Engine
f	Friction
H, h	Horizontal
i	Initial
	Induced
	Inner
Kev	Kevlar
kin	Kinetic
o	Outer
press	Pressure
proj	Projected
prop	Propulsive (in combination with η)
	Propeller
root	At the root
rw	Ring-wing
stall	At stall
stat	Static
tip	At the tip
TO	Take-Off
T-O	Tail-off
tr	Transition
tv	Thrust-vectoring
W	Wing
wet	Wetted
∞	Infinity
	Free-stream

List of Figures

List of Tables

1

INTRODUCTION

"Innovation in aircraft design to achieve more efficient and more sustainable air travel." This is the motivation which drives the aerospace industry of today in the development of new aircraft concepts. It goes without saying that for many decades aircraft designers are improving and inventing new concepts which contribute to this goal. In 2015 the Airbus A350-XWB, "the most modern and efficient aircraft" [1], entered service into the world of commercial aviation. This astonishing piece of engineering shows the product of decades of aircraft optimization, resulting in a fuel efficiency of ±14 grams of fuel per passenger per kilometer[1] [2]. However, if you compare the A350 to one of the first successful airliners; the Boeing-Douglas DC-3 (entered service in 1936, fuel efficiency of ±70 grams of fuel per passenger per kilometer [3]), or the first jet airliner; de Havilland Comet (entered service in 1952, fuel efficiency of ±80 grams of fuel per passenger per kilometer [4]), the looks of the commercial airliner did not change much over 80 years of development. Except for the fact that the aircraft engines are placed conveniently underneath the wings; the fuselage, wing, and tail still look the same as back in the early years of aviation.

In the exploration towards more efficient and sustainable aircraft designs, thinking outside of the box might result in revolutionary solutions. For this reason, the department of Flight Performance & Propulsion (FPP) at the Faculty of Aerospace Engineering of the Delft University of Technology recently invented a unique and unconventional aircraft design concept. The Delft University Unconventional Configuration (DUUC) features a ducted-fan propulsive empennage (DFPE), by means of replacing the conventional tail by two large ducted-fan systems (DFS). By integrating the propulsion system with a stabilizing ring-wing lifting surface and jet control vanes, a lighter and more fuel efficient design could be achieved. Additionally, this provides blade-containment protection and noise shielding.

Because removing the tail of the aircraft, the most critical system to keep an aircraft stable during flight, and replacing it with ducted fans, many questions could be raised concerning the design: "how will the aircraft be balanced?", "is the aircraft still stable?", "how heavy is the DFPE?", "how efficient are the ducted fans?", "is there a drag reduction by removing the tail?". To conclude, introducing a new aircraft concept is easier said than done. And therefore the first step in developing any new aircraft concept is to perform a baseline conceptual design study, where the aircraft is analyzed from the points of view of various aeronautical disciplines (aerodynamics, structures, stability/trimming, engine performance), such that in the end a conclusion can be made on the feasibility of the overall aircraft design.

Section 1.1 discusses the history of the application of DFS. The motivation, objective, and research goals of the thesis are provided in Section 1.4. The thesis scope and outline are discussed in Sections 1.5 and 1.6 respectively.

1.1. HISTORY OF DUCTED-FAN AIRCRAFT

The existence of the aircraft propeller is as old as the existence of motorized flight. With the success of the Wright Brothers in 1903 the airscrew, currently known as propeller, was born. Over the years which followed, more and more research is done towards this propulsion system to make them more efficient. Around the end of World War II, engineers came to the conclusion that the performance of a propeller at high speeds is

[1] For the calculations see Appendix A

limited because of the high sonic tip speeds which cause tip losses. This event led to the development of the turbojet engine, the ancestor of the advanced turbofans engines of the present day. [5]

The concept of ducted propellers, also known as ducted fans or shrouded propellers, already exists since the early days of aviation. The first known aircraft which featured such a system, was the Stipa Caproni (1932), see Figure 1.2(a). The idea behind this concept was that by placing the entire piston engine including propeller inside a converging-diverging tube-shaped fuselage, the airflow would accelerate throughout the tube based on the Venturi effect, which should give more thrust than without the tube. And indeed during the first test flights the airplane proved to lift-off faster then expected [6]. However, the ducted-fuselage also made the aircraft extremely stable, which deteriorated the maneuverability of the aircraft. Furthermore, the long duct added much wetted area, which drastically increased the profile drag and so the aircraft could not accelerate beyond 81mph [6].

Various studies are performed to the design and performance of DFS [7–14], and the main conclusion research has indicated is that the DFS showed to have a higher static thrust force compared to an unshrouded propeller of the same diameter and power loading. This could theoretically go up to 26% in static conditions, if the fan thrust is equal to the duct thrust [7]. Theoretical analysis shows that the presence of the duct reduces the slipstream contraction of the fan, which increases the mass flow through the fan [7], see Figure 1.1. Secondly, the accelerated inflow which occurs near the leading edge (LE) of the duct produces a pressure suction peak, which gives a forward thrust component on the duct. Although the thrust generated by the fan inside the duct is less than of an isolated propeller, the combination of both duct and fan thrust is higher than of an isolated propeller with the same diameter [7]. Furthermore, placing the propeller inside a duct reduces the tip induced drag of the propeller as it suppresses the vortex shedding [15]. This results in an unloading effect of the duct on the blades, which allows the fan to operate more efficient than without the duct. By minimizing the tip clearance, maximum thrust increase is achieved. [16] Because the design of the ducted fans proved to have many advantages, it inspired engineers to develop new ducted-fan aircraft concepts.

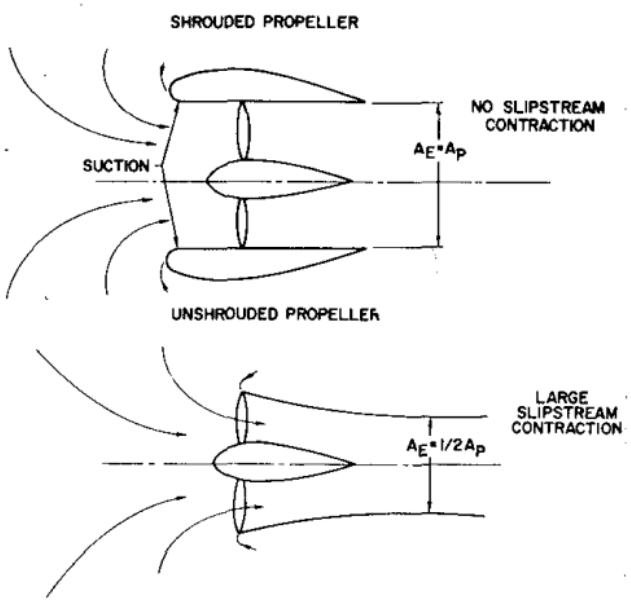

Figure 1.1: Momentum flow field comparison of shrouded and unshrouded propellers at static conditions [7] Smaller slip stream contraction is higher mass flow through the propeller disk, which results in higher thrust. A_P and A_E correspond to the cross sectional areas of the mass flow at the propeller, and the end of the slipstream, respectively

Unfortunately there are also downsides to the DFS. Although ducted fans have a higher static thrust than similar sized unshrouded propellers, at higher flight speeds ducted fans lose their advantage. For any propeller, the slip stream contraction decreases with flight speeds when the initial momentum is high. Since the duct is purposed the decrease the slipstream contraction anyways, this effect decreases with increasing airspeed [7]. Furthermore, for high cruise Mach numbers the duct inlet shape can cause losses in the propulsive efficiency [7].

Besides the increase in static thrust performance, one of the main secondary benefits of adding a duct to a propeller, is that it could improve the noise shielding. For conventional unshrouded propellers, the noise emitted from the source tends to go to the sides of the propeller [16, 17]. Therefore, implementing a duct should shield the noise emission to the sides. Although the addition of the duct might shield the noise to the sides, the interaction between the fan and the inner side of the duct might cause an increase in noise [14, 16, 17]. It is difficult to state what the direct noise benefits are for the ducted-fan concept, and therefore this is not easily implementable in the conceptual design stage.

Further research to fuselage mounded DFS is been investigated in the 1960s, for instance the XAZ-1 Marvelette, see Figure 1.2(b). This aircraft also featured control vanes inside the duct to provide pitch and yaw control. Another research program to vertical take-off and landing (VTOL) aircraft resulted in the development of the Bell X-22, see Figure 1.2(c). This aircraft features four DFS, which are able to rotate 90 degrees, such that they can be used in forward flight and VTOL. This aircraft formed the baseline for the Bell-Boeing V22 Osprey tilt-rotor aircraft[18]. Unfortunately the US military lost interest in this aircraft, even though the test program showed promising results [19].

Recent research by Airbus to hybrid-electric aircraft resulted into a successful prototype which has fully electric ducted fans, the E-Fan (2014) see Figure 1.2(d). Due to the higher thrust generation at low speed conditions, a ducted fan requires less engine shaft power than an open rotor propeller [20]. This makes ducted fan a good candidate for hybrid-electric propulsion, since the most electric engines are limited in shaft power compared to conventional turboprops [20]. Unfortunately it is not possible to easily upscale the hybrid-electric systems, due to the technical limitations in battery, electric engine, and power cables technology[20]. So therefore it is more favorable to use a conventional gasturbine for the DUUC.

History shows that various attempts are done to make successful aircraft which feature ducted fans. However, up until this day none of those aircraft solely used a tandem DFS as a horizontal and vertical stabilizer with control surfaces. That is why the ducted-fan propulsive empennage makes the DUUC an unique aircraft concept.

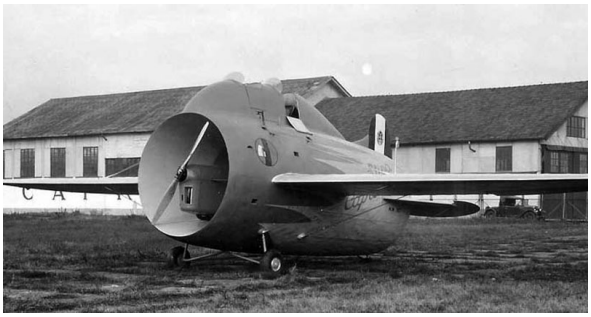

(a) Stipa Caproni (1932) [21]

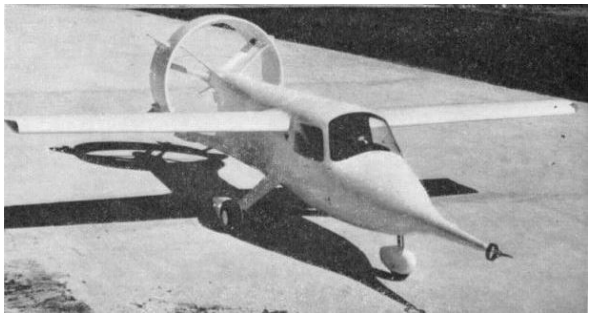

(b) XAZ-1 Marvelette (1962) [22]

(c) Bell X-22 (1966) [23]

(d) Airbus E-Fan (2014) [24]

Figure 1.2: Examples of ducted fan aircraft. The Airbus aircraft feature a hybrid-electric propulsion system

1.2. DEFINITION OF A DUCTED-FAN ENGINE

To introduce a basic, yet tricky topic, is to define what a ducted fan exactly is. To visualize the difficulty of characterizing a propulsion system as a DFS, three types of fan-based propulsion systems are depicted in

Figure 1.3. The most left image is the Rolls-Royce Trent XWB turbofan engine, "the world's most efficient large aero-engine" (Rolls-Royce plc. [25]), found on aircraft such as the Airbus A350. A more exotic variant on the turbofan is the propfan, which is an essence: "A turbine engine featuring contra rotating fan stages with aerodynamically advanced propellers, which allows operation at near-sonic free-stream Mach numbers." (Dungen, [20]) Most propfans are unducted, however Russian engineers developed an exotic variant of the propfan,; the NK-93, see Figure 1.3(b). And finally, there is the ducted fan such as the Dowty ducted fan, as installed on an experimental Britten-Norman Islander [26], see Figure 1.3(c). These three engines look similar because they all feature a large duct with a fan inside, but in performance and operating conditions they are definitely not the same.

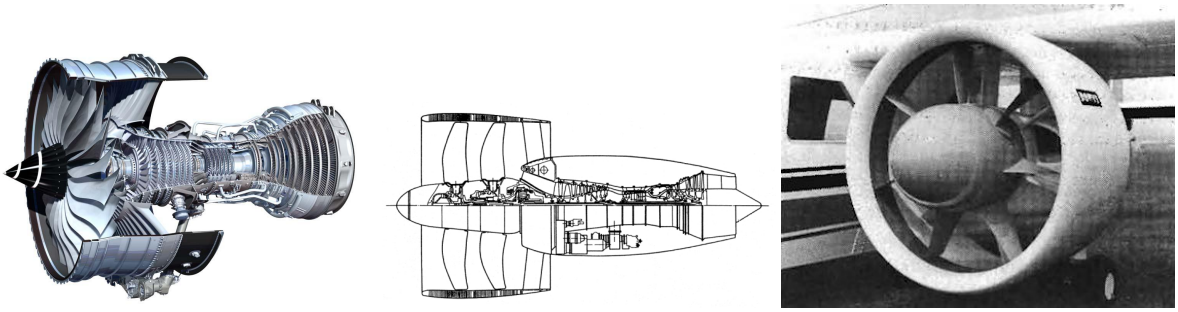

(a) Rolls-Royce Trent XWB Turbofan [27] (b) Kuznetsov NK-93 Propfan [28] (c) Dowty ducted fan [29]

Figure 1.3: Fan based engine types

One of the key elements which distinguish the engines in Figure 1.3 from each other, is the speed region in which they operate. Figure 1.4 shows in which Mach domains a certain type of engine is the most efficient to use. The figure indicates that most propellers are efficient at lower airspeeds, $M < 0.7$, and for the higher speeds a turbofan is preferred.

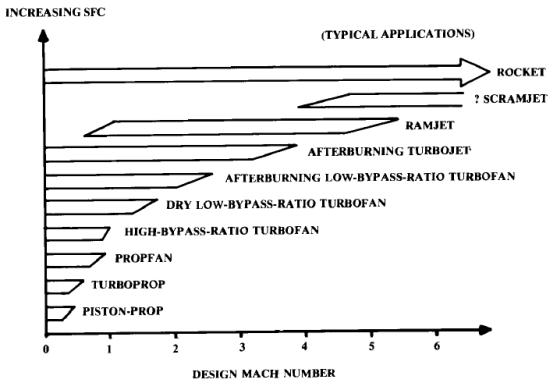

Figure 1.4: Propulsion system speed limits [30]

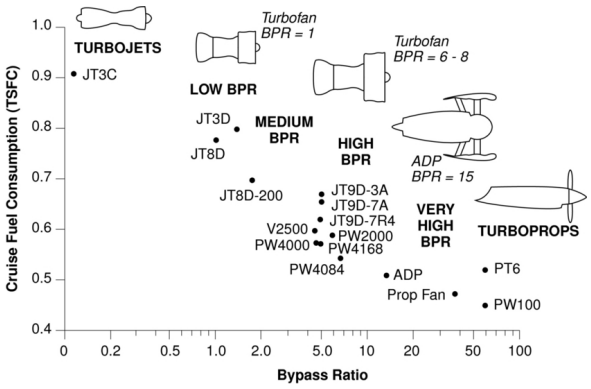

Figure 1.5: Trends in engine bypass ratio (Epstein, 1998) [31]

In general it is concluded that a propeller is more efficient in terms of propulsive efficiency compared to the turbofans, since it requires less energy in terms of fuel to accelerate a large air mass with a small velocity change, then to accelerate a smaller air mass with a higher velocity change [32]. Therefore it is more favorable to have an engine which has a large bypass ratio (BPR) [2], because it will result into more fuel efficient engines, see Figure 1.5. In contrary to a ducted fan, the propfan still has an engine core which accelerates the airflow in a similar way as a turbofan. "The design is intended to offer the speed and performance of a turbofan, with the fuel economy of a turboprop" (Sayed, [32])

In terms of geometry, ducted fans have the looks of both a conventional turboprop and a turbofan, however its performance is much more related to that of a turboprop. Bluntly said: *a ducted fan can be made by placing a duct around a standard turboprop engine*, see Figure 1.1.

[2] Bypass ratio is defined as the ratio between the airflow which goes around the engine core and the airflow which goes through the engine core. A high BPR indicates a large inlet fan cross sectional area.

1.3. AIRCRAFT DESIGN INITIATOR

The baseline concept of the DUUC is developed within the Aircraft Design Initiator development group, of the faculty of Aerospace Engineering at the department of Flight Performance & Propulsion (FPP). The Initiator is a conceptual aircraft design program, developed by FPP MSc graduate students [33, 34]. This program is purposed to synthesize realistic aircraft in a quick manner, to study the effect of new aircraft concepts. The Initiator combines empirical methods with physics-based models, to produce low order reliable results for both conventional as unconventional aircraft configurations.

The Initiator is written in MATLAB® [35], based on a modular, and object-oriented approach. This modular set-up of the Initiator allows to easily add and modify modules [33, 34]. Therefore, all equations, methods, and results presented in this thesis report are implemented and acquired via the Initiator.

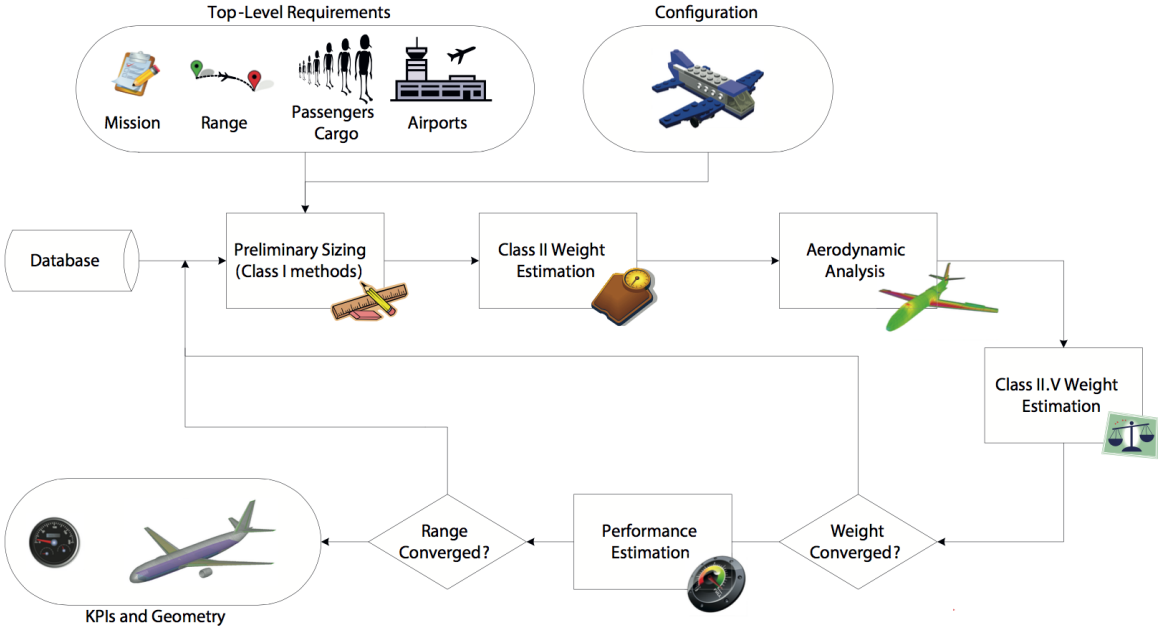

Figure 1.6: Overview of Initiator aircraft design process. [34]

During the thesis work various changes are done to the Initiator, either to improve the analysis of turboprop aircraft itself, and secondly to implement the DUUC concept. A mayor update to the core of the program was done to implement a more sophisticated engine model, such that the user is able to design the various components of the engine to model various types of engine architectures: turbofan, turboprop, ducted fan, electric motors, etc. A detailed overview of all relevant modifications done to the Initiator is provided in Appendix B.

1.4. RESEARCH OBJECTIVE

In contrary to the previously mentioned aircraft designs which used ducted fans, placing the propulsion system at the empennage will cause sizing difficulties with respect to the location of the center of gravity (c.g.), and thus also with respect to longitudinal static stability and controllability [3] (LSSC) of the aircraft. Therefore this specific aeronautical discipline is central for this thesis research.

When a new aircraft concept such as the DUUC is developed, it is good to compare its performance to similar sized reference aircraft with a conventional propulsion system and empennage. This should be done first of all to validate the results on the new concept, and secondly such an comparison is useful in determining how efficient the new concept is in a relative sense. Given the speed regimes of modern aircraft which use propellers and the vision to transport passengers over a longer distance with the DUUC, it is decided that the DUUC should be sized as a medium-range turboprop aircraft. Therefore it falls within the same category as the Fokker-50 [36] and ATR72-600[37].

[3] The term controllability refers to the ability of the aircraft to trim itself up to a state where it maintains a longitudinal moment balance.

Previous work on turboprop aircraft within the Initiator research group is done with the ATR72-600 as baseline aircraft [38, 39]. Because the Initiator input files for this aircraft were already available at the start of this thesis research, it was convenient to continue with this aircraft. Therefore the DUUC model as presented in this paper was sized with the same mission criteria and similar sizing rules as the ATR72-600 reference aircraft. In terms of the aircraft airworthiness regulations, the DUUC was sized according to the FAR-25 regulations [4].

The formulation of the main research objective follows from the technological gap between the currently existing aircraft, and an aircraft featuring a DFPE:

Research Objective

"The objective of this thesis is to investigate the feasibility of the conceptual aircraft design of the Delft University Unconventional Configuration, an aircraft featuring a ducted-fan propulsive empennage, by comparing its performance in terms of maximum take-off mass, operational empty mass, fuel consumption for the harmonic mission, and aircraft drag, with the conceptual design of a similar sized reference aircraft with a conventional propulsion system and empennage, both modeled with the FPP Aircraft Design Initiator, with a main focus on aircraft longitudinal static stability and balance."

From the research objective, the following research goals are defined:

Research Goals

1. Model a conventional turboprop reference aircraft in the Initiator
2. Model the DUUC aircraft in the Initiator
3. Perform a baseline aircraft comparison between the reference and DUUC aircraft
4. Perform a sensitivity study on the main DUUC design parameters

The key performance indicators which are used for the aircraft comparison are: maximum take-off mass (MTOM), operational empty mass (OEM), fuel consumption for the harmonic mission, and aircraft drag.

The research objectives lead to the following main research question:

Research Question

"What is the effect of the DUUC concept, an aircraft featuring a ducted-fan propulsive empennage, on the key performance indicators of the aircraft design, while providing sufficient longitudinal static stability and balance during flight?"

At the start of the thesis, the following research hypothesis were defined:

Research Hypothesis

1. The DUUC will have a lower OEM than a similar sized reference aircraft with a conventional propulsion system and conventional empennage
2. The DUUC will have a lower MTOM than a similar sized reference aircraft with a conventional propulsion system and conventional empennage
3. The DUUC will have a lower fuel consumption than a similar sized reference aircraft with a conventional propulsion system and conventional empennage
4. The DUUC will have a lower aircraft drag than a similar sized reference aircraft with a conventional propulsion system and conventional empennage

[4] FAR-25 airworthiness regulations are valid for transport aircraft with a minimum take-off mass of 5760kg [40, 41].

1.5. SCOPE OF THESIS

Given the available time for the thesis research, it is not possible to study all subsystems of the DUUC in great detail. This thesis study focuses on the conceptual design of an aircraft, which means that the details of the aircraft concept are limited to the Class II sizing rules[5] in addition of a more detailed structural analysis of the wing. Most methods are already implemented in the Initiator, see Figure 1.6, however for the DUUC the specific systems such as duct and pylon need to be sized.

A disadvantage of most Class II sizing methods is that assumptions and corrections factors are introduced to result feasible answers. Because these assumptions have their own uncertainty, it is convenient to perform a sensitivity study on the main DUUC uncertain parameters, to study their effect on the KPIs. Ideally in a detailed design stage of the DUUC design process the lower-order analysis methods can be replaced by higher-order methods, which will increase the accuracy of the final aircraft design.
The following topics are within the research scope of this thesis:

1. System implementation of the DFPE within the overall aircraft design in the Initiator
2. Class II Weight Estimation of DFPE propulsion system components
3. DFPE sizing for longitudinal static stability and controllability
4. Performance comparison of a conventional turboprop reference aircraft with the DUUC
5. Sensitivity analysis of various DUUC key design parameters, and their impact on the KPIs

The next list consists of items which are not explicitly investigated for this thesis research, however which are important for future research on the DUUC concept:

1. Aerodynamic analysis of the airflow inside and outside of a ducted fan
2. Structural analysis of the DFPE by using finite elements methods (FEM)
3. Aerodynamic interference effects of a tandem ducted-fan configuration
4. Aerodynamic interference effects between the DFPE and the fuselage
5. Propulsive performance analysis of a DFS by using computational fluid dynamics (CFD)
6. Propulsive performance of a DFPE with a non-uniform inflow
7. Noise analysis of the DFPE
8. Hybrid-electric propulsion system integration for the DUUC

Input on the aerodynamic analysis of the ducted fans is acquired via the thesis research of V. Harinarain [43]. During the research on the DUUC a close cooperation with Harinarain is done such that his findings, by means of performing analytical analysis and windtunnel experiments to ducted-fan performance, could directly be implemented for the DUUC sizing process in the Initiator. Harinarain's work presents more detailed explanation about the aerodynamic phenomena regarding ducted-fan performance, while this thesis focuses on the implementation of ducted fans into the overall aircraft design.

1.6. OUTLINE OF THESIS

This thesis starts with providing a theoretical background on the design and analysis of ducted and unducted fans in Chapter 2. Although this thesis focuses less on the detailed aerodynamic phenomena concerning the performances of a ducted fan system, it is essential to discuss the basics.

A propeller analysis program which is developed during the thesis to perform parametric studies to the DFS is presented in Chapter 3.

The propulsion mass estimation methods which are relevant for the DFPE are discussed in Chapter 4. This chapter mainly focuses on methods which are revised and added to the already existing ones of the Initiator.

The most important chapter about the DUUC sizing process is Chapter 5, where it is explained which methods are used to ensure that the DUUC is stable and balanced during flight. As it will turn out, this is the crux of the DUUC concept. Many results presented later on refer to the methods described in this chapter.

All results which are acquired during the thesis research are presented in Chapter 6. First of all, this includes the baseline development of the ATR72-600 and DUUC models. Secondly, the chapter contains an extensive sensitivity analysis to key DUUC design parameters, and to uncertain factors which are used during various sizing processes. The purpose of this chapter is to show how the DUUC design behaves in terms of its KPIs for various modifications to the design.

Finally, the conclusion and recommendations of this research are given in Chapter 7.

[5] Class II Sizing Methods as described by aircraft design handbooks such as Torenbeek [40], Raymer [30], and Roskam [42] focus on the sizing of general dimensions and masses of all mayor aircraft systems; wing, tail, fuselage, propulsion system, operational items, furnishing.

2

THEORY OF DUCTED AND UNDUCTED FANS

The theoretical background of this study is rooted in the research field of ducted/unducted propellers/fans and ring-wings, mainly in terms of propulsive and aerodynamic performance. First an overview of the relevant geometry definitions is provided, which is then followed by background information about the propeller performance analysis and DFS aerodynamic analysis.

2.1. DEFINITIONS

To start off with the background theory on ducted and unducted propellers, it is essential to understand the basic definitions which are being used in this thesis report. This section explains the various geometric models which are used, including the main propeller performance parameters.

2.1.1. SIZING OF THE DUCTED-FAN PROPULSIVE EMPENNAGE

Figure 2.1 depicts multiple sketches of the DFPE which are used within the Initiator. In the current configuration of the DUUC, the gasturbine is implemented in the centerbody inside the duct. The duct profile is axi-symmetric, and therefore uses a single airfoil. The geometries of the spinner and fan shown in the figure are chosen arbitrarily. The jet vanes are not modeled as geometries in the Initiator, however their aerodynamic effects are implemented where necessary. The part of the pylon which is located inside the duct does not contribute to $S_{\mathrm{H_{pylon}}}$.

The following definitions furthermore hold:

- Ducted Fan System (DFS): duct + fan + centerbody + gasturbine + control vanes
- Ducted Fan Propulsive Empennage (DFPE) : 2 × (DFS + pylon)

For the sake of clarity, propellers and fans are equivalent definitions. The same can be said for the terms duct, nacelle, and ring-wing.

One of the DFS key design parameters is the duct aspect ratio (AR_{duct}), which depends on the duct chord (c_{duct}, [m]) and fan diameter (D_{fan}, [m]):

$$AR_{\mathrm{duct}} = \frac{D_{\mathrm{fan}}}{c_{\mathrm{duct}}} \tag{2.1}$$

During the sizing process it is found that it is easier to use D_{fan} instead of D_{duct} to determine AR_{duct}, since the duct diameter depends on the airfoil thickness, fan position inside the duct, and tip clearance. Instead, for a given AR_{duct} and fan diameter, duct chord can be computed instantly.

The fan diameter is determined based on the maximum tip Mach number (M_{tip}), free-stream Mach number at cruise condition (M_{∞}), speed of sound (a, [m/s]), and design fan revolutions per second (n):

$$D_{\mathrm{fan}} = \frac{a}{\pi n}\sqrt{M_{\mathrm{tip}}^2 - M_{\infty}^2} \tag{2.2}$$

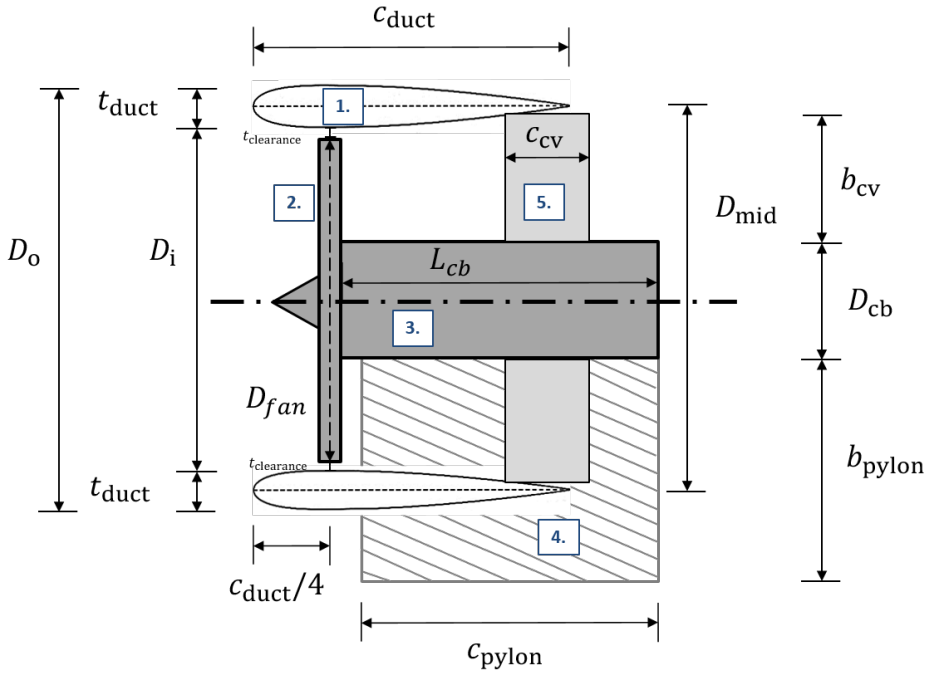

(a) Sketch of DFPE as modeled in the Initiator, including dimension indications. 1: duct (ring-wing airfoil), 2: fan including spinner, 3: centerbody including engine, 4: pylon, 5: control vanes.

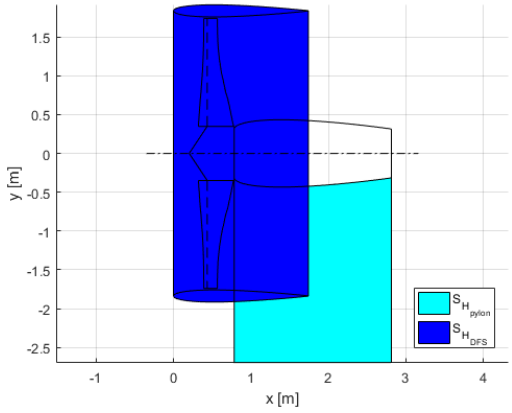

(b) Initiator model of DFPE, including horizontal projected surface areas, where $S_{\mathrm{H_{proj}}} = S_{H_{\mathrm{DFPE}}} = 2\left(S_{\mathrm{H_{DFS}}} + S_{H_{\mathrm{Pylon}}}\right)$

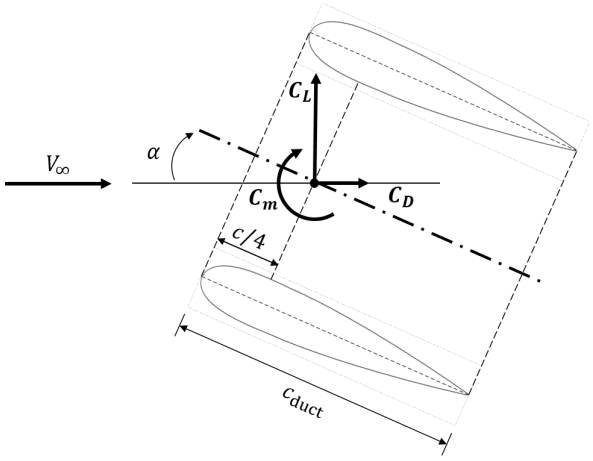

(c) Sketch of a ring-wing including aerodynamic forces and moments

Figure 2.1: Ducted fan propulsive empennage sketches and definitions. The sketches show half of the DFPE

The tip Mach number should ideally below $M = 1$ to prevent tip losses due to flow separation [44, 45]. For example, the Hamilton Standard F568 propellers which are installed on the ATR72-600, see Figure 2.2, operates at 1200RPM at a cruise Mach number of $M_\infty = 0.45$, and have $D_{\text{fan}} = 3.93$m. Equation (2.2) yields $M_{\text{tip}} = 0.916$. Because of the leading edge sweep angle (Λ_{LE}, [deg]) of the propeller blades, it is possible to operate at a higher tip Mach number, since the local Mach number on the tip airfoil tangential to the LE will be lower due to the swept wing rule [46]:

$$M = \cos(\Lambda_{\text{LE}}) M_\infty \tag{2.3}$$

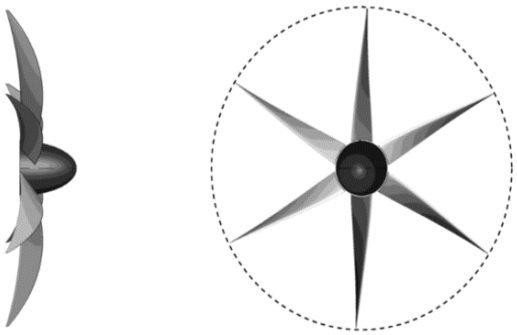

Figure 2.2: Model of the Hamilton Sundstrand F568, all composite propeller, which is installed on the ATR72-600. RPM = 1200, $D_{fan} = 3.93m$ [37, 47]

The maximum allowed tip Mach number is one of the many settings in the Initiator, which is often chosen arbitrarily by the aircraft designer based on reference values of similar sized propellers. As an example for the DUUC, the DFS installed on the Bell X-22 [48] researched by Mort et. al. [8], is taken for reference. This DFS has $D_{\text{fan}} = 2.13$m, with RPM = 2590, operating at 409km/h at a cruise altitude of 8500m, which gives $M_\infty = 0.37$. Combining this data with Equation (2.2), yields a fan tip Mach number of $M_{\text{tip}} = 1.01$. The calculation shows that the DFS on the Bell X-22 operates at a sonic fan-tip Mach number, however, aircraft design handbooks such as Ruijgrok [45] suggest to have $M_{\text{tip}} < 1$. Furthermore, a lower tip Mach number results in a smaller fan diameter, which results a smaller and therefore lighter duct design. Since it goes beyond the scope of this thesis to study the aerodynamic phenomena inside the duct in great detail, especially the interactions between the fan and the duct, it is assumed that the DUUC's DFS can operate at $M_{\text{tip}} = 0.99$. Because this assumption comes with an uncertainty, a sensitivity study presented in Chapter 6 is done where $M_{\text{tip}} = 0.99$ is varied for various DUUC models to investigate its impact on the aircraft KPIs.

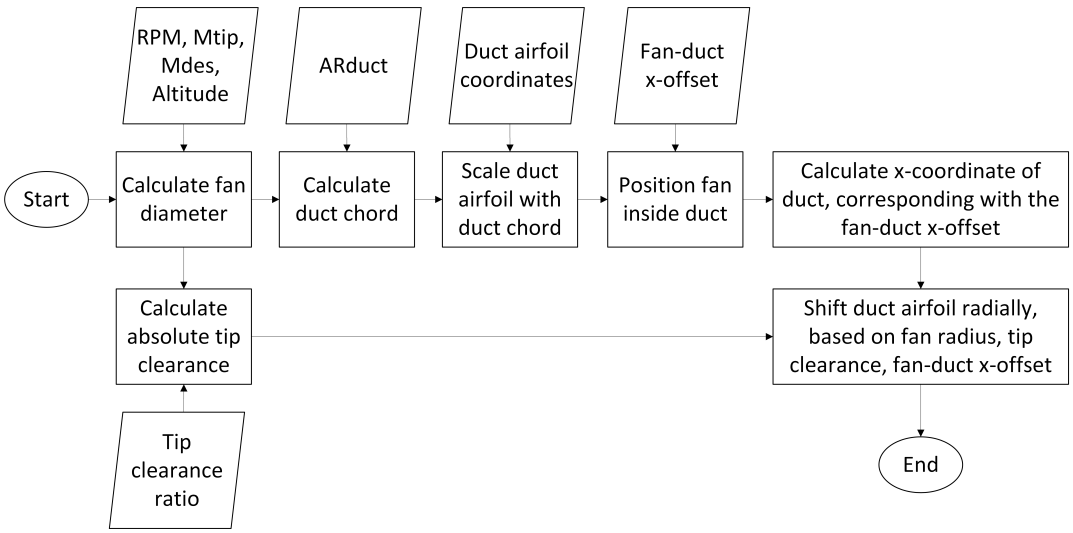

Figure 2.3: DUUC DFS sizing process. The squares indicated calculations (in the Initiator), the parallelograms represent input data (in the Initiator aircraft settings).

The combination of the fan RPM, M_{tip}, design Mach number (M_∞), AR_{duct}, $t_{clearance}$, fan-duct x-offset, and duct airfoil results the total geometry of the DFS, see Figure 2.3. Once the DFS geometry is created, the predefined engine location and fuselage geometry ensure that the correct pylon geometry is created, which connects the DFS to the fuselage. The DFPE is placed in such a way that the duct does not go more aft of the fuselage, to prevent that it scrapes the run-way during the take-off rotation and bulked landing.

Since M_{tip}, M_∞, $t_{clearance}$, and duct airfoil are fixed design parameters, the geometry of the DFS can be directly altered by varying the fan RPM and AR_{duct}. Therefore, these two values are the key design parameters which an aircraft designer can modify to size the DFS.

2.1.2. ADVANCE RATIO

An often used parameter in propeller theory is the advance ratio (J), which is used to describe the propeller performance at various flight conditions. The advance ratio describes the relation between the axial and tangential flow around a propeller. The tangential flow is represented by the number of blade revolutions per second (n) multiplied by the fan diameter (D_{fan}, [m]), and the axial flow is represented by the flight speed (V_∞, [m/s]) [40, 44, 45]:

$$J = \frac{V_\infty}{nD_{fan}} \tag{2.4}$$

For a fan with a certain diameter, the advance ratio can be varied via two manners; either by maintaining a constant airspeed with varying RPM, or by keeping the RPM constant and varying the airspeed.

2.1.3. ACTIVITY FACTOR

The activity factor (AF) represents the integrated power absorption capability of all propeller blade elements, which is a function of the blade area as the ratio of the area of the propeller disk [49]:

$$AF = N_{bl}\frac{1\cdot 10^5}{16}\int_{r_{hub}}^{r_{tip}} (c/D)(r/R)^3\, d(r/R) \tag{2.5}$$

By integrating the chord to diameter ratio of the fan blade (c/D) along the radius of the propeller normalized with the total fan radius (r/R), multiplied with a factor of $\frac{1\cdot 10^5}{16}$ and number of blades (N_{bl}), the total AF of the propeller is acquired.

2.1.4. PROPELLER PERFORMANCE COEFFICIENTS

To discuss the performance of propellers and DFS, such as thrust (T, [N]), torque (Q, [Nm]), power (P, [W]), and propulsive efficiency (η), it is required to define a set of performance coefficients which are applicable to both unducted and ducted fans. In propeller literature one can find various definitions, however not all of them are valid for both propellers as DFS. The following equations are used to describe the performance coefficients used in this report [45]:

$$C_T = \frac{T_{tot}}{\rho n^2 D_{fan}^4} \tag{2.6}$$

$$C_Q = \frac{Q}{\rho n^2 D_{fan}^5} \tag{2.7}$$

$$C_P = \frac{P}{\rho n^3 D_{fan}^5} \tag{2.8}$$

$$P = \omega Q \tag{2.9}$$

$$\eta = \frac{T_{tot}}{P} V_\infty \tag{2.10}$$

$$\eta = \frac{C_T}{C_P} J \tag{2.11}$$

The thrust coefficient in Equation (2.6) applies to the total thrust of the propeller or DFS. So in the case of the DFS $T_{tot} = T_{fan} + T_{duct}$. Furthermore, all performance coefficients are normalized with the free-stream air density (ρ, [kg/m^3]), revolutions per second (n), and fan diameter (D_{fan}, [m]). Multiplying the propeller shaft torque with its angular velocity (ω, [rad/s]), also results the shaft power, see Equation (2.9).

2.2. PROPELLER PERFORMANCE ANALYSIS

The main parameters to analyze the performances of a propeller, are the propulsive efficiency (η), and thrust and power coefficients, (C_T) and (C_P). These parameters are often found in the so called "propeller maps" or "carpet plots", where they are plotted for various blade pitch angles, ($\beta_{0.75}$, [deg], measured at 75% of the

blade radius), versus the advance ratio (J) [45]. An example of such a propeller performance map is given in Figure 2.4. Most modern propellers have a variable blade pitch, which means that for a constant RPM the correct blade pitch at each airspeed is chosen to operate at maximum propulsive efficiency [45].

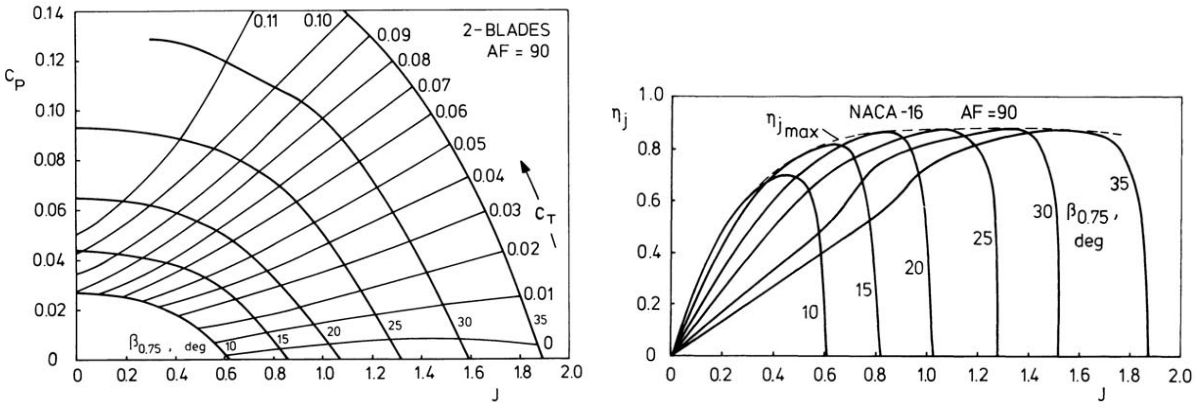

(a) Carpet plot

(b) Propulsive efficiency, indicated with η_j

Figure 2.4: Propeller performance of a NACA-16 2-bladed variable-pitch propeller [45]

2.2.1. ACTUATOR DISK THEORY

Originally the Initiator used the Actuator Disk Theory (ADT) to determine the propeller propulsive efficiency at a given flight velocity (V_∞, [m/s]):

$$\eta = \frac{2}{1+\sqrt{1+\frac{T}{\frac{1}{2}\rho\frac{\pi}{4}D_{\text{fan}}^2 V_\infty^2}}} \tag{2.12}$$

ADT is a low order propeller analysis method, which relies on the conservation of momentum theory [44, 50] . This theory basically states that a disk is placed inside an axial uniform flow which results in a uniform increase in total pressure and velocity along the disk radius, see Figure 2.5. The disadvantage of this method, is that it significantly simplifies the propeller model without taking into account the specific blade shape, nor the presence of a duct.

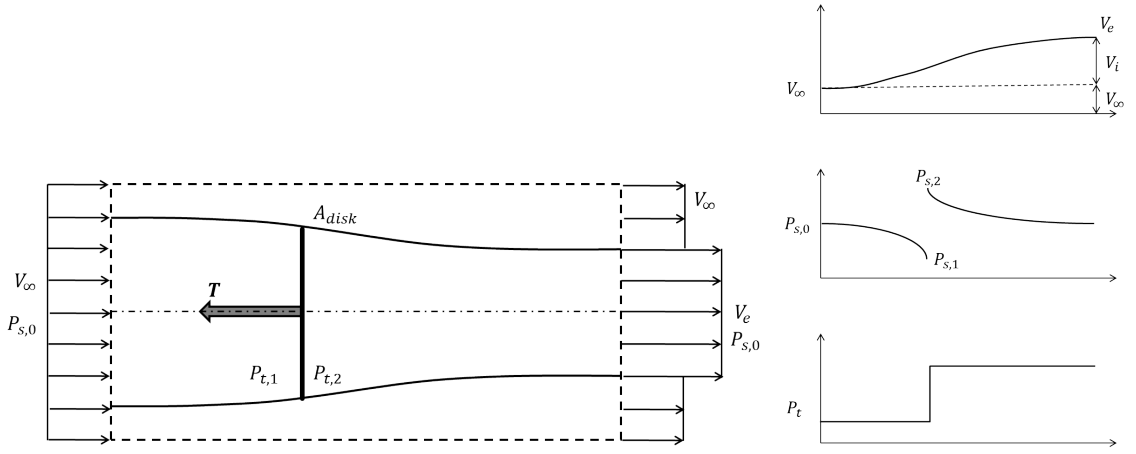

(a) Control volume, including steam tube visualization

(b) Axial velocity, static pressure, and total pressure propagation in the free-stream

Figure 2.5: Visualization of the actuator disk theory [51].
Pressures are indicated with P. Total pressure (P_t) and static pressure (P_{static}).

2.2.2. BLADE ELEMENT METHOD

In the blade element method (BEM), the propeller blade is discretized into a number of bladed elements including its local velocities and forces, see Figure 2.6.

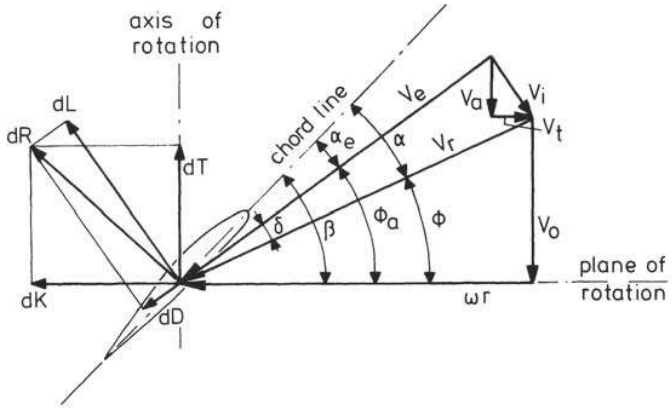

Figure 2.6: Schematic of propeller blade element, including relevant angles, velocities, and forces [45]

Then, for each of the sections a force balance, and balance of axial and angular momentum is performed. The resulting set of differential equations is solved in an iterative manner for each blade element, to compute the local lift (L), drag (D), torque (Q), thrust (T), and power (P) [44, 50, 52]:

$$dL = \frac{1}{2}\rho V_e^2 \cdot c(r) \cdot c_l \cdot dr \tag{2.13a}$$

$$dD = \frac{1}{2}\rho V_e^2 \cdot c(r) \cdot c_d \cdot dr \tag{2.13b}$$

$$dT = dL\cos\phi_a - dD\sin\phi_a \tag{2.13c}$$

$$dQ = r\left(dL\sin\phi_a + dD\cos\phi_a\right) \tag{2.13d}$$

$$dP = \omega r\left(dL\sin\phi_a + dD\cos\phi_a\right) \tag{2.13e}$$

A required input for these equations is the local lift and drag coefficients of the blade elements, c_l and c_d respectively. Once all blade elements are analyzed, the sum of the local torque and thrust values multiplied by the number of blades (N_{bl}) yields the total torque and thrust of the propeller [44, 50, 52]:

$$T = N_{bl}\int_{hub}^{tip} dT = N_{bl}\int_{hub}^{tip} \frac{1}{2}\rho V_e^2 c(r)\left(c_l\cos\phi_a - c_d\sin\phi_a\right)dr \tag{2.14a}$$

$$Q = N_{bl}\int_{hub}^{tip} dQ = N_{bl}\int_{hub}^{tip} r\frac{1}{2}\rho V_e^2 c(r)\left(c_l\sin\phi_a + c_d\cos\phi_a\right)dr \tag{2.14b}$$

$$P = N_{bl}\int_{hub}^{tip} dP = N_{bl}\int_{hub}^{tip} \omega r\frac{1}{2}\rho V_e^2 c(r)\left(c_l\sin\phi_a + c_d\cos\phi_a\right)dr \tag{2.14c}$$

The advantage of BEM over ADT is that this method is able to give a more accurate radial distribution of the increments in axial and tangential flow velocity, and total and static pressure. In the ADT the increment in tangential and radial flow velocity is constant along the radius as depicted in Figure 2.5(b), while in reality this is not the case due to the twist of the propeller blade [50], see Figure 2.7. Because the BEM includes the specific propeller blade shape and local blade lift and drag properties into account, it is considered as a more accurate propeller model then ADT.

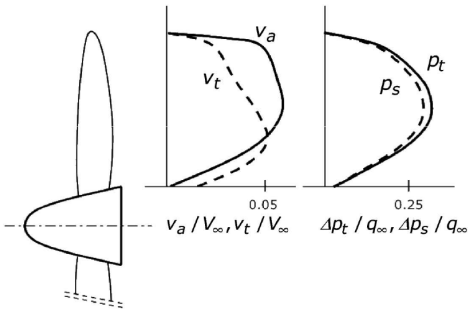

Figure 2.7: Typical radial distribution of axial velocity, tangential velocity, total pressure and static pressure directly behind a 6 bladed lightly loaded propeller; BEM analysis [50]

2.3. RING-WING & DUCTED FAN AERODYNAMICS

Next to the propulsive performances of a DFS, this system is also used as a stabilizing and trim surface. Because the fan inside the duct affects the airflow inside and outside of the duct, the lift and drag generation of the DFS is affected. In the next paragraphs, it is described which models are implemented in the Initiator to model the lift and drag of the DFPE.

2.3.1. RING-WING LIFT GENERATION

For tail sizing of conventional planar-wings, a DATCOM method is used to determine the lift gradient C_{L_α} of planar wings [42]:

$$C_{L_{\alpha_{\text{planar}}}} = \frac{C_{l_{\alpha_{2D}}} \cdot k \cdot AR}{2 + \sqrt{\frac{AR^2\left(1-M_\infty^2\right)}{k^2} \cdot \left[1 + \frac{\tan\left(\Lambda_{0.5_{\bar{c}}}\right)^2}{1-M_\infty^2}\right] + 4}} \tag{2.15}$$

$$\tan\left(\Lambda_{0.5\bar{c}}\right) = \tan\left(\Lambda_{\text{LE}}\right) - \frac{1}{AR} \cdot \frac{1-\lambda}{1+\lambda} \tag{2.16}$$

$$k = \begin{cases} 1 + \frac{(1.87 - 0.000233\Lambda_{\text{LE}})AR}{100} & \text{for } AR \leq 4 \\ 1 + \frac{[(8.2 - 2.3\Lambda_{\text{LE}}) - (0.22 - 0.153\Lambda_{\text{LE}})AR]}{100} & \text{for } AR > 4 \end{cases} \tag{2.17}$$

The maximum lift coefficient of planar wings is approximated with [40]:

$$C_{L_{\max_{\text{planar}}}} = 0.35 AR^{1/3} \tag{2.18}$$

Because the DATCOM method works for planar wings only, is not applicable for ring-wings and DFS. Research done by Werle[53] showed that the model by Weissinger gives the best results for the determination of the ring-wing lift gradient approximation:

$$C_{L_{\alpha_{\text{rw}}}} = C_{Y_{\beta_{\text{rw}}}} = \left(\frac{\pi}{2}\right) \zeta_{\text{rw}} C_{l_{\alpha_{2D}}} \tag{2.19}$$

$$\zeta_{\text{rw}} = \frac{1}{1 + \frac{\pi}{2AR} + \text{atan}\left(\frac{1.2}{AR}\right)\frac{1}{AR}} \tag{2.20}$$

For both the planar wing as the ring-wing it is assumed that the 2D lift gradient of the airfoil equals $C_{l_{\alpha_{2D}}} = 2\pi$, which is the approximated solution for an infinite wing [46]. For the same free-stream conditions and aspect ratio, a ring-wing will generate a higher C_{L_α} compared to an unswept and untapered planar wing. For instance, with AR=2, at $M_\infty = 0$, for an unswept and untapered planar wing, Equations (2.15 – 2.17) yield $C_{L_{\alpha_{\text{planar}}}}$=2.7, and Equations (2.19) and (2.20) yield $C_{L_{\alpha_{\text{rw}}}}$ =4.8.

Research done by Ribner [54] and Maqsood [55], see Figure 2.8, show the effect of increasing aspect ratio on the lift curve of the ring-wing. The figure furthermore includes the analytical approximations of the linear part of the lift curve, as computed with Equations (2.19) and (2.20). The comparison show that the analytical model given by Equations (2.19) and (2.20) approximate the experimental data sufficiently.

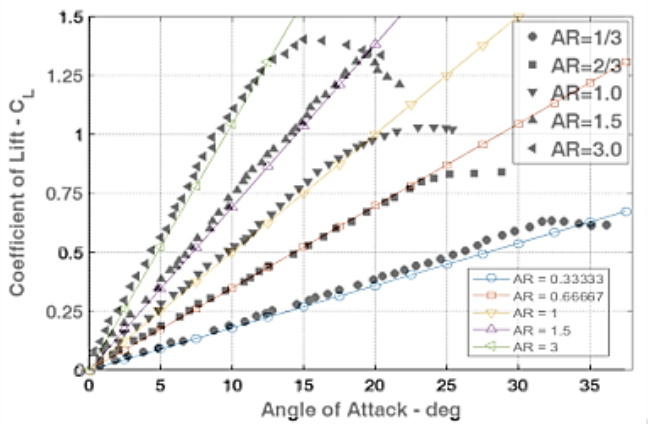

Figure 2.8: Effect of aspect ratio on the variation of lift coefficient for annular wings. Experimental (data-points) [55] versus analytical (lines) results based on Werle's model [53]

2.3.2. RING-WING AERODYNAMIC MOMENT

Werle furthermore also provides a method to determine the moment around the aerodynamic center of the ring-wing itself. However, for the aircraft LSSC calculations it is required to determine the aerodynamic moment of the ducted fan around the aerodynamic center (a.c.) of the entire aircraft, $C_{m_{\text{ac}_{\text{duct}}}}$, and therefore Werle's method is not sufficient.

Another manner to compute this parameter is given by Torenbeek, who states that the $C_{m_{\text{ac}_{\text{nacelles}}}}$ for the nacelles of all aircraft configurations with fan-based engines can be determined with [40]:

$$C_{m_{\text{ac}_{\text{nacelles}}}} = \begin{cases} -0.05 & \text{for } z_{\text{cg}} - z_{\text{engine}} \geq 0 \\ 0.02 & \text{for } z_{\text{cg}} - z_{\text{engine}} < 0 \end{cases} \tag{2.21}$$

Previously, Torenbeek's method is implemented in the Initiator for all aircraft which have turbofan engines. Although the origin of these values remains unclear in Torenbeek's handbook [40], it most likely refers to the frontal-area drag multiplied with the vertical offset between the engine centerline and the aircraft c.g. position ($z_{\text{cg}} - z_{\text{engine}}$), to acquire an aerodynamic moment around the aircraft a.c. Since these coefficients do not vary with the engine geometry, it is probable that they are determined based on a statistical analysis of various turbofan aircraft. Even though the duct design is axi-symmetric, meaning that the moment around its own a.c. is zero, it is decided to use Torenbeek's method to calculate $C_{m_{\text{ac}_{\text{nacelles}}}}$ for the DFPE, to include the effect of the moment induced by the frontal area of the fans into the tail-off pitching moment ($C_{m_{\text{ac}_{\text{T-O}}}}$).

2.3.3. DUCTED FAN: THRUST EFFECTS ON RING-WING

With the known aerodynamic performance of a ring-wing in terms of lift, the thrust-effects should be included to result the aerodynamic performance of a DFS. Experimental windtunnel research by Harinarain [43] showed that the lift gradient of a DFS can be approximated with the following equation, where $k = 0.20$:

$$C_{L_{\alpha_{\text{DFS}}}} = C_{L_{\alpha_{\text{rw}}}} (1 + k \cdot T_c) \tag{2.22}$$

The thrust coefficient T_c used in this equation is defined by:

$$T_c = \frac{T_{\text{tot}}}{\frac{1}{2}\rho V_\infty^2 S_{\text{H}_{\text{proj}}}} \tag{2.23}$$

Substituting this relation and $T_{\text{tot}} = \frac{\eta_{\text{prop}} P_{\text{TO}}}{V_\infty}$ results in:

$$C_{L_{\alpha_{\text{DFS}}}} = C_{L_{\alpha_{\text{rw}}}} \left(1 + k \cdot \frac{\eta_{\text{prop}} P_{\text{TO}}}{\frac{1}{2}\rho V_\infty^3 S_{\text{H}_{\text{proj}}}}\right) \tag{2.24}$$

An area-weighted average is used to include the contributions of the DFS and pylon to determine the total lift gradient of the DFPE, with $N_{\text{DFS}} = 2$ because the DFPE consists of 2×DFS:

$$C_{L_{\alpha_{\text{DFPE}}}} = \frac{N_{\text{DFS}} \left(C_{L_{\alpha_{\text{DFS}}}} S_{\text{H}_{\text{DFS}}} + C_{L_{\alpha_{\text{pylon}}}} S_{\text{H}_{\text{pylon}}}\right)}{S_{\text{H}_{\text{proj}}}} \tag{2.25}$$

The pylon lift gradient ($C_{L_{\alpha_{\text{pylon}}}}$) is calculated with Equation (2.15), because in essence it is a planar wing.

Harinarain's experimental research showed that the maximum lift coefficient of a DFS in idle mode results in $C_{L_{\max_{\text{DFS,idle}}}} = C_{L_{\max_{\text{rw}}}} \approx 2$, which corresponds to the maximum lift coefficient of a ring-wing [43]. Unfortunately during the thesis Harinarain's research was not able to determine the relation between AR_{duct} and $C_{L_{\max_{\text{rw}}}}$, so therefore the maximum lift coefficient of the DUUC's ring-wings is based on Harinarain's wind-tunnel experiments with AR_{duct}=2. The maximum thrust configuration can result in $C_{L_{\max_{\text{DFS}}}}$ which is almost 2.5 times higher than the maximum ring-wing lift. By implementing maximum deflection of the jet-vanes of the DFS, the lift could increase with $k_{\text{tv}} = 0.20$ [43]:

$$C_{L_{\max_{\text{rw}}}} \approx 2 \tag{2.26a}$$

$$C_{L_{\max_{\text{DFS}}}} \approx 2.5 C_{L_{\max_{\text{rw}}}} \tag{2.26b}$$

$$C_{L_{\max_{\text{DFS,tv}}}} \approx C_{L_{\max_{\text{DFS}}}} (1 + k_{\text{tv}}) \tag{2.26c}$$

The maximum lift coefficient of the DFS is difficult to estimate, as it is specific for each combination of fan, duct, pylon, and centerbody geometries. Furthermore, a significant part of the pylon is located inside the duct, where the aerodynamic interactions between the fan, duct, and pylon are unknown. Because of this unknown effects, it is uncertain how the pylon would contribute to $C_{L_{\max_{\text{DFPE}}}}$. Therefore it is chosen that for the DFPE downforce estimation, the contribution of the DFS is dominating and the effect of the pylon is neglected, such that $C_{L_{\max_{\text{DFPE}}}} \approx C_{L_{\max_{\text{DFS}}}}$.

To solve all uncertainties it is advised to implement a more detailed aerodynamic model of the ducted fan aerodynamics including installed jet vanes. Unfortunately, such a model was not available during the thesis research. Hence the assumptions stated in this section are based on a single wind-tunnel experiment.

2.3.4. DFPE PARASITE DRAG ESTIMATION

The drag of the DFPE consists out of two main parts, namely the parasitic drag and the lift induced drag [30]: $C_D = C_{D_0} + C_{D_i}$. The method to determine the lift induced drag (C_{D_i}) is explained in the section about the trim drag, given in Section 5.6. This section elaborates on the parasitic drag component (C_{D_0}).

The C_{D_0} of the DFPE is mainly generated by the surface friction of the duct and pylon. Because the geometries of the jet vanes are not sized in the Initiator, it is not certain how much parasite drag they will produce. Even more, it is not possible to determine with a lower-order method what the interaction of the airflow between the jet vanes, fan, centerbody, pylon, and duct is. Because of these reasons, it is decided assume that the parasite drag components for the fan, jet vanes, and centerbody are included in the propulsive efficiency.

For all nacelle objects within the Initiator, an empirical method given by Raymer [30] is used to calculate the C_{D_0}:

$$C_{D_0} = (C_f)\left(f_{L/D}\right)\left(f_M\right)\left(\frac{S_{\text{wet}}}{S_W}\right) \tag{2.27}$$

The pylon object uses the same empirical method as given by Equation (2.27), only then with pylon specific parameters. The wetted areas (S_{wet}, [m^2]) of the duct and pylon follow from the geometry estimation module in the Initiator. The pylon wetted area is based on the area which is located outside of the duct, see Figure 2.1(b). The skin friction coefficient (C_f) is calculated via Roskam's empirical estimation, which can be found for further reference in Appendix C. The slenderness coefficient ($f_{L/D}$) is calculated with [30]:

$$f_{L/D} = 1 + 0.35\left(\frac{L}{D}\right) \tag{2.28}$$

This equation uses the characteristic length (L, [m]) and diameter (D, [m]) of an arbitrary object. In case of the duct, the duct chord and outer duct diameter are used to calculate $f_{L/D}$. In case of the pylon the pylon chord and span are used to calculate $f_{L/D}$. The interface factor (f_M) is calculated with [30]:

$$f_M = 1 - 0.08 M_\infty^{1.45} \tag{2.29}$$

Once the C_{D_0} for the duct and pylon are calculated, the total parasite drag of the engine is calculated with $C_{D_{0_{\text{engine}}}} = C_{D_{0_{\text{duct}}}} + C_{D_{0_{\text{pylon}}}}$. These values can simply be added, because both are already normalized with the wing surface area S_W in Equation (2.27).

3

PROPELLER ANALYSIS PROGRAM

During the thesis research it was concluded that in order to have a good performance comparison between ducted and unducted propellers, a tool is needed which is capable of analyzing both propeller systems via similar analysis methods.

Programs exist to simulate unducted propellers (XROTOR)[56], and the ducted fans Ducted Fan Design Code (DFDC)[57]. However because each of these programs comes with its own structure of inputs and outputs, a quick exchange of data between the programs is not possible to allow for a comparison study on the performance of ducted and unducted fans.

This chapter explains about the Propeller Analysis Program (PAP), a MATLAB framework which is capable of analyzing both ducted as unducted propellers with similar propeller simulating tools, such as XROTOR and DFDC.

PAP is developed during the thesis research, first of all to quickly compare the performances of ducted and unducted propellers, and secondly to study the performance effects of the individual design parameters of ducted fans.

This chapter firstly discuss which tools are implemented in PAP, in Section 3.1. Secondly, the overall structure of the program is explained in Section 3.2, where more detailed program flow diagrams are provided in Appendix D. In Section 3.3 various results are presented which are acquired with PAP, to demonstrate its capabilities.

3.1. TOOLS

PAP includes the following tools to analyze ducted and unducted fans:

1. A Blade Element Method (BEM) developed by Prof. L.L.M. Veldhuis [50] → mainly for unducted propellers, but also includes correction for ducted propellers
2. Ducted Fan Design Code (DFDC) → for ducted fans only
3. XROTOR → for unducted propellers only

Furthermore, PAP includes XFOIL[58] to determine the 2D propeller blade airfoil properties. Since both XROTOR and DFDC are made by the same developers (M. Drela and H. Youngren) and both tools are based on the same aerodynamic methods [56, 57], it should be possible to study the relative performances of ducted and unducted propellers with these tools.

3.1.1. BEM

The first tool which is included in PAP, is a blade element code developed by Prof. L.L.M. Veldhuis [50]. The code itself is based on the blade element theory described in Section 2.2.2. To have BEM easily integrated within the structure of PAP, a couple of modifications had to be done:

1. Use various airfoils along the propeller radius.
2. Include XFOIL to make lift-polar per airfoil section.
3. Removed Prandtl-Glauert Mach correction, as XFOIL already uses a Karman-Tsien Mach correction to determine the blade element lift and drag coefficients [58].

4. Adapted variable pitch such that the $\beta(r)$ is varied according to the required $\beta_{0.75}$. while taking the $\beta_{0.75_{des}}$ into account.
5. Make sure that the tip radial location is slightly below $r/R = 1.00$, for example $r/R = 0.999$. This definition will prevent singularity errors when the Prandtl tip loss factor is implemented. This factor has a theoretical value of zero at the tip, however when this factor is used in square roots and numerators, this results in infinitely large numbers when $f = 0$.
6. Propeller area was initially defined as $S = \pi R^2_{\text{prop}}$, which does not take the hub area into account in contrary to XROTOR and DFDC. This is now modified according to $S = \pi(R^2_{\text{prop}} - R^2_{\text{hub}})$.

3.1.2. XROTOR

"XROTOR is an interactive program for the design and analysis of ducted and free-tip propellers and windmills" [56] XROTOR includes the following solving methods, which can be chosen individually per analysis run with PAP:

1. `GRAD`: Graded Momentum formulation
2. `POT`: Potential (Goldstein) formulation
3. `VRTX`: Discrete Vortex Wake formulation

These solving methods are presented in order of accuracy and computational time. The Graded Momentum formulation is the fastest method, however the Goldstein formulation gives a higher accuracy but also increases the computational time [56]. The discrete vortex wake formulation is mainly used for advanced propeller geometries, such as swept leading edge (LE) propellers [56]. Therefore this method also has the longest computational time. By default, XROTOR uses the Goldstein formulation. The user is however allowed to choose the preferred analysis method in PAP.

3.1.3. DFDC

DFDC is a tool used for axi-symmetric analysis and design of ducted rotors. The solving method is based on a lifting-line representation of the rotor blade together with an axi-symmetric panel representation of the duct and centerbody [57]. DFDC is derived from XROTOR, which combines classical propeller theory with simple models to simulate the presence of the duct and centerbody.

An example of a DFDC analysis is presented in Figure 3.1. In the bottom of the window, the axi-symmetric representation of the DFS is given including the grid layout. In the top of the window, the pressure distribution along the various surfaces is shown. The color indication of the pressure distribution corresponds with the color indication of the DFS. Hence, the orange pressure distribution correspond to the duct (off course, when this documented is printed in greyscale this cannot be seen in the figure).

After a single analysis, the program returns the axial forces generated by the propeller, duct, and centerbody. The duct will generate some force in the forward direction, hence thrust, due to the fact that there occurs a suction peak at the LE of the duct. The centerbody will mainly produce drag. A visualization of this effect is shown in Figure 3.2.

By default, DFDC runs an inviscid analysis, which therefore neglects the viscous drag of the duct and centerbody. The benefit of this setting, is that a single computation is relatively fast ≈5sec, while a viscous analysis could take up to ≈30sec The disadvantage, is that the viscous drag of the duct and centerbody are therefore neglected, so the total thrust is overestimated. However, for quick conceptual design of ducted fan systems it is acceptable to neglect the viscous effects. In terms of conceptual design, it is more valuable to study the relative effects on the propulsive performance by modifying the duct design parameters, then to determine the propulsive performance per DFS in great detail.

3.2. STRUCTURE

PAP includes the following main analysis protocols:

1. Ideal propeller performance, based on Durand Actuator Disk Theory [59]
2. `SingleAnalysis`: point analysis with the fan system, for one set of manual input free-stream conditions
3. `MultiAnalysis`: analysis for a range of advance ratios, where one of the fan system design parameters is modified
4. `MapAnalysis`: similar to `MultiAnalysis`, only the fan system design parameter which is modified is the blade pitch $\beta_{0.75}$

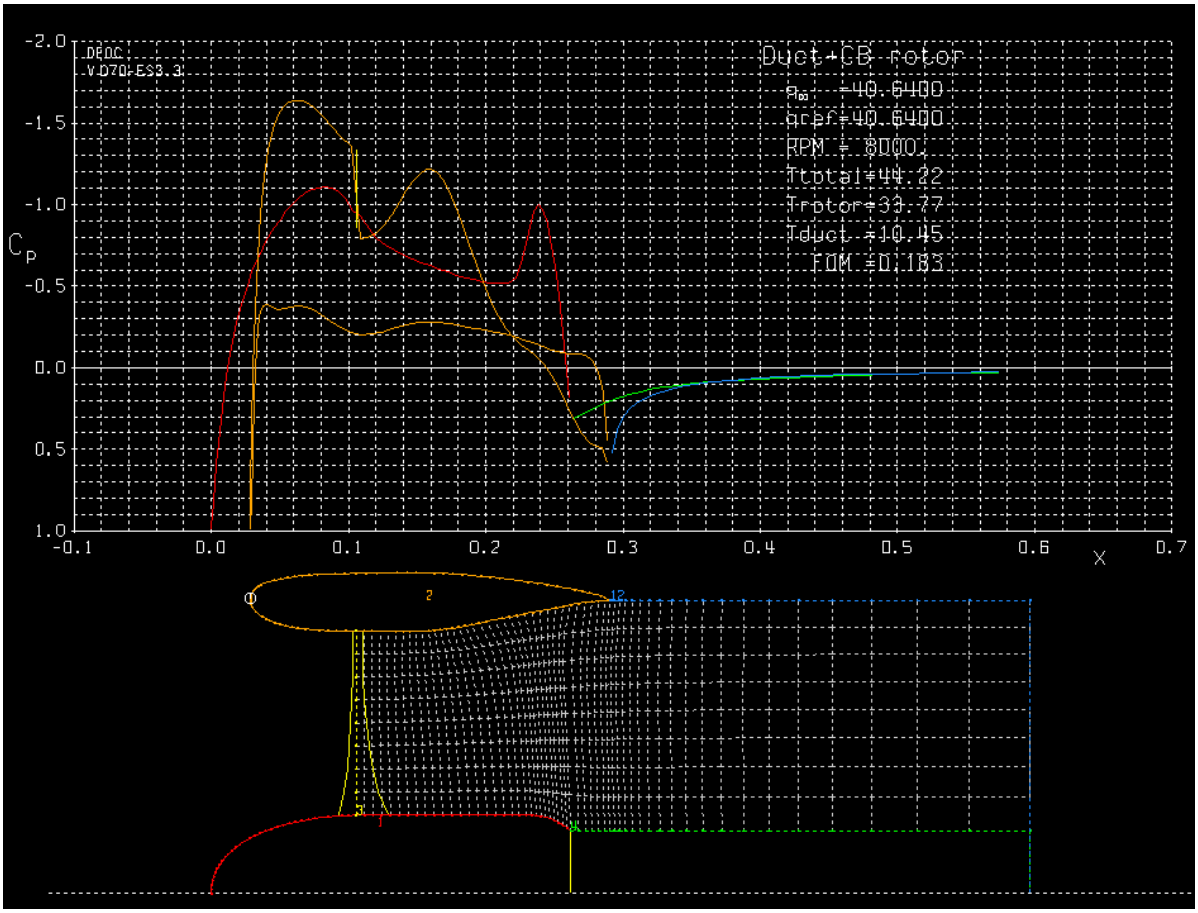

Figure 3.1: Example of DFDC analysis. The top plot shows the pressure distribution on the duct profile (indicated in orange), and centerbody profile (indicated in red). The example model is based on the DFS of Grunwald & Goodson. [9]

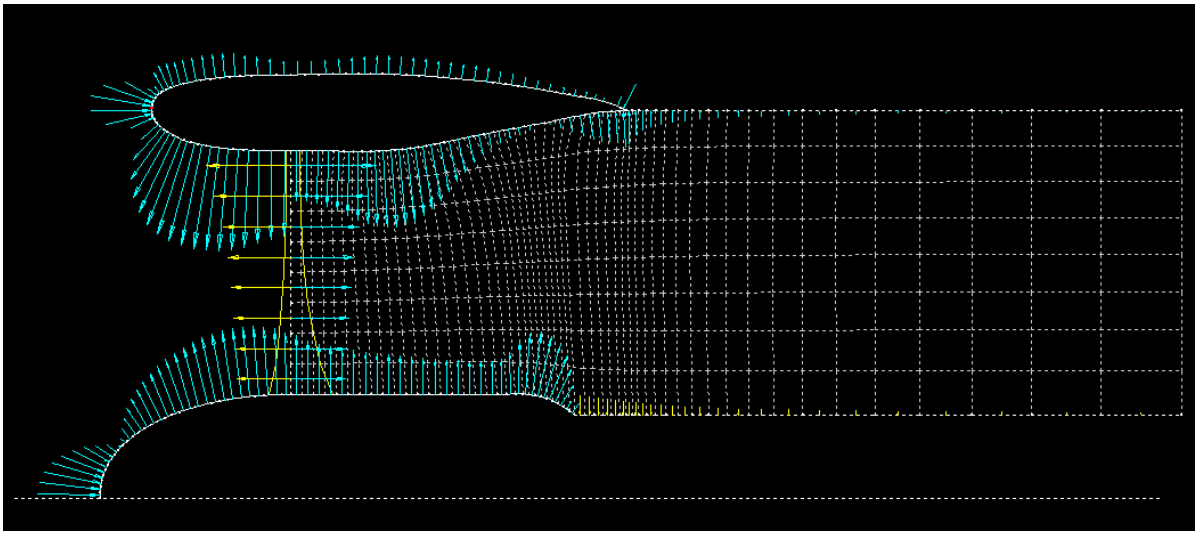

Figure 3.2: Example of DFDC pressure vector distribution, which corresponds to the analysis done in Figure 3.1. At the leading edges, pressure vectors are pointing into the forward direction, hence this indicates the duct thrust. Example model is based on the DFS of Grunwald & Goodson [9]

This section explains how these procedures are executed. To visualize the structure of how PAP works, a flow diagram is presented in Figure 3.3(a). Each propeller system consists of a propeller and centerbody, which are defined by settings files. Additionally, a duct airfoil is given for the ducted fans. An example of the ducted fan geometry is given in Figure 3.3(b). In Appendix D more elaborated flow diagrams are presented on the PAP structure.

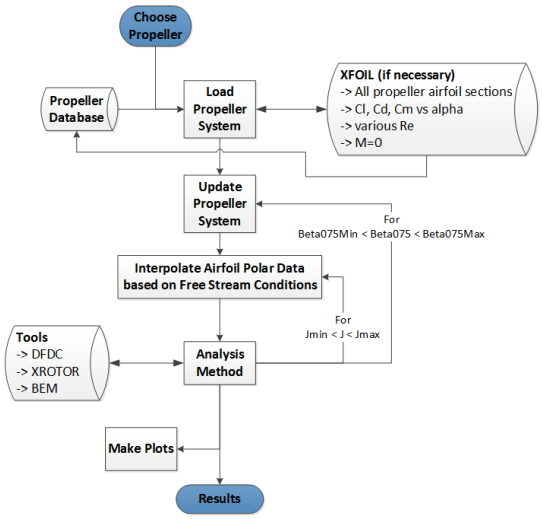

(a) Work flow diagram

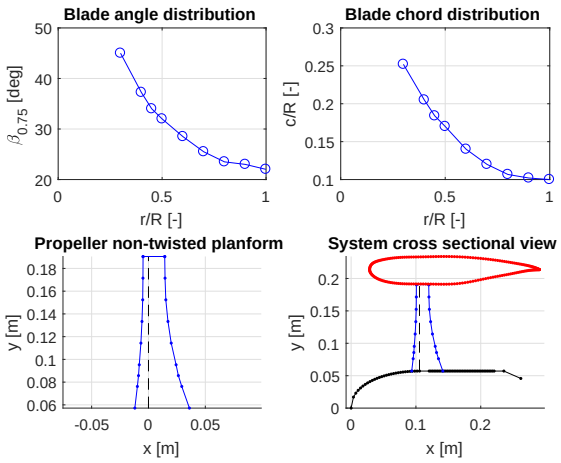

(b) Propeller system definition. Example model is based on Grunwald's DFS [9]

Figure 3.3: Propeller Analysis Program overview

The user starts with choosing a propeller from the database, which includes all geometrical and aerodynamic properties of the propeller and its blade element sections. If the aerodynamic properties in terms of lift, drag, moment versus angle of attack of all blade sections are not known, XFOIL is used to make the data for a range of Reynolds numbers. This data is then saved into the propeller database, such that the user can use it for a next time. Once the propeller properties are loaded, the blade pitch angles are updated based on the selected $\beta_{0.75}$ setting. Secondly, based on the free-stream conditions i.e. the advance ratio J, the airfoil polars of all blade blade sections are interpolated. After the airfoil interpolation, the correct propeller analysis tool is chosen. For ducted fans this automatically is DFDC, for unducted propellers the user can choose between XROTOR including its various solvers and BEM. Once the inputs and the preferred analysis tool are chosen, a single point analysis is computed. This procedure is repeated for various advance ratios and blade pitch settings to acquire propeller performance maps. After the analysis, all output is stored in one data package and various propeller performance plots are generated.

3.2.1. AIRFOIL POLAR INTERPOLATION

Both XROTOR and DFDC require airfoil lift polar characteristics as input, instead of the lift/drag polars which follow from XFOIL. The BEM code however uses the airfoil polars directly. The following parameters need to be know per blade element section:

- Maximum lift coefficient $C_{l_{\max}}$
- Minimum lift coefficient $C_{l_{\min}}$
- Zero-lift angle of attack α_0
- Lift gradient of the linear part of the lift curve C_{l_α}
- Lift gradient after stall $C_{l_{\alpha_{\text{stall}}}}$
- Lift increment to stall $\Delta C_{l_{\text{stall}}}$
- Minimum drag coefficient C_{d_0}
- Lift coefficient at minimum drag coefficient $C_l^{C_d=C_{d_0}}$
- Gradient of drag coefficient with respect to lift coefficient squared $\delta C_d / \delta C_l^2$
- Critical Mach number M_{crit}

To convert the airfoil polars which follow from XFOIL into the parameters listed above, an airfoil interpolation protocol developed by T. Sinnige is used, see Figure 3.4. This protocol also includes a correction to the lift coefficient, which includes the rotational effects. The resulting parameters can be directly used for XROTOR and DFDC.

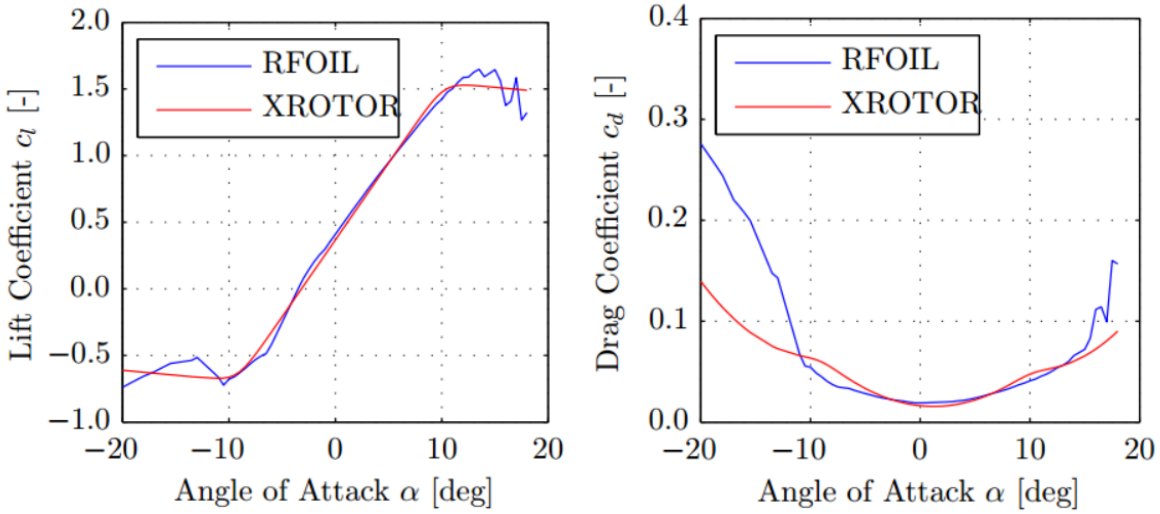

(a) Example interpolated $C_l - \alpha$ curve

(b) Example of interpolated $C_d - \alpha$ curve

Figure 3.4: Example of airfoil interpolation protocol by Sinnige [60]. The raw data (RFOIL) is compared with the fitted data (XROTOR)

3.2.2. MULTI ANALYSIS

In multi analysis, the user is allowed to vary one of the design parameters of the propeller system, and then plot the propeller performance in terms of thrust, torque, and efficiency for various advance ratios. The benefit of this analysis, is that the user can use this to investigate the influence of a certain design parameter on the propeller performances.

For example, to study what the effect is of modifying the aspect ratio of a ducted fan, this protocol can be used to determine whether a larger aspect ratio is more beneficial for the propulsive efficiency or not. Because the duct aspect ratio has a large influence on the aerodynamic efficiency of the DFPE which affects the stability related performance, see Section 2.3, it should also be determined how it influences the thrust related performance. An example of a multi analysis with a varying aspect ratio is presented in Section 3.3.3.

3.2.3. PROPELLER MAP ANALYSIS

The propeller map analysis is similar to the multi analysis, however for this particular analysis variable parameter is the propeller blade pitch $\beta_{0.75}$. By doing so, the user can generate a propeller map for a given range of advance ratios and blade pitches.

The output of the propeller map analysis is structured in such a manner, that the Initiator can easily be used for the mission analysis simulation. During this simulation for turboprop aircraft it is required to evaluate the propulsive efficiency at each time step. Currently a fixed value for η_{prop} is used for the take-off, climb, and cruise phases individually. With the methods implemented in PAP, the `MapAnalysis` results a database which contains the maximum efficiency versus advance ratio. For a fixed RPM, which is often seen at variable blade pitch propellers, the advances ratio scales with airspeed. And so the output of PAP can be used to have a more realistic propeller performance analysis in the Initiator.

3.3. RESULTS

This section shows a set of PAP results to demonstrate its capabilities. Section 3.3.1 shows an example of a comparison between the various unducted fan tools. Because the focus of this thesis research lies on the performance study to ducted fans, it is decided to put the emphasis of the PAP validation on DFDC, see Section 3.3.2. An example of a parametric study to the duct aspect ratio is given in Section 3.3.3.

3.3.1. BEM VS XROTOR

Since PAP has various tools available to determine the performance of an unducted propeller, such as BEM and the multiple XROTOR solvers, the results of these methods are compared. A propeller map analysis is done with a default propeller of PAP. The exact same analysis is done for all unducted propeller solvers. The propeller map results are shown in Figure 3.5.

The results in the figure show that for this default propeller, the various methods show similar results. However, it can be seen clearly that the BEM results are slightly overestimated compared to the XROTOR results. Especially in the propeller power, see Figure 3.5(c), the BEM code underestimates the power coefficient for the lower advance ratios. The significance of this effect decreases with advance ratio.

Furthermore, when having a closer look at the XROTOR results, the values of the potential (`POT`) and vortex (`VRTX`) methods are almost the same, while the values determined with the gradient (`GRAD`) method are less within range. Because the potential method gives almost the same accuracy as the vortex method for this propeller, and since the potential method is faster than the vortex method, it is beneficial to have the potential method as the default XROTOR solver.

3.3.2. DFDC VALIDATION

Because DFDC is a new tool within the Initiator research group, a validation is required to determine how accurate it is to model the performances of ducted fans. The validation of DFDC is mainly done by the thesis of Harinarain [43], so therefore the conclusion of his research is presented in this section.

A validation study is done to the windtunnel experiments with DFS researched by Grunwald & Goodson [9], see the model in Figures 3.1, 3.2, and 3.3(b). Harinarain concluded that compared to the experimental research the total thrust acquired with DFDC, show a maximum deviation of 10% [43]: "It can therefore be concluded that DFDC is able to predict variations in thrust accurately for a given thrust input at operating conditions. This means that DFDC is a well suitable tool for analyzing design trends".

3.3.3. MULTIANALYSIS FOR DUCTED FANS

As an example, a multi analysis is done with the ducted fan described by Grunwald and Goodson [9]. The default geometry of the DFS by Grunwald and Goodson is depicted in Figure 3.3(b). The fan ($D_{\text{fan}} = 0.38$m) operated at a constant 8000RPM, and so the advance ratio increased with airspeed. This section shows the results of a `MultiAnalysis` done with the duct aspect ratio varying from 1 to 2 in steps of 0.5. The default aspect ratio of the reference DFS is $AR = 1.8$.

The results of the analysis are shown in Figure 3.6. In general sense it is concluded that a higher duct aspect ratio is more beneficial for the maximum efficiency. Furthermore, it is possible to achieve the maximum efficiency at higher advance ratios with increasing AR_{duct}.

When looking at Figure 3.6(b), it is concluded that the total thrust increases with the aspect ratio. The increase in propeller thrust is rather constant, while the duct thrust shows a non-linear behavior. This indicates that increasing the aspect ratio is mainly favorable for the propeller thrust generation. At lower aspect ratios, having a lower AR_{duct} is more beneficial, and for the higher aspect ratios a higher AR_{duct} is more beneficial for higher thrust.

Figure 3.6(b) shows that the propeller thrust is higher than the duct thrust, and that both are decreasing with increasing advance ratio. Around $J = 1$, it is seen that the thrust becomes negative. This indicates that the DFS is generating mostly drag at this high velocity. Because this causes singularities in the results, because the efficiencies vary between $\pm\infty$, it is concluded that these results are not reliable anymore once the thrust becomes negative.

Figure 3.6(b) shows that DFS with a higher AR_{duct} also require more power. However, since the increase in thrust is more than the increase in power with increasing aspect ratio, the propulsive efficiency increases with AR_{duct}.

This example shows how the `MultiAnalysis` protocol can be used to choose ideal values for DFS design parameters.

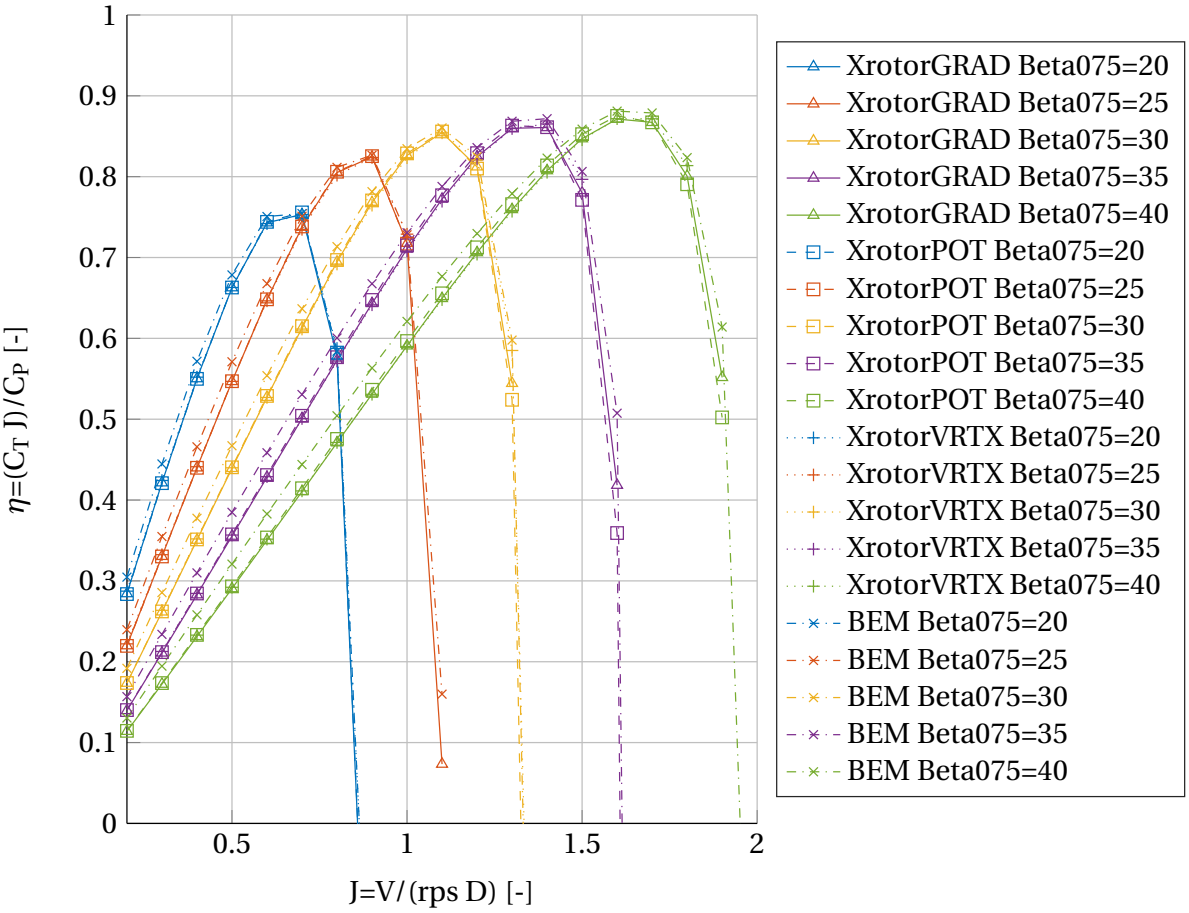

(a) Propulsive efficiency

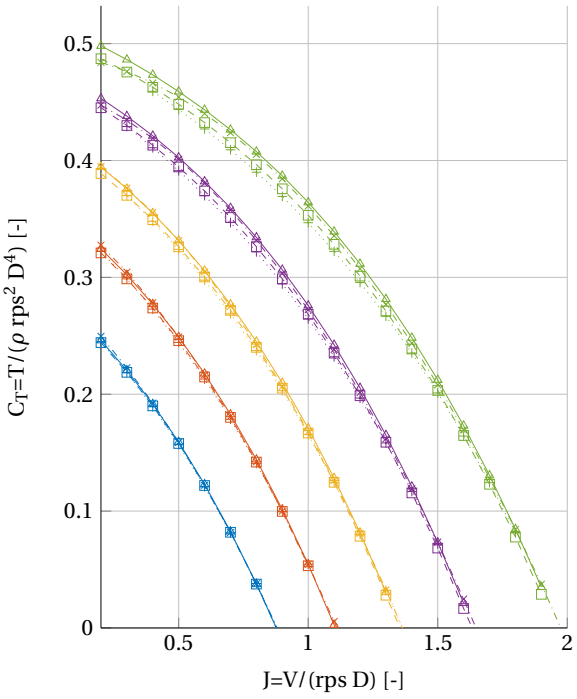

(b) Thrust coefficient

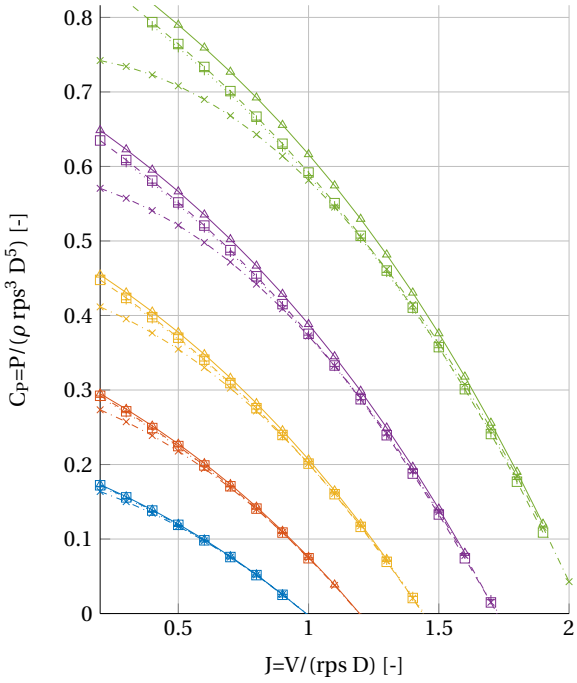

(c) Power coefficient

Figure 3.5: Comparison of BEM vs XROTOR with PAP for a default propeller geometry

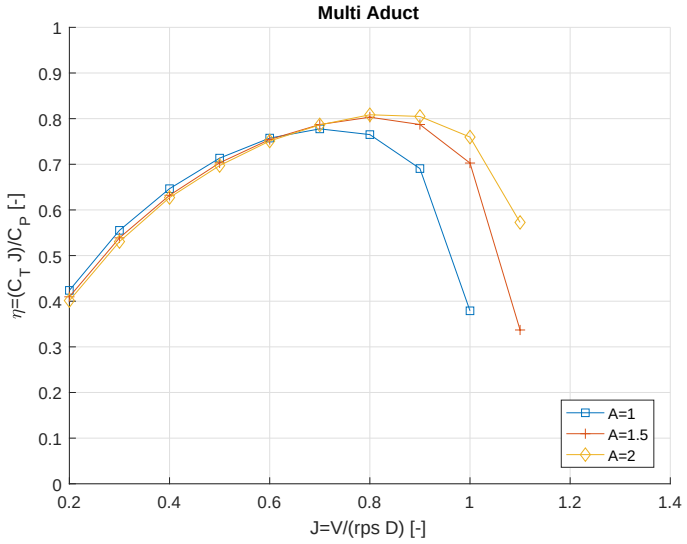

(a) Propulsive efficiency

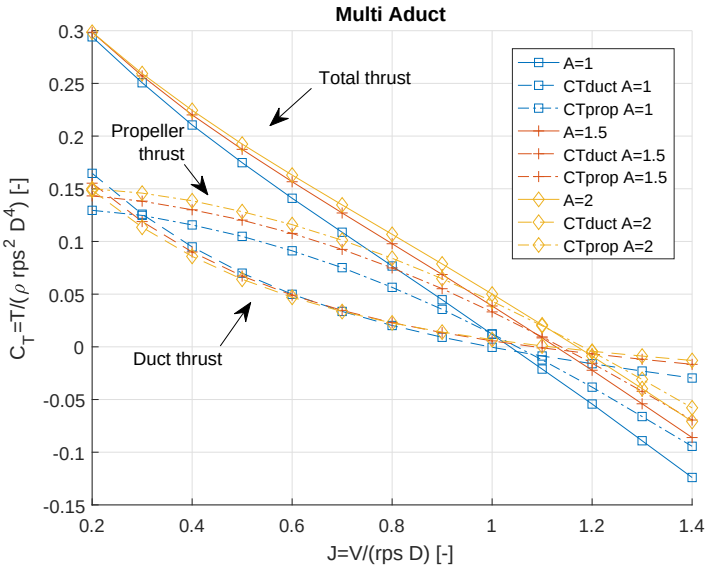

(b) Thrust coefficient

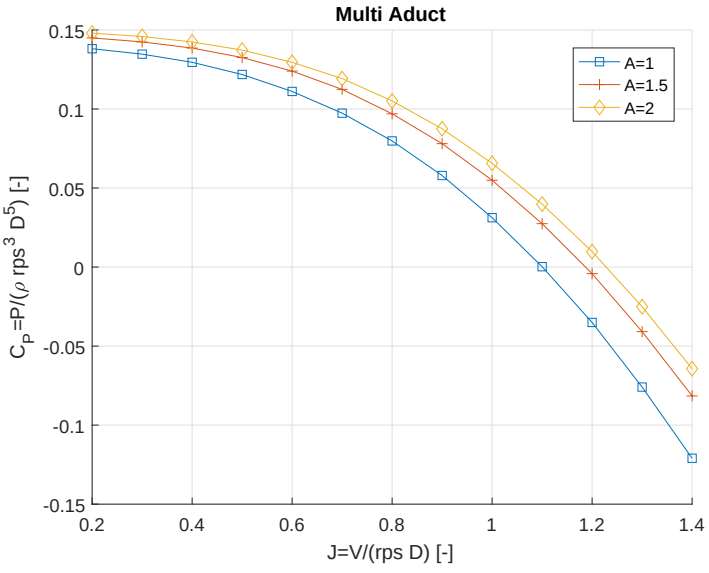

(c) Power coefficient

Figure 3.6: Results of PAP multi analysis with DFS model based on Grunwald Goodson [9], with variable duct aspect ratio. Negative thrust indicates that the system operates beyond its design speed, and only produces drag. RPM = 8000, $D_{fan} = 0.38m$

4

PROPULSION WEIGHT ESTIMATION

Aircraft design handbooks provide methods to determine the masses of conventional propulsion systems such as turbofans and turboprops. The DFS is however a mix between both engine types, and therefore it is intricate to determine which conventional methods can be applied. Furthermore, most empirical weight estimation methods rely on statistical data, and therefore they are often limited to a handful of geometric parameters. Therefore it is decided to update the propulsion weight estimation in the Initiator, based on the component masses of the propulsion system, such as gasturbine, fan, centerbody, duct, and pylon.

This chapter focuses solely on the component mass estimations of the propulsion system. The other aircraft systems are calculated with Torenbeek's Class 2 Mass Estimation method, see Appendix F. Some systems, such as the wing and fuselage masses are calculated with physics-based Class 2.5 Weight Estimation methods. These results overwrite the Class 2 Weight Estimation Results, see the Initiator flow diagram in Figure 1.6.

4.1. TURBOPROP

The turboprop engine or gasturbine, is the part of the propulsion system which converts air plus fuel into work, i.e. shaft power. The mass of the turboprop engine can either be acquired directly from the engine manufacturer, or via empirical relations. This section shows a trade-off between various turboprop mass estimation methods.

4.1.1. RAYMER

Originally, the Initiator used the weight estimation methods as imposed by Raymer [30]:

$$W_{\text{eng}} = 1.67(P_{\text{TO}})^{0.803} \tag{4.1a}$$

$$L_{\text{eng}} = 4.14(P_{\text{TO}})^{0.373} \tag{4.1b}$$

$$D_{\text{eng}} = 9.48(P_{\text{TO}})^{0.120} \tag{4.1c}$$

With the engine weight (W_{eng}, [lb]), take-off break horse power (P_{TO}, [hp]), engine length L_{eng} [in], and engine diameter (D_{eng}, [in]). The computed W_{eng} of Equation (4.1a) is the *uninstalled* engine weight, also known as the engine dry weight.

The benefit of this method is that it quickly determines the mass and dimensions of the engine, for a required engine power. Once the power loading of the aircraft gets updated throughout the design process, the engine size scales accordingly.

4.1.2. ROSKAM

In Roskam's[42] aircraft design volumes, multiple weight estimation methods are presented (Volume 5), such as Cessna, USAF, Torenbeek, and GD. However, for commercial transport aircraft all methods highly advise to use actual engine manufacturers data, and so they do not present empirical relations for this type of aircraft. Additionally, Roskam provides a linear log-log approximation to predict the dry weight of a turboprop based on data of a set of reference engines, see Figure 4.1.

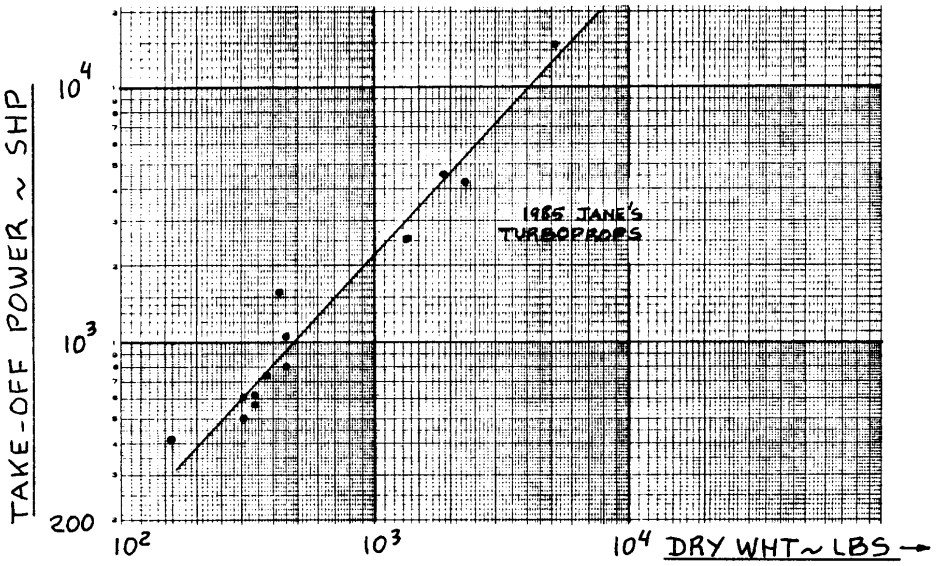

Figure 4.1: Turboprops: take-off shaft horse power and dry weight trends [42]

Roskam does not provide the approximated relation which is shown in the figure, so therefore the following relation is derived from Figure 4.1:

$$W_{\text{eng}} = 500\left(\frac{P_{\text{TO}}}{10^3}\right)^{\frac{\log(4000/500)}{\log(10^4/10^3)}} \tag{4.2}$$

With the engine weight (W_{eng}, [lb]), take-off break horse power (P_{TO}, [hp]). The approximation is acquired by using a linear log-log relation, with the following two data points derived from the figure; [500lb, 10^3hp] and [4000lb, 10^4hp].

4.1.3. TURBOPROP WEIGHT ESTIMATION TRADE-OFF

It is investigated how Raymer's and Roskam's methods compare to existing engine designs. A statistical analysis of 16 often used turboprops is done, see Appendix E, and the results are presented in Figure 4.2. [1]

Figure 4.2 shows that Roskam's method results in more accurate approximation than Raymer's method, for the reference engines listed in Appendix E. Figure 4.2 clearly shows that Roskam's method approximates the uninstalled engine mass more accurately than Raymer's method. Interesting enough both methods determine the mass purely based on the power requirement. The difference might be caused by the fact that Raymer's design studies often refer to military applications of turboprop aircraft, while Roskam's method are more applied to the civil aviation. Because the design philosophies for these two categories of aircraft is different (high performance and maneuverability versus fuel efficiency), it is likely that this possibly results in a different engine mass estimation method.

Because Roskam's method proved to be more accurate for frequently used turboprops in civil aviation based on the results in Figure 4.2, it is decided to replace Raymer's mass estimation method with the one provided by Roskam.

Since the gasturbine is installed in a centerbody, the mass of the centerbody should also be taken into account. Raymer adds 30% of the turboprop mass, to arrive at the *installed* engine mass [30]. For the implementation of the centerbody in the Initiator, it is assumed that its mass corresponds to Raymer's 30% for to the installed engine weight:

$$W_{\text{cb}} = 0.30 W_{\text{eng}} \tag{4.3}$$

[1] All results from Raymer and Roskam which are determined with the equations presented in this section are converted to SI units, and then shown in the figure.

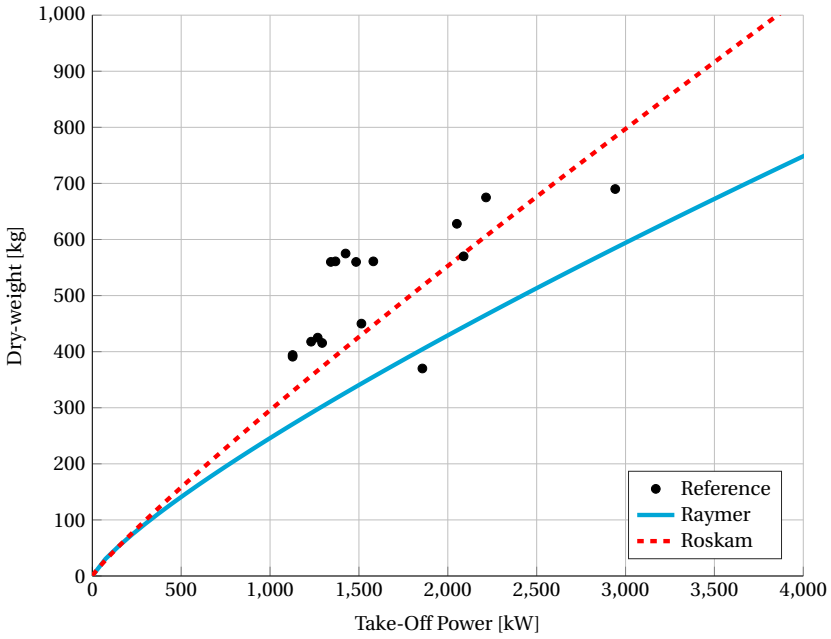

Figure 4.2: Turboprop weight estimation

4.2. PROPELLER

Although the mass of the propeller is rather small compared to the total propulsion mass (±8%) [40], it is still relevant to have an accurate mass prediction of this system. This section shows the various propeller mass estimation which have been implemented in the Initiator.

4.2.1. TORENBEEK

Torenbeek's method can be used to determine the weight of a propeller [40]:

$$W_{\text{prop}} = 0.108(N_{\text{prop}})^{0.218}\left[D_{\text{prop}}(P_{\text{TO}})(N_{\text{bl}})^{0.5}\right]^{0.782} \tag{4.4}$$

The propeller weight (W_{prop}) is given in [lbs], the engine take-off power (P_{TO}) in [hp], and propeller diameter (D_{prop}) in [ft]. This method is mainly intended for metallic propellers.

4.2.2. HAMILTON STANDARD - NASA

Hamilton Standard has developed in collaboration with NASA a generalized propeller weight estimation method:

$$W_{\text{prop}} = K_{\text{W}}\left[\left(\frac{D_{\text{prop}}}{10}\right)^2\left(\frac{N_{\text{bl}}}{4}\right)^{0.7}\left(\frac{AF}{100}\right)^{0.75}\left(\frac{(RPM)(D_{\text{prop}})}{20000}\right)^{0.5}\left(\frac{P_{\text{TO}}}{10D_{\text{prop}}^2}\right)^{0.12}(M_{\text{des}}+1.0)^{0.5}\right] + C_{\text{W}} \tag{4.5}$$

With number of blades (N_{bl}), propeller diameter (D, [ft]), activity factor (AF), shaft power (P_{TO}, [hp]), design Mach number (M_{des}), and counterweight (C_{W}, [lb]). The counterweight C_{W} for fiberglass-bladed, constant-speed, full feathered propellers can be computed with Equation (4.6), with scaling factor $K_{\text{W}} = 210$ [61].

$$C_{\text{W}} = 2.5\left[\left(\frac{P_{\text{TO}}}{RPM}\right)\left(\frac{M_{\text{des}}}{D_{\text{prop}}}\right)(AF)(N_{\text{bl}})\right] \tag{4.6}$$

4.2.3. PROPELLER WEIGHT ESTIMATION TRADE-OFF

A comparison of both methods with statistical data of reference propellers from the HS-NASA research [61] is presented in Table 4.1. It is clearly seen that the accuracy of the HS-NASA method lies within ±10%, whereas Torenbeek's method significantly underestimates the propeller masses.

Mainly because the HS-NASA method is able to include the propeller geometry aspects by means of the activity factor *AF*, it is decided that this method is preferred over Torenbeek's propeller mass estimation method. For further reference to the propeller or fan weight, W_{fan} is used.

Table 4.1: Comparison of propeller mass estimation methods, based on reference data from an advanced general aviation propeller study [61], see Appendix E.

		HS-NASA		***Torenbeek***	
Propeller	**Mass**	**Mass**	**Diff**	**Mass**	**Diff**
	[kg]	[kg]	[%]	[kg]	[%]
23LF-321	67.6	73.8	+9.3	47.9	-29.1
23LF-329	68.9	73.6	+6.8	64.3	-6.8
23LF-333	65.3	69.4	+6.3	61.3	-6.2
33LF-307	54.4	50.3	-7.5	42.7	-21.6
33LF-327	54.4	55.7	+2.3	46.2	-15.2
1500 HP	161.0	160.6	-0.3	128.6	-20.2
1500 HP	140.2	140.2	0.0	128.6	-9.3
DHC-7	171.0	164.7	-3.7	118.7	-30.6
DHC-7	145.1	145.1	0.0	118.1	-18.6

4.3. DUCT

Besides the turboprop/gasturbine, the nacelle/duct is one of the most heavy components of DUUC's propulsion system due to its large size. Because the dimensions of the DFS can vary significantly throughout the design process, it is essential to have a weight estimation method available which is sensitive to these changes.

During the thesis research it is found the standard mass estimation methods for determining the nacelle mass are insufficient, or invalid for the DUUC. The pitfall of most standard methods, is that they are not sensitive for geometry changes of the engine. The second pitfall of the standard nacelle group mass estimation methods, is that they are based on a statistical analysis of turbofan nacelles. Because the architecture of these types of engines is different compared to the turboprop engine, it is determined that these methods are not valid to determine the mass of a ring wing.

To conclude, there existed a need for a physics-based mass estimation method of the DUUC's ducts. This section elaborates on the various existing nacelle mass estimation methods of the Initiator, and furthermore a new mass estimation method specific for the DUUC's ducts.

4.3.1. RAYMER

Originally, the Initiator used Raymer's method to determine the mass of the nacelle group (W_{ng}, [lb]) [30]:

$$W_{\text{ng}} = 0.672 K_{\text{ng}} N_{\text{Lt}}^{0.10} N_{\text{w}}^{0.294} N_{\text{z}}^{0.119} W_{\text{ec}}^{0.611} N_{\text{en}}^{0.984} S_{\text{n}}^{0.224} \tag{4.7}$$

The equation shows that it is sensitive to geometrical properties, such as the nacelle length (N_{LT}, [ft]) and wetted area (S_{n}, [ft^2]). The pitfall of this equation however is that it is based on a set of old turbofan engines, which are not directly applicable to simple ducted propellers.

4.3.2. TORENBEEK

Torenbeek provides two equations for the nacelle group mass estimation:

$$W_{\text{ng}} = 0.055 T_{\text{TO}} \tag{4.8a}$$

$$W_{\text{ng}} = 0.065 T_{\text{TO}} \tag{4.8b}$$

Both equations state that the nacelle weight (W_{ng}, [lb]) is solely depending on the take-off thrust (T_{TO}, [lb]). Equation (4.8a) is valid for pod mounted turbojet or turbofan engines, and equation (4.8b) is valid for high bypass turbofans with short fan duct. The resulting value also includes the pylon weight and extended nacelle structure for a thrust reverser installation. In the absence of thrust reversing, a reduction of 10% may be assumed [40]. Because Torenbeek's method is not depended on the engine geometry, this method is found unsuitable for the DUUC.

4.3.3. CRANFIELD UNIVERSITY SEMI-EMPIRICAL METHOD

The University of Cranfield published various research papers in the fields of turbofan mass estimation methods, which showed to be more accurate then the existing empirical methods [62–64]. The main benefit of the Cranfield methods is that they implement a more refined turbofan geometry, compared to the empirical ones:

$$W_{ng} = k\pi \left(2 l_{ca} D_{ca} + l_{bo} D_{af} + 2 l_{af} D_{af}\right) \tag{4.9}$$

Equation (4.9) derived by Jackson [62] is based on the turbofan geometry, as sketched in Figure 4.3. Furthermore, W_{ng} in [kg], $k\pi = 24.88$ kg/m^2.

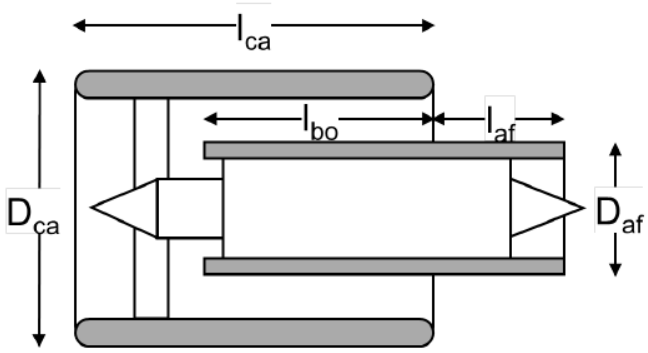

Figure 4.3: Nacelle dimensions for the Cranfield Turbofan Mass Estimation, by Jackson [62]

The Cranfield method includes detailed information about the duct and centerbody geometries, which is excellent for the mass estimation of the DUUC. The disadvantage of this method however, is that it uses an empirical correction factor of $k\pi = 24.88$ kg/m^2. This factor is based on a single turbofan engine, the Rolls Royce T892M [62–64]. Therefore this method is valid for engines in the same class as the reference engine, but it should not be used to determine the structural mass of a ring-wing.

4.3.4. CRANFIELD UNIVERSITY COMPONENT-BASED METHOD

Research by Lolis [63] done at the Cranfield University goes one step further, into the detailed mass estimation method of all turbofan components. This research therefore calculates the individual masses of all compressor stages, combustion chamber, turbine stages, fan, duct, nacelle, etc. From this method, the duct mass estimation is extracted to be used for the DFS. This method is based on an internal pressure vessel theory, with additional reinforcements for blade-containment. Lolis' duct weight estimation states that the fan should be sized for two main criteria: skin thickness to withstand a certain internal pressure, and secondly the thickness of a blade-containing layer in case of a blade release. The summation of those two components yield the total clean duct mass.

DUCT SHELL SKIN THICKNESS

The airfoil plate thickness, also known as duct shell skin thickness ($t_{\text{duct}_{\text{press}}}$, [m]) is computed via the pressure vessel theory, which includes the total air pressure (P_{tot}, [Pa]), duct outer diameter (D_o, [m]), and maximum allowed yield stress (σ_y, [Pa]) [63, 65]:

$$t_{\text{duct}_{\text{press}}} = \frac{P_{\text{tot}} D_o}{2\sigma_y} \tag{4.10}$$

The total air pressure is calculated based on the static atmospheric pressure (P_{stat}) and the dynamic pressure on the inside of the duct (P_{dyn}). The pressure distribution on the inner side of the duct is acquired via DFDC, with the method as described in Chapter 3. The duct will generate a large under-pressure distribution on the lower side of the airfoil during the take-off, see Figure 3.2. Since the thrust is the largest during take-off, this is flight phase is identified as the critical condition for the duct sizing. Because the duct will be sized for an under-pressure, the maximum stress in Equation (4.11) is based on the compressive yield strength. The difference between the tensile and compressive strengths of Al7075T6 is negligible, as indicated in Table 4.2, so this does not result in significant calculation errors based on the yield strength assumption stated here.

BLADE CONTAINMENT LAYER SKIN THICKNESS

Next to that, the thickness of the blade containment material (t_{con}), e.g. Kevlar sheets, is computed with [63]:

$$t_{\text{duct}_{\text{con}}} = \frac{0.4 E_{\text{kin,bl}} E}{\sigma_y^2 h_{\text{bl}} c_{\text{bl}}} \tag{4.11}$$

With minimum wall thickness (t_{con}, [m]), blade kinetic energy ($E_{\text{kin,bl}}$, [J]), material Young's Modulus of elasticity ([E]), material maximum yield stress (σ_y, [Pa]), blade height (h_{bl}, [m]) and blade chord (c_{bl}, [m]). The blade kinetic energy is derived from the general form of kinetic energy, which is based on a systems mass (m, [kg]), and velocity (V, [m/s]) [66]:

$$E_{\text{kin}} = \frac{1}{2} m V^2 \tag{4.12}$$

The mass of a single fan blade is calculated with the methods described in Section 4.2. The velocity of the blade is calculated with $V = \omega \overline{R}$, which is based on the angular velocity (ω, [rad/s]) and centroid fan radius ($\overline{R}$, [m]). Because fans have a specific chord distribution, see the example in Figure 3.3(b), $\overline{R}$ should be used to calculate the kinetic energy of the blades. The fan centroid normalized with the fan radius is calculated based on the weighted average of the radial chord distribution:

$$\left(\frac{\overline{r}}{R}\right) = \frac{\sum \left(\frac{r}{R}\right)_i \left(\frac{c}{R}\right)_i}{\sum \frac{c}{R}_i} \tag{4.13}$$

The centroid of the fan is then calculated with $\overline{R} = \left(\frac{\overline{r}}{R}\right) R_{\text{fan}}$. The blade chord ($c_{\text{bl}}$) given in Equation (4.11) is calculated on based on the interpolation of the chord distribution and the fan centroid.

Finally, the following equation is derived to determine the kinetic energy of a single fan blade release:

$$E_{\text{kin,bl}} = \frac{1}{2} \left(\frac{W_{\text{fan}}}{N_{\text{bl}}}\right) \left(\omega \left(\frac{\overline{r}}{R}\right) R_{\text{fan}}\right)^2 \tag{4.14}$$

TOTAL MASS ESTIMATION

The volume of the duct shell is calculated by multiplying the duct airfoil arc length L_{arc}, with the circumference of the inner duct radius (D_{i}) taken at the longitudinal location of the fan, and the skin thickness:

$$V_{\text{duct}_{\text{pres}}} = \pi \left(D_{\text{i}}\right) \left(L_{\text{arc}}\right) \left(t_{\text{duct}_{\text{pres}}}\right) \tag{4.15}$$

The airfoil length is calculated by summing up the distances between two airfoil coordinates (x, y), done for all n coordinates:

$$L_{\text{arc}} = \sum_{i=1}^{n-1} \sqrt{\left(x_{i+1} - x_i\right)^2 + \left(y_{i+1} - y_i\right)^2} \tag{4.16}$$

The volume of the blade containment layer is simply calculated by taking the circumference of the inner duct radius, at the location of the fan ($D_{\text{duct,in}}$), multiplied with the layer width:

$$V_{\text{duct}_{\text{con}}} = \pi \left(D_{\text{i}}\right) \left(c_{\text{bl}_{\text{max}}}\right) \left(t_{\text{duct}_{\text{con}}}\right) \tag{4.17}$$

The width of the blade containment layer should be at least as wide as the maximum chord of the fan blade. Additionally, a correction factor to add 20% more width is assumed for the layer width calculation ($k_{\text{c}} = 1.2$):

$$c_{\text{bl}_{\text{max}}} = k_{\text{c}} R_{\text{fan}} \left(\frac{c}{R}\right)_{\text{max}} \tag{4.18}$$

Combined with the densities of both materials, the total duct mass is computed. In the current design the duct airfoil is made of the alloy aluminium 7075-T6, and the blade-containing ring is made of Kevlar with 49 yarns, see Table 4.2 for the duct material properties. Both of these materials are often found in aircraft structures, so therefore it is convenient to implement them in the DFS [67–69]. To account for the producibility of the shell and the blade containment liner, it is assumed that the minimum thickness should be 1.5mm. Furthermore, to include the masses for the jet vanes, and duct structural reinforcements, a correction factor of $k_{\text{duct}} = 1.5$ is assumed:

$$W_{\text{duct}} = k_{\text{duct}} \left(V_{\text{duct}_{\text{press}}} \rho_{\text{Al}} + V_{\text{duct}_{\text{con}}} \rho_{\text{Kev}}\right) \tag{4.19}$$

Table 4.2: Material properties for the duct. [67, 68]

Properties	Symbol	Unit	Al7075T6	Kevlar49
Density	ρ	kg/m^3	2800	1440
Young's E-modulus	E	GPa	72.5	112.4
Tensile strength	σ_y	MPa	503	3600
Compressive strength	σ_y	MPa	505	n.a.

4.4. PYLON

The last propulsion mass estimation which needs to be done is for the pylon. Because the pylon is designed to carry the masses of the engine components which are installed at the tip of the pylon, i.e. gasturbine, centerbody, fan, and duct, it is obvious that the pylon structural mass scales with the masses of the other propulsion components. Based on basic structural analysis, if the pylon tip mass increases the pylon needs to be more rigid to deal with the structural loads, which will increase its own mass [70].

It would be possible to make a simplified wing-box model, which uses the pylon tip mass and maximum thrust force to calculate the required wingbox thicknesses. The disadvantage of this method, is that the calculated thicknesses will only be designed for static loads. Any dynamic loads such as aeroelasticity cannot be easily done without further extensive calculations [20, 70].

To have a proper structural analysis of the pylon, it is essential to determine the critical load cases under which the DFPE needs to operate. An initial estimate for the maximum load case would be based on the take-off rotation, due to the maximum engine thrust, and rotational acceleration on the DFPE. However, another possible critical load case could be the steepest turn, where the aircraft experiences a high g-force [45]. A third option would be to size the DFPE based on a hard-landing [70]. In short, there are various critical load cases to be considered, if it is decided to use a physics-based method to calculate the pylon mass. Unfortunately given the time and scope of this thesis research, such an analysis is out of the question.

To simplify the pylon mass estimation, it is assumed that the pylon mass equals 30% of its tip mass:

$$W_{\text{pylon}} = 0.30\left(W_{\text{eng}} + W_{\text{cb}} + W_{\text{fan}} + W_{\text{duct}}\right) \tag{4.20}$$

This pylon mass estimation indirectly contains the effect of a variable duct geometry on the structural rigidity of the pylon. For instance, if the duct diameter increases, the pylon needs to become longer to guarantee a certain fixed clearance between the duct and the fuselage. With an increasing duct diameter, the calculations in Section 4.3 result a higher W_{duct}. Because W_{duct} is implemented in the pylon mass calculation, the pylon gets heavier if its span width increases. Secondly, if a larger engine is required, it will increase in length based on Equation (4.1b). Because of this, the centerbody length increases to ensure that the engine fits inside the centerbody, and therefore the pylon chord length can increase also. Because the centerbody mass scales with engine mass with Equation (4.3), and both W_{eng} and W_{cb} are included in the pylon mass estimation, the pylon mass scales with increasing propulsion component geometries.

Because it is uncertain how accurate the stated pylon mass assumption is, a sensitivity analysis in Section 6.3 is done to the propulsion mass weight factor. If the total mass of the DFPE decreases, it will shift the c.g. location more forward. By doing so, the stability and balance analysis of the aircraft changes. Even without performing an extensive detailed structured analysis on the DFPE, by means of a sensitivity analysis it is still possible to study its mass effect on the overall aircraft design.

5

Sizing for Longitudinal Static Stability and Controllability

The backbone for the conceptual DUUC sizing process is based on sizing for longitudinal static stability and controllability, also known as the horizontal stability estimation (HSE) module within the Initiator. For clarification, the term controllability within LSSC refers to trimming during flight to maintain horizontally balanced, as no dynamic flight behavior of the DUUC is analyzed during this thesis. The fact that the DUUC uses an unconventional propulsion system as horizontal stabilizer, which additionally puts a large mass aft of the aircraft and thus shifting the c.g. far aft, makes sizing for LSSC more intricate than for conventional aircraft.

This chapter firstly discusses the lower order tail sizing methods in Sections 5.1 and 5.2. A higher order stability and balance method is Torenbeek's "X-plot" method, which is discussed in Section 5.3. From this method, a set of stability and balance constraints is presented in Section 5.4, which form the baseline for the DUUC wing-positioning method in Section 5.5. The final step is to implement a new DUUC trimming method, which is explained in Section 5.6.

5.1. Tail Volume Coefficient

In conventional aircraft design, a first estimate of the tail size is done with the tail-volume coefficient method [30, 40]:

$$\overline{V}_{\mathrm{H}} = \frac{S_{\mathrm{H}} l_{\mathrm{h}}}{S_{\mathrm{W}} \overline{c}} \tag{5.1}$$

The tail volume coefficient ($\overline{V}_{\mathrm{H}}$) is based on statistical data, to determine the tail-wing area relation ($S_{\mathrm{H}}/S_{\mathrm{W}}$) for a given tail arm normalized with the mean aerodynamic chord ($l_{\mathrm{h}}/\overline{c}$). The mean aerodynamic chord (MAC) is denoted as $\overline{c}$. Once the wing area and longitudinal locations of the wing and tail are fixed in the design process, Equation (5.1) quickly results the required tail area.

This tail volume coefficient however is only valid for planar wing tails, and only for similar sized aircraft, because it is based on the statistical data of $\overline{V}_{\mathrm{H}}$. Furthermore, the calculated tail area with the tail volume coefficient does not explicitly prove that the new design is stable and trimmable.

The combination of these effects make the traditional volume coefficient method not sufficient to be used for the sizing of the DFPE.

5.2. Horizontal Tail Effectiveness

Appending the tail volume coefficient with the aerodynamic efficiency of the horizontal tail planform in terms of its lift-curve slope C_{L_α}, allows to compare the horizontal tail effectivenesses η_{H} of both planar wings and DFPE:

$$\eta_{\mathrm{H_{planar}}} = \left(\frac{S_{\mathrm{H}} l_{\mathrm{h}}}{S_{\mathrm{W}} \bar{c}}\right) C_{L_{\alpha_{\mathrm{planar}}}} \tag{5.2}$$

$$\eta_{\mathrm{H_{DFPE}}} = \left(\frac{S_{\mathrm{H_{proj}}} l_{\mathrm{h}}}{S_{\mathrm{W}} \bar{c}}\right) C_{L_{\alpha_{\mathrm{DFPE}}}} \tag{5.3}$$

The lift gradient of the DFPE $C_{L_{\alpha_{\text{DFPE}}}}$ includes the aerodynamic contributions of all ducts, fan thrust effects, and pylons, as defined by Equations (2.24) and (2.25).

During the design process of the DFPE Equation (5.3) can be used to determine the optimal AR_{duct} which satisfies a given η_{H} requirement. The disadvantage of this approach, is that a good estimate of $\eta_{\text{H}_{\text{DFPE}}}$ is required to guarantee that the resulting AR_{duct} has an acceptable value. Throughout the thesis it is concluded that it is not possible to state that $\eta_{\text{H}_{\text{DFPE}}} = \eta_{\text{H}_{\text{planar}}}$, since this resulted in unrealistically high values of the AR_{duct}. This is mainly caused due to the the fact that the ATR72-600 reference aircraft has a conventional tail with wing mounted engines, and the DUUC has those two systems combined in the DFPE.

Furthermore, modifying the AR_{duct} affects both $S_{\text{H}_{\text{proj}}}$ and $C_{L_{\alpha_{\text{DFPE}}}}$, so this combined effect results in large changes in the absolute value of $\eta_{\text{H}_{\text{DFPE}}}$. Therefore it is decided to keep AR_{duct} fixed per aircraft design convergence of the DUUC in the Initiator.

5.3. X-PLOT METHOD

A higher order method to determine the LSSC of the aircraft is Torenbeek's "X-Plot" method [40], see Figure 5.1. This method consists of two types of plots which are later combined, to determine the required tail to wing area ratio ($S_{\text{H}}/S_{\text{W}}$) and corresponding wing location, which result in a minimum tail area which guarantees a stable and balanced aircraft.

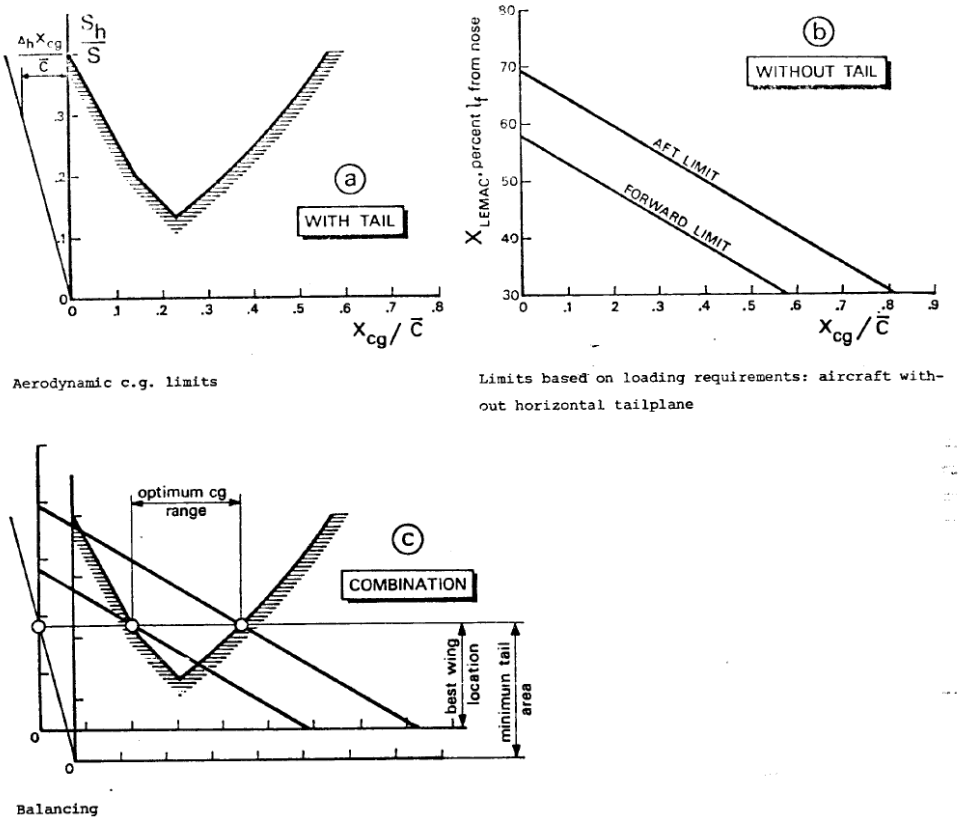

Figure 5.1: Balancing the airplane with the "X-Plot" or "Scissor-Plot" method by Torenbeek [40]

This physics-based method fully relies on moment balances, acquired from the main lift forces of the wing and tail. In other words, the tail is sized such that it can balance the aerodynamic moment of the tailless aircraft around its c.g. The tailless (tail-off) aircraft refers to the wing-fuselage combination [40]. For conventional aircraft this also includes the propulsion group, however for the DUUC it needs to be investigated which propulsion group properties contribute to the tailless aircraft.

The moment balances of the X-plot method determine the stability and trimmability of the aircraft during various critical flight phases, such as longitudinal static stability with and without static margin, trimming up to stall, and tail downforce generation during the take-off rotation. The resulting equations/constraints for longitudinal static stability and controllability are for future reference referred to as the "LSSC-constraints".

Key elements of the original moment balances in the X-plot method, are that the tail to wing area ratio is chosen as a free variable and that all balances are repeated for various wing positions. This procedure first of all results a plot which shows the *required* aircraft c.g. location, which guarantees stable and trimmable aircraft for a given tail to area ratio, see the top left plot in Figure 5.1.

Secondly, because the wing position is also varied in the moment balances, the *actual* aircraft c.g. locations are calculated which result a second plot containing the most forward and aft c.g. locations for the various wing positions, see the top right plot in Figure 5.1.

As a final step, the two plots are combined because they share the same horizontal axis since all c.g. locations refer to the longitudinal aircraft axis, and they are normalized with the leading edge of the MAC (LEMAC). The intersection of the lines results in the minimum tail to wing area ratio including corresponding wing location which satisfies the LSSC-constraints, see the bottom plot in Figure 5.1.

Because simple tail volume methods are not valid for the DUUC, it is decided to use a modified version of Torenbeek's X-plot method to determine DUUC's wing position. In contrary to Torenbeek's original method, the DUUC does not have the freedom to use S_H/S_W as a design variable, since this is already fixed once the duct diameter and chord are determined with the design parameters given in Section 2.1. This effect reduces the number of design variables for the DUUC in the HSE module, and therefore wing positioning becomes an intricate task in the Initiator.

5.4. LONGITUDINAL STATIC STABILITY & CONTROLLABILITY CONSTRAINTS

The LSSC-constraints as given by Equations (5.8 – 5.11), follow from the aircraft longitudinal stability and balance analysis as presented in this section. The equations origin from Torenbeek's X-plot method, and are modified for the DUUC where necessary. In total three critical constraints are identified: sizing for stick fixed longitudinal static stability, sizing for control up to stall, and sizing for control at the take-off rotation.

5.4.1. FREE BODY DIAGRAM

The first step in the moment balance analysis, is to determine all major aerodynamic forces and weights which are relevant for a moment balance. These forces are represented in a free body diagram (FBD). The FBD corresponding to HSE-module for the DUUC is presented in Figure 5.2, which is a modified version of Torenbeek's original FBD for horizontal tail sizing [40]. The difference is that the DUUC includes a significant thrust force (T_H) at the horizontal stabilizer. For the sake of clarity, the terms tail-off (T-O) and tailless aircraft are the same.

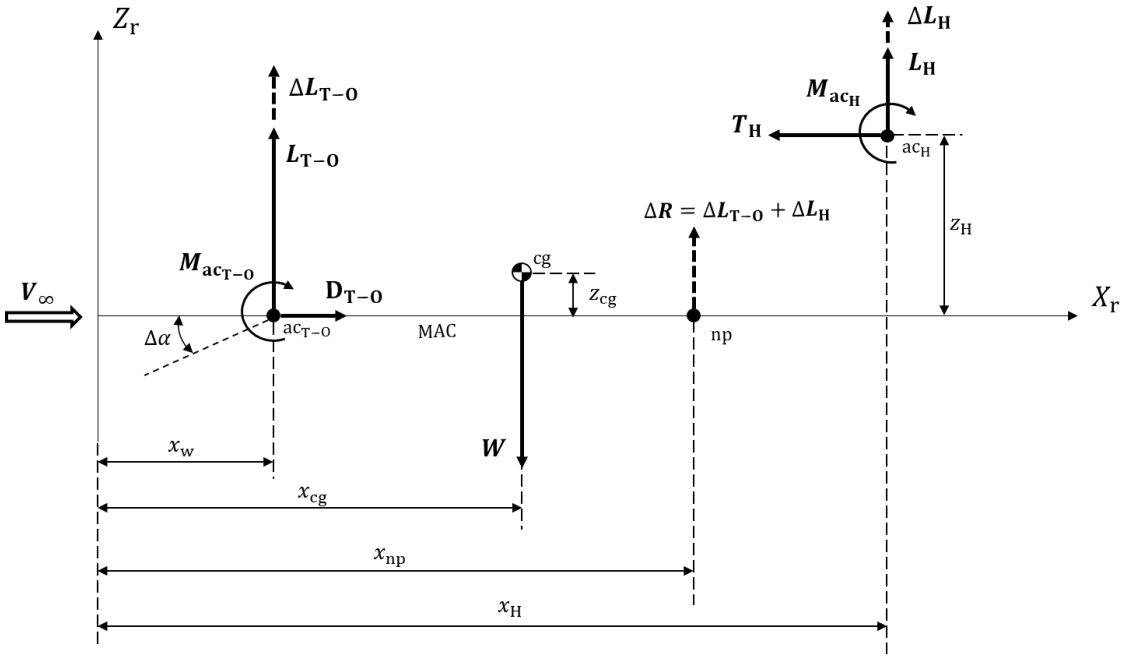

Figure 5.2: DUUC FBD in the vehicle reference frame, including geometric definitions, forces, and moments. Tail-off aircraft contributions indicated with (T-O), and the horizontal stabilizer (DFPE) contributions indicated with H.

The forces and moments given in Figure 5.2 are calculated with [71]:

$$L_{\text{T-O}} = C_{L_{\text{T-O}}} \frac{1}{2} \rho V_\infty^2 S \tag{5.4}$$

$$L_{\text{H}} = C_{L_{\text{H}}} \frac{1}{2} \rho V_{\text{H}}^2 S_{\text{H}} \tag{5.5}$$

$$M_{\text{ac}} = C_{m_{\text{ac}}} \frac{1}{2} \rho V_\infty^2 S \bar{c} \tag{5.6}$$

$$T_{\text{H}} = \frac{\eta_{\text{prop}} P_{\text{tot}}}{V_\infty}. \tag{5.7}$$

By convention the following rules are applied to shorten the equations:

- Any longitudinal point normalized with the mean aerodynamic chord is written as $\frac{x_{\text{i}}}{\bar{c}} = \overline{x}_{\text{i}}$
- Any longitudinal point normalized with the fuselage length is written as $\frac{x_{\text{i}}}{l_{\text{fuselage}}} = \overline{X}_{\text{i}}$

The subscript "i" indicates an arbitrary point.

5.4.2. SIZING FOR STICK FIXED LONGITUDINAL STATIC STABILITY

By definition, to have a longitudinally stable aircraft, the change in moment around the center of gravity due to a small change in angle of attack, should be negative: $\frac{dC_m}{d\alpha} < 0$ [40]. From the moment balance, the c.g. location for stick-fixed neutral stability is expressed by [40]:

$$\overline{x}_{\text{cg}} = \overline{x}_{\text{ac}} + \frac{C_{L_{\alpha_{\text{H}}}}}{C_{L_{\alpha_{\text{T-O}}}}} \left(1 - \frac{d\epsilon}{d\alpha}\right) \frac{S_{\text{H}}}{S} \frac{l_{\text{h}}}{\bar{c}} \left(\frac{V_{\text{H}}}{V}\right)^2 - S.M. \tag{5.8}$$

A static margin of 5% is included as safety factor ($S.M. = 0.05$). Since Equation (5.8) investigates the change in moment balance with a small free-stream disturbance in angle of attack ($\Delta\alpha$), and it is assumed that the thrust force is marginally influenced by this ($\frac{dT}{d\alpha} \approx 0$) [40], the conventional equation can also be applied to the DUUC.

The wing position then has to be chosen in such a manner, that the c.g. position calculated with Equation (5.8) is located after the most aft c.g. location acquired from the aircraft loading diagram, to get a neutrally stable aircraft [40]: $\overline{x}_{\text{cg}_{\text{stability}}} \geq \overline{x}_{\text{cg}_{\text{aft}}}$

5.4.3. SIZING FOR LONGITUDINAL STATIC CONTROLLABILITY (TRIMMING)

To ensure that the aircraft can pitch up to the stall angle of attack in landing configuration, the aircraft should be balanced around its center of gravity, $\circlearrowleft \Sigma M_{\text{cg}} = 0$, which results the following moment balance [40]:

$$\overline{x}_{\text{cg}} = \overline{x}_{\text{ac}} - \frac{C_{m_{\text{ac}}}}{C_{L_{\text{T-O}}}} + \frac{C_{L_{\text{H}}}}{C_{L_{\text{T-O}}}} \frac{S_{\text{H}}}{S} \left(\frac{V_{\text{H}}}{V}\right)^2 \frac{l_{\text{h}}}{\bar{c}} \tag{5.9}$$

By convention, it is assumed that the engines have to be in the power-off configuration in this flight phase [40], hence the DUUC design does not have an influence on the moment balance in this configuration.

The same moment balance can be made for controllability during take-off rotation, where the rotation speed is assumed to be 5% larger than the stall speed ($V_{\text{R}} = 1.05 V_{\text{S}}$), for transport aircraft [40]:

$$\overline{x}_{\text{cg}} = \frac{C_{L_{\text{T-O}}} \left(x_{\text{ac}} - x_{\text{g}}\right) + C^\star_{L_{\text{H}}} \left(x_{\text{H}} - x_{\text{g}}\right) \frac{S_{\text{H}}}{S_{\text{W}}} \left(\frac{V_{\text{H}}}{V}\right)^2 + C_{L_{\text{T-O}}} \left(\frac{V_{\text{S}}}{V_{\text{R}}}\right)^2 \left(x_{\text{g}} - \left(\frac{T_{\text{TO}}}{W}\right) z_{\text{T}}\right) - C_{m_{\text{ac}}} \bar{c}}{C_{L_{\text{T-O}}} \left(\frac{V_{\text{S}}}{V_{\text{R}}}^2\right) \bar{c}} - \frac{x_{\text{LEMAC}}}{\bar{c}} \tag{5.10}$$

The thrust during takeoff is based on the thrust to weight ratio $\left(\frac{T_{\text{TO}}}{W}\right)$, which is for propeller aircraft derived from the power to weight ratio combined with the propulsive efficiency during takeoff (η_{TO}), and rotational velocity (V_{R}). For the take-off rotation, the moment balance is calculated around the landing gear position, $\circlearrowleft \Sigma M_{\text{g}} = 0$. Due to the pitch up during rotation ($\dot{\theta}$), the horizontal stabilizer experiences an upwash, which translates itself into an decreased tail downforce ($C^\star_{L_{\text{H}}}$) determined with [40]:

$$C^\star_{L_{\text{H}}} = C_{L_{\text{H}}} + C_{L_{\alpha_{\text{H}}}} \frac{\dot{\theta} \left(x_{\text{H}} - x_{\text{g}}\right)}{V_{\text{R}}} \tag{5.11}$$

The take-off rotation is based on Torenbeek's assumption of $\dot{\theta} = 3.0°/s$. [1]

For both the control at stall and take-off equations, the DUUC wing position has to be located in such a manner that the calculated c.g. positions are located in front of the most forward c.g. location retrieved from the aircraft loading diagram, to have a controllable aircraft in these flight phases [40]: $\overline{x}_{\text{cg}_{\text{control}}} \leq \overline{x}_{\text{cg}_{\text{forward}}}$

[1] The tail generates a downforce during take-off rotation to give a nose-up moment, so $C_{L_{\text{H}}} < 0$.

5.4.4. BOOKKEEPING OF DFPE PROPERTIES

The basics of the LSSC equations rely on the fact that the horizontal stabilizer, in the case of the DUUC this is the DFPE, should generate an aerodynamic moment around the c.g. of the aircraft, which compensates the aerodynamic moment around the c.g. generated by the tailless aircraft. The lift force generated by the tailless aircraft is mainly generated by the wing, and other contributions to the moment balance, e.g. the fuselage, translate themselves into moment coefficients measured with respect to the a.c. of the tailless aircraft.

In the Initiator, the tail-off moment coefficient around the tail-off a.c. $C_{m_{\text{ac}_{\text{T-O}}}}$ is defined by the contributions of the wing, fuselage, and nacelles [40]:

$$C_{m_{\text{ac}_{\text{T-O}}}} = C_{m_{\text{ac}_{\text{wing}}}} + C_{m_{\text{ac}_{\text{fuselage}}}} + C_{m_{\text{ac}_{\text{nacelles}}}} \tag{5.12}$$

Furthermore, the tailless lift is generated at the location of the tail-off aerodynamic center, which consists of the contributions of the wing, fuselage, nacelles, and thrust [40]:

$$\overline{x}_{\text{ac}} = \left(\frac{x_{\text{ac}}}{\overline{c}}\right)_{\text{wing}} + \left(\frac{x_{\text{ac}}}{\overline{c}}\right)_{\text{fuselage}} + \left(\frac{x_{\text{ac}}}{\overline{c}}\right)_{\text{nacelles}} + \left(\frac{x_{\text{ac}}}{\overline{c}}\right)_{\text{thrust}} \tag{5.13}$$

In both the $C_{m_{\text{ac}_{\text{T-O}}}}$ as the $\overline{x}_{\text{ac}}$ calculations it is seen that the nacelles have a contribution. For conventional aircraft this is no problem, however for the DUUC it raises questions regarding the bookkeeping of certain properties, because at some point thrust related parameters could be mixed with stabilizing surface related parameters, and tail-off parameters could be mixed with tail-only parameters. To solve this problem and to maintain a clear overview of the DFPE properties and their contributions to the performance and balance analysis, the following definition is maintained in the DUUC sizing process:

All DFPE properties which contribute in generating a vertical force caused by a lifting surface are booked under the horizontal stabilizer contributions, and all parameters which contribute in an axial force due to the fan frontal area drag are booked under the propulsion contributions.

For example, because $C_{m_{\text{ac}_{\text{nacelles}}}}$ refers to a drag induced moment caused by the frontal area of the fans multiplied with the vertical offset of the fan centerline with respect to the c.g., see Equation (2.21), this parameter is not coupled to a DFPE downforce and therefore it is booked under $C_{m_{\text{ac}_{\text{T-O}}}}$.

The parameter $\overline{x}_{\text{ac}_{\text{nacelles}}}$ in Equation (5.13) however, refers to the longitudinal contribution of the nacelle to the location of the aerodynamic center [40]:

$$\left(\frac{x_{\text{ac}}}{\overline{c}}\right)_{\text{nacelles}} = \Sigma k_{\text{nacelles}} \frac{b^2_{\text{nacelles}} l_{\text{nacelles}}}{S_{\text{W}} \overline{c} \left(C_{L_\alpha}\right)_{\text{T-O}}} \tag{5.14}$$

The nacelle correction factor in this equation has a value of $k_{\text{nacelles}} = -4.0$ for wing mounted nacelles, and $k_{\text{nacelles}} = -2.5$ fuselage mounted nacelles. The nacelle width (b_{nacelles}) is the same as the outer duct diameter of the DFS (D_{o}). Because the nacelle arm is defined as the longitudinal distance between the TE of the nacelle and the 25% MAC location, it is concluded that this equation refers to a vertical force. Because this effect is already implemented in the tail moment calculation of the DFPE, it is decided that $\overline{x}_{\text{ac}_{\text{nacelles}}}$ =0 in case of the DFPE.

The thrust contribution to the longitudinal location of the tailless aircraft however ($\overline{x}_{\text{ac}_{\text{thrust}}}$) refers to an axial force caused by the fan frontal area [40]:

$$\left(\frac{x_{\text{ac}}}{\overline{c}}\right)_{\text{thrust}} = \left(\frac{x_{\text{ac}}}{\overline{c}}\right)_{\text{nacelles}} - 0.05 N_{\text{bl}} D^2_{\text{fan}} \frac{x_{0.25\overline{c}} - x_{\text{fan}}}{S_{\text{W}} \overline{c} \left(C_{L_\alpha}\right)_{\text{T-O}}} \tag{5.15}$$

Because this equation refers to a thrust offset caused by the fan frontal area, it is decided to book this parameter under $\overline{x}_{\text{ac}}$.

5.5. DUUC WING-POSITIONING

Now the LSSC-equations are derived, they need to be combined into a single diagram to determine the ideal wing-location which is required to satisfy the the c.g. conditions. Since the tail-wing area ratio ($S_{\text{H}}/S_{\text{W}}$) for the DUUC is not a variable in this method because of the fixed DFPE geometry, only the tail arm (l_{h}) and therefore the wing location can be modified. This section explains how the DUUC's wing is positioned, such that it satisfies the LSSC requirements.

5.5.1. GENERAL PROCEDURE

Although the DUUC wing-positioning method has similar characteristics compared to Torenbeek's method, it is still valuable to explain step-by-step how it is done. The DUUC wing-positioning procedure is visualized in a flow diagram, see Figure 5.3.

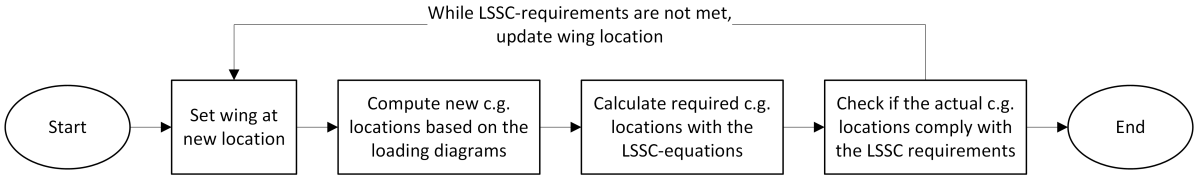

Figure 5.3: Flow diagram for DUUC wing positioning, with the horizontal stability estimation module

The base for the DUUC wing-positioning relies on the calculations of the $\overline{x}_{cg}$ points determined with the LSSC-equations, see Equations (5.8 – 5.11). Because tail to wing area ratio (S_H/S_W) is fixed due to the DFPE geometry, the only free variable in the equations is the tail arm (l_h), which can be varied by modifying the wing location ($X_{WingApex}/L_{fuselage}$). The wing position ($X_{WingApex}/L_{fuselage}$) is a design variable within the Initiator, and corresponds to the longitudinal location of the LE of the wing root measured from the nose of the aircraft, normalized with the fuselage length. For further reference, this parameter is denoted as $\overline{X}_{LE_{wing}}$.

For each new wing position, firstly the actual forward and aft c.g. locations are acquired via the aircraft loading diagrams, see Figure 5.4 for an example. Because of the new wing-position, both the OEM c.g. and the MAC locations change, and therefore the limit c.g. locations change with respect to the leading edge of the mean aerodynamic chord. Secondly, the required $\overline{x}_{cg}$ locations are calculated with Equations (5.8 – 5.11).

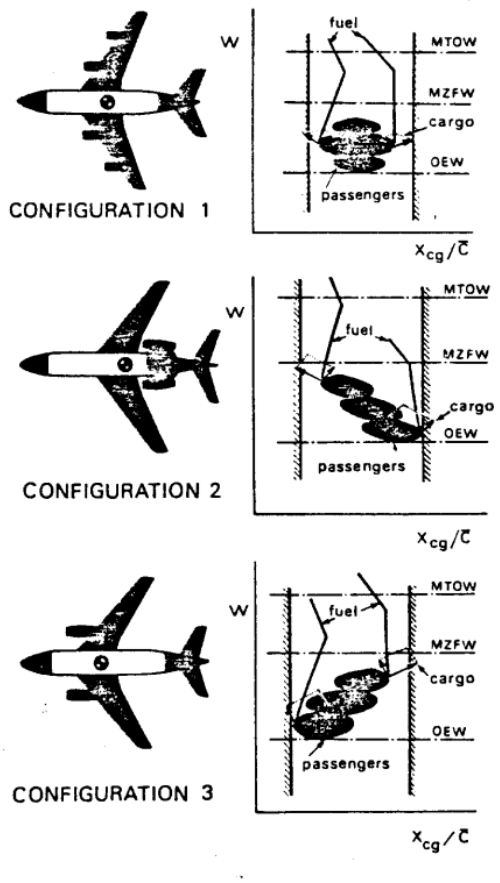

Figure 5.4: Example of aircraft loading diagram, given for various aircraft configurations [40]. Diagram shows weight versus longitudinal c.g. location normalized with the MAC $\left(\frac{x_{cg}}{\bar{c}} = \overline{x}_{cg}\right)$.

This procedure is executed for three wing locations: $\overline{X}_{\text{LE}_{\text{wing,init}}}$, $\overline{X}_{\text{LE}_{\text{wing,init}}} + 0.05$, and $\overline{X}_{\text{LE}_{\text{wing,init}}} - 0.05$. This procedure is visualized in Figure 5.5. By interpolating the $\overline{x}_{\text{cg}}$ locations for all wing positions in this figure, the final wing-positioning plot is resulted in figure 5.6.

In contrary to Torenbeek's X-plot, the DUUC wing-positioning plot directly shows what the effect of the new wing-position is on the limit c.g. locations resulting from the loading diagram, and the required c.g. locations calculated with the LSSC-equations. The X-plot however only shows the variation of the c.g. locations calculated with the LSSC-equations, with the variable tail area ratio, for one wing position.

5.5.2. WING-POSITIONING PLOT

An aircraft designer should use the wing-positioning plot depicted in Figure 5.6 in such a manner, that it determines the wing location ($\overline{X}_{\text{LE}_{\text{wing}}}$) where all control lines are in front of the most front c.g. line, and that the neutral stability line including static margin lies beyond the most aft c.g. line.

In Figure 5.6 it is seen that the design space for feasible wing locations is always bound by an upper and lower limit. Because mainly the vertical axis in the wing-positioning diagram is relevant for the longitudinal positioning of the wing, the vertical distance in the design space determines the freedom for the aircraft designer to place the wing. The vertical distance in the design space is denoted with $\Delta\overline{X}_{\text{LE}_{\text{wing}}}$.

In this example wing-positioning plot presented in Figure 5.6, the upper limit is bound by the wing location which corresponds to the intersection of the lines which represent *"control at stall"*, and the *"forward c.g. location"*. The lower bound is determined by the wing location which corresponds to the intersection of the lines which represent *"neutral stability including static margin"*, and the *"aft c.g. location"*. The distance between these bounds forms the feasible wing positioning design space, where the conditions $\overline{x}_{\text{cg}_{\text{control}}} \leq \overline{x}_{\text{cg}_{\text{forward}}}$ and $\overline{x}_{\text{cg}_{\text{stability}}} \geq \overline{x}_{\text{cg}_{\text{aft}}}$ are met.

In the traditional wing positioning method, the wing is positioned where it results a minimal c.g. shift. However, since the DUUC experiences a large c.g. shift between its OEM and MTOM configuration, the traditional method is not sufficient to result in a good design in terms of LSSC. Based on the feasible wing positioning design space in Figure 5.6, the aircraft designer needs to define criteria which results in a protocol which places the wing at an ideal location. This can be on the upper or lower bound of the design space, or somewhere in the middle.

In case the aircraft designer chooses the stability constraint as active, the wing would be positioned at the upper bound of the design space. Therefore the wing would be placed more aft, which decreases the tail arm. With a decreased tail arm the DFPE should generated a larger lift to compensate the tailless aerodynamic moment around the c.g. A larger lift force, is inherent in a larger trim drag. So therefore it is advised to maximize the tail arm, to minimize the trim drag.

In case the aircraft designer chooses the stall constraint as active, the wing would be positioned at the lower bound of the design space. Therefore the wing would be placed more front, which increases the tail arm, and therefore it reduces the trim drag. To have a robust protocol for ideal wing positioning, which first of all maximizes the tail arm by placing the wing as much forward as possible, and secondly which ensures that the aircraft is always controllable in the worst case stall condition (landing configuration), it is decided that the wing should be be positioned at the intersection of the *"control at stall"* line. Since modern aircraft can be neutrally stable, or even instable in combination with an active stability augmentation system, an aircraft designer can choose to give more value to the stall constraint than the neutral stability constraint. The benefit of this method is that the aircraft design will always comply to the stall constraint, however the aircraft stability constraint is therefore ignored.

In order to have a feasible design space, it is essential that the upper bound in the wing-positioning plot is always determined by the stability constraint. As it will become clear during the sensitivity analysis in the results chapter, for the situation where the DFPE is too small it results that the control bound is placed above the stability bound, indicating that a more aft wing location is preferred. Based on the above mentioned wing-positioning protocol, the wing is always placed at the *"control at stall bound"*. This results that for the situation with an infeasible design space the aircraft will be able to balance itself in the critical stall at landing condition, however it will instable.

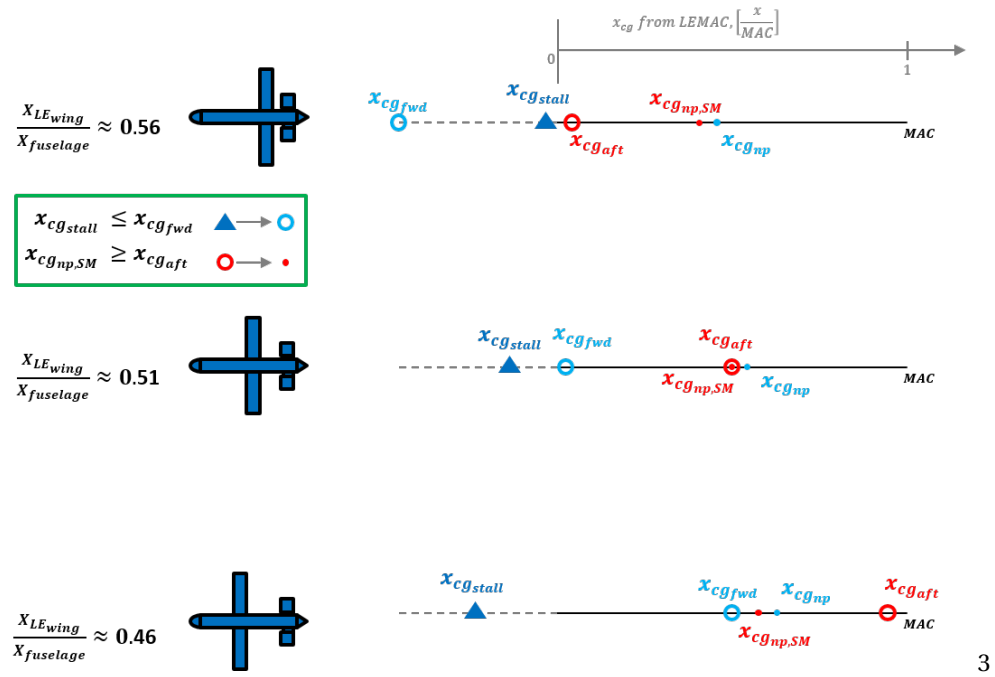

Figure 5.5: DUUC wing-positioning method relies on the calculations of the required $\overline{x}_{cg}$ points determined with the LSSC-equations, and the actual forward/aft $\overline{x}_{cg}$ locations, per wing position

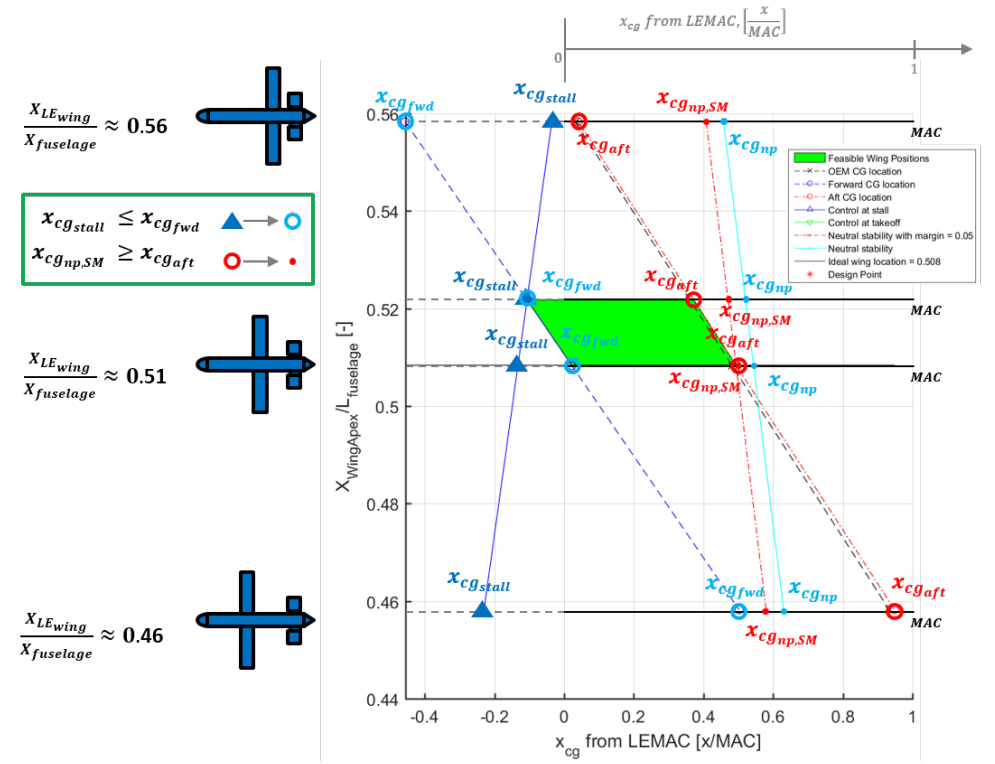

Figure 5.6: Example of the DUUC wing-positioning plot with the Initiator HSE-module. The active constraint for the wing positioning in this figure is "neutral stability including static margin". All wing positions within the highlighted design space give feasible aircraft designs, based on the LSSC-equations. The take-off constraint is further left in the graph, therefore it is not depicted in the current domain.

5.6. TRIMMING

The final piece of the puzzle is to include the trim drag into the aircraft lift drag polar. Normally the Initiator uses AVL [72] to determine the lift and induced drag of all lifting surfaces during the cruise flight, including trim drag. These results are then used in the mission analysis simulation module to compute the lift and drag forces, and therefore the thrust and required fuel consumption. Unfortunately, AVL is only valid for thin planar wing planforms, and is therefore not able to model ring-wings or ducted fans.

The solution for the DUUC's trim drag calculation is to use the trim diagram which follows from the HSE module in the Initiator, and to use the trim diagram to calculate the required tail lift, which is then converted into trim drag.

5.6.1. TRIM DIAGRAM

An example of the trim diagram is found in Figure 5.7. A trim diagram combines the aerodynamic moment of the tailless aircraft during various critical flight conditions and c.g. locations, including at which tailless lift coefficient this moment is generated, and shows the required tail lift which is required to compensate for the tailless aerodynamic moment.

For example, in Figure 5.7 the situation which causes the largest nose down tailless aerodynamic moment around the aircraft c.g. ($C_{m_{cg}} < 0$)[2], is the landing configuration with maximum flaps combined with the most forward c.g. This configuration results in $C_{m_{cg}} = -0.78$ on the upper horizontal axis, at a tailless lift coefficient of $C_{L_{cg}} = 3.3$ at the vertical axis. The tail lift which is required to trim the aircraft, hence to compensate for $C_{m_{cg}} = -0.78$ is $C_{L_H} = -0.78$ on the lower horizontal axis.

The benefit of a trim diagram is that a designer can see if the tail is capable of trimming the aircraft for all extreme values of $C_{m_{cg}}$. The disadvantage of the DUUC, is that the tail lift C_{L_H} strongly depends on the thrust setting, i.e. more thrust results in more tail lift, as described in Section 2.3.3. Hence for takeoff different limits exist than for the cruise phase and landing stall configurations.

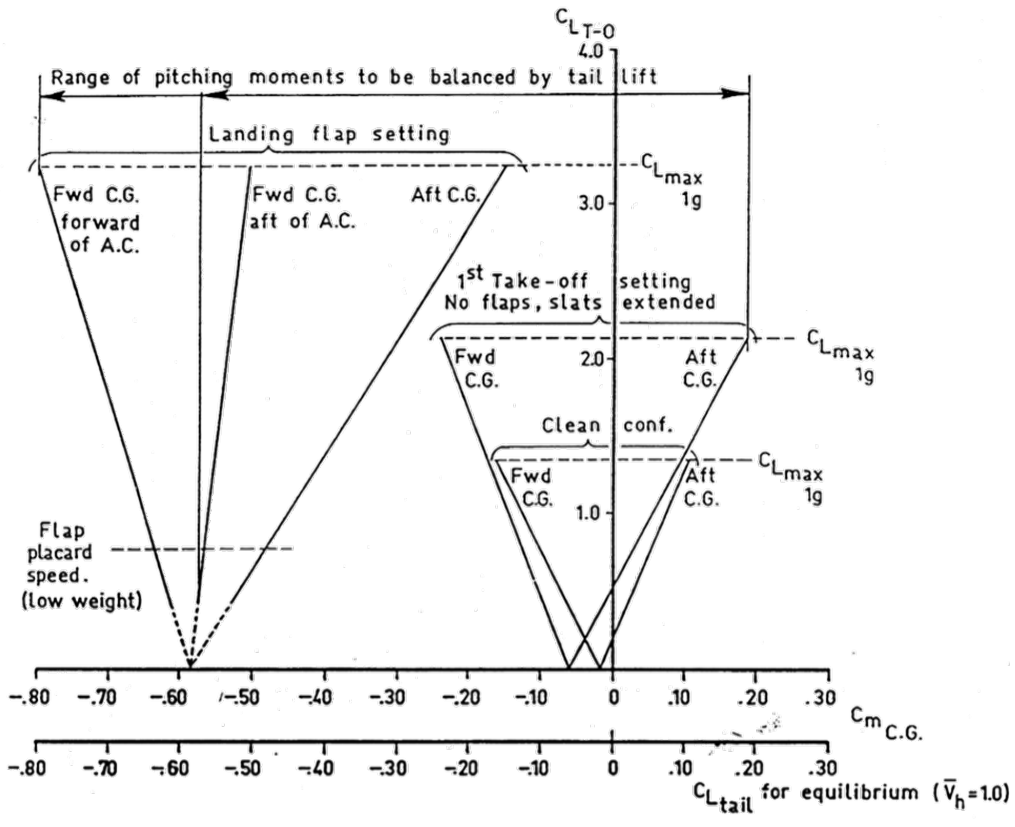

Figure 5.7: Pitching moment, aircraft less tail. Flap placard speed = maximum speed at which aircraft is allowed to fly with flaps deployed [73]

[2] In Figure 5.7 the tailless aerodynamic moment $C_{m_{T\text{-}O}}$ is written as $C_{m_{cg}}$. These are the same, since the tailless aerodynamic moment is calculated with respect to the c.g.

5.6.2. TRIM DRAG

To determine the trim drag of the DUUC a superposition method is applied. This means that the DFPE induced drag is based on the required tail lift, which is required to keep the aircraft in steady symmetric horizontal cruise flight. This required tail lift, follows from the trim diagram.

To simplify the equations, it is assumed that the c.g. shift during flight is small for straight-wing aircraft ($\Delta\overline{x}_{cg_{flight}} \lesssim 0.01$), such that the moment arms corresponding to the wing and tail lift forces do not change. By doing so, it is possible to directly use the linear relation between C_{L_H} and $C_{L_{T\text{-}O}}$, by taking one of the bounds of the trim drag triangle which corresponds to the cruise flight. In the case of the most forward c.g. this is the left bound, and in case of the most aft c.g. it is the right bound, see Figure 5.7. Because it is most likely that the loaded aircraft shifts the c.g. more front compared to the OEM c.g., it is assumed that the forward c.g. bound in the trim diagram can be taken. Verification with the aircraft loading diagram is required to confirm this assumption, which is done in Section 6.2. Without making the assumption that the c.g. location varies insignificantly small during flight, the equations given in the next paragraphs should include the longitudinal c.g., which requires more computational effort.

From the aircraft trim diagram, see Figure 5.7, it follows that there exists a linear trend between the tail-off lift, and the required tail downforce to maintain a moment balance. This linear relation is defined by:

$$C_{L_H} = \left(\frac{dC_{L_{T\text{-}O}}}{dC_{L_H}}\right) C_{L_{T\text{-}O}} + C_{L_{H_0}} \tag{5.16}$$

The lift and drag of the DFPE is generated by the combination of the DFS and pylon, and therefore a weighted average should be applied. The tail lift calculated with Equation (5.16) is based on the weighted average of the lift forces generated by the DFS and pylon:

$$C_{L_{DFS}} = C_{L_H}\left(\frac{S_{H_{DFS}}}{S_{H_{proj}}}\right) \tag{5.17}$$

$$C_{L_{pylon}} = C_{L_H}\left(\frac{S_{H_{pylon}}}{S_{H_{proj}}}\right) \tag{5.18}$$

The corresponding lift induced drag components of the DFS and pylon are computed with $C_{D_i} = \frac{C_L^2}{\pi ARe}$ [46]:

$$C_{D_{i_{DFS}}} = \frac{C_{L_{DFS}}^2}{\pi\,(AR_{duct})\,(e_{DFS})} \tag{5.19}$$

$$C_{D_{i_{pylon}}} = \frac{C_{L_{pylon}}^2}{\pi\left(AR_{pylon}\right)\left(e_{pylon}\right)} \tag{5.20}$$

Research by Harinarain showed that the Oswald efficiency factor $e_{DFS} = 2$ for ducted fans [43]. For the pylon, it is assumed that has similar properties to a symmetric planar wing, and therefore it is assumed that $e_{pylon} = 0.95$ [46]. The lift induced drag of the horizontal stabilizer, or DFPE trim drag becomes:

$$C_{D_{i_H}} = \frac{C_{D_{i_{DFS}}} S_{H_{DFS}} + C_{D_{i_{pylon}}} S_{H_{pylon}}}{S_{H_{proj}}} \tag{5.21}$$

The resulting lift induced drag is added to the friction horizontal stabilizer friction drag, which results in the total drag of the horizontal stabilizer:

$$C_{D_H} = C_{D_{0_H}} + C_{D_{i_H}} \tag{5.22}$$

Now the lift and drag of the horizontal stabilizer is computed, the results should be combined with the tail-off results to arrive at the trimmed aircraft lift and drag coefficients. This is not simply adding only the tail trim drag results to the existing tail-off lift drag polar, because then the total lift is not corrected for the tail downforce. The solution to this involves combining Equations (5.16 – 5.21, which ensure that the final lift drag polar includes the trim drag of the DFPE, and that the lift and drag values are corrected to ensure that lift equals weight is maintained during cruise flight.

The total aircraft lift is defined as:

$$L_{tot} = L_{T\text{-}O} + L_H \tag{5.23}$$

And in its full form:

$$C_L \frac{1}{2}\rho V^2 S_W = C_{L_{T\text{-}O}} \frac{1}{2}\rho V^2 S_W + C_{L_H} \frac{1}{2}\rho V_H^2 S_H \tag{5.24}$$

Dividing both sides by $\frac{1}{2}\rho V^2 S_W$ yields:

$$C_L = C_{L_{T\text{-}O}} + C_{L_H} \left(\frac{V_H}{V}\right)^2 \frac{S_H}{S_W} \tag{5.25}$$

Via a similar procedure the drag is calculated:

$$C_D = C_{D_{T\text{-}O}} + C_{D_H} \left(\frac{V_H}{V}\right)^2 \frac{S_H}{S_W} \tag{5.26}$$

An example of the tail-off versus the trimmed drag polar is shown in Figure 5.8. For example, the figure shows that there would be a ±15% difference in drag for a cruise lift coefficient of $C_{L_{cruise}} = 1.3$. Neglecting the trim drag would result in an overestimated lift-to-drag ratio, which underestimates the fuel consumption. Therefore it essential to included the trim drag for any aircraft, including the DUUC.

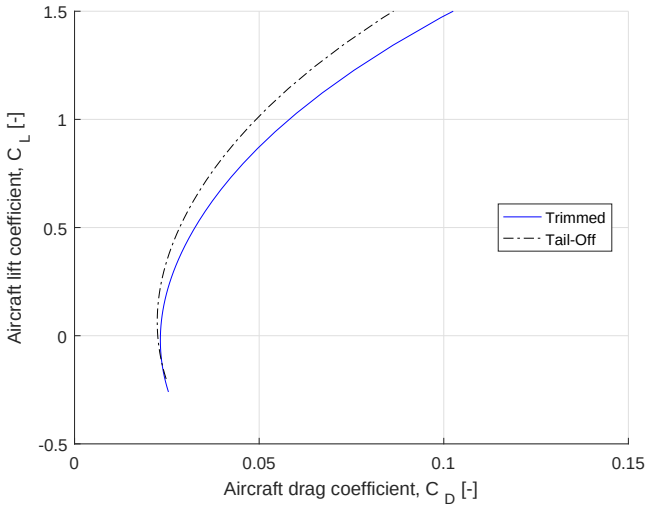

Figure 5.8: Example DUUC drag polar comparison of trimmed versus tail-off aircraft. Figure is based on DUUC baseline model.

The disadvantage of the DUUC lift-drag polar superposition method, is that the tail trim force calculation is based on the cruise lines in the trim diagram, which are based on the c.g. location during cruise, which follows from the MTOM configuration. This means that if the aircraft would fly its ferry mission, the c.g. would be too far aft, and therefore the above described method would not work anymore.

6

Results & Discussion

This chapter discusses the results of the research on the DUUC synthesis process. All results in this chapter are acquired via the Initiator. Because of the previous research within the Initiator development group on the ATR72-600, see Figure 6.1, it is decided to continue with this aircraft. Therefore, the Initiator model of the ATR72-600 reference aircraft and DUUC are based on the mission requirements of the actual ATR72-600, which are presented in Table 6.1.

Figure 6.1: Actual model of the ATR72-600 [37]

Table 6.1: Top level mission requirements for the harmonic mission, based on the ATR72-600 [37]

Parameter	Unit	Value
Payload mass (68 pax)	kg	7500
Range at max payload	km	1528
Design Cruise Altitude	m	7500
Design Cruise Mach	-	0.45

This chapter firstly discusses the results of the ATR72-600 model in Section 6.1, including a comparison to the actual aircraft. This is followed by the results of the DUUC baseline model, presented in Section 6.2, including a comparison with the ATR72-600 Initiator model.

Throughout the DUUC design process, various assumptions were made to complete for instance the aerodynamic, structural, and mass calculations. Each of these assumptions has a certain impact on the converged result of the Initiator. Furthermore, a set of key design parameters (M_{tip}, RPM, AR_{duct}) exists which determine the size of the DFPE. To study the effects of these parameters on the total aircraft design, a sensitivity study is performed. The results of these analysis are given in Section 6.3.

To clarify, all comparisons done between the DUUC and ATR72-600 refer to the Initiator models, since then it is clear to compare these aircraft because they are designed with similar methods within the Initiator. The KPIs are: MTOM, OEM, fuel fraction, and total aircraft drag. The fuel fraction is defined as the fuel mass divided by the MTOM. Furthermore, all performance results are presented for the harmonic mission [1].

Most KPI results in the sensitivity analysis are presented as relative differences compared to KPIs of the Initiator ATR72-600 model. The exact values of all Initiator analysis are shown in Appendix H.

[1] The range corresponding to the maximum payload mass and MTOM refers to the harmonic range. The maximum range with maximum fuel capacity refers to the ferry range.

6.1. REFERENCE AIRCRAFT VALIDATION

In this section the converged Initiator model of the ATR72-600 reference aircraft is discussed, where its KPIs are compared to those of the actual aircraft. The geometries of the ATR72-600 model are presented in Figure 6.2, and the KPI comparison is given in Table 6.2.

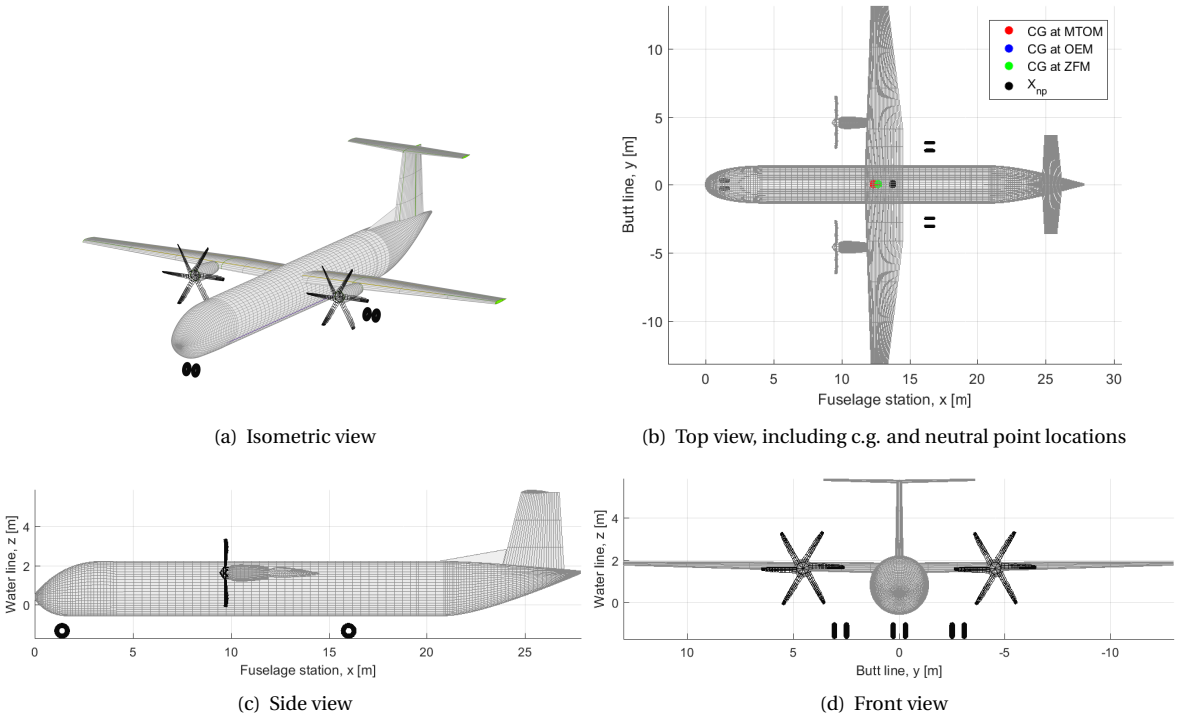

(a) Isometric view

(b) Top view, including c.g. and neutral point locations

(c) Side view

(d) Front view

Figure 6.2: ATR72-600 baseline model geometry, made with the Initiator

Table 6.2: Comparison of reference aircraft and Initiator model of the ATR72-600. Reference data is retrieved from Janes All the Worlds Aircraft [37].

		ATR72-600 Model Validation		
Parameter	**Unit**	*Reference*	*Initiator*	*Difference*
MTOM	kg	22800	22300	-2.2%
OEM	kg	13311	13200	-0.8%
Harmonic fuel	kg	1989	1550	-22.1%
Harmonic fuel fraction	-	0.0872	0.0695	-20.0%
Fuel efficiency	g/pax/km	19.1	14.9	-22.1%
Power loading	N/W	0.0606	0.0497	-18.0%
Wing loading	N/m^2	3667	3790	+3.4%
Engine T-O power	kW	3692	4400	+19.2%
Wing surface area	m^2	61.0	57.6	-5.5%

6.1.1. PROPELLER PERFORMANCE

The ATR72-600 is equipped with two turboprops, each featuring a Hamilton Standard F568 propeller [37], see Figure 2.2. The performance of the F568 is retrieved from an extensive propeller performance study by Filippone [47]. The propulsive performance is presented in Figure 6.3. [2]

Because the propeller map was already available, it was easier to digitize this plot than to use PAP to calculate the performances for the F568 propeller. The F568 rotates at 1200RPM, and has a diameter of 3.93m [37]. From the cruise conditions stated in Table 6.1, it follows that the cruise airspeed is V_∞ =140m/s. Using

[2] The advance ratio used in this figure is normalized with 2π compared with Equation (2.4).

Equation (2.4), this results in $J_{\text{cruise}} = 1.78$. After normalizing J_{cruise} with 2π a value of 0.28 is found. Interpolating with $J = 0.28$, Figure 6.3 results a propulsive efficiency of $\eta_{\text{cruise}} = 0.85$. Calculating the velocity at the take-off rotation gives $V_R = 55.7$m/s, which yields $J_{TO} = 0.71$, and 0.11 after normalizing it with 2π. Interpolating at $J = 0.11$ in Figure 6.3 gives $\eta_{TO} = 0.65$. However, due to an underestimated power loading, which is explained in the next section, it was required to use $\eta_{TO} = 0.70$ to allow the aircraft to take-off within its predefined take-off runway length. The climb advance ratio is based on the average of $J_{\text{T-O}}$ and J_{cruise}. This yields $J_{\text{climb}} = 0.20$, and $\eta_{\text{climb}} = 0.80$ after interpolation in Figure 6.3. The propeller performances are used as settings within the Initiator, since some calculations or methods require the efficiency for a specific flight phase, so therefore the calculated propulsive efficiencies can easily be used in the Initiator.

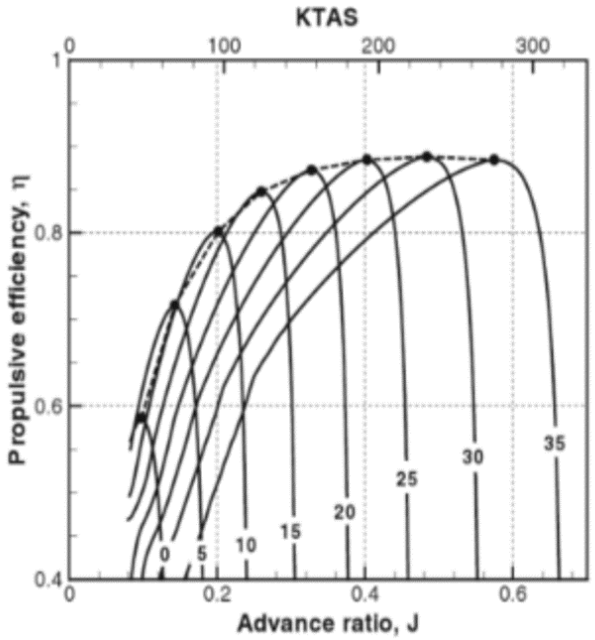

Figure 6.3: Performance of the F568 propeller [47] The the advance ratio is normalized with 2π

6.1.2. GENERAL COMMENTS ON FINAL RESULT

Table 6.2 shows that the ATR72-600 is within 2.2% difference in MTOM, OEM, compared to the actual aircraft. The fuel mass, and therefore the fuel fraction, is about 20% off compared to the reference aircraft. The origin of this large discrepancy is firstly caused by an underestimated power loading. Currently the design point in the wing-power loading estimation is limited by the FAR 25.121d regulation, which calculates the required power loading to meet the climb gradient of 2.1% during a balked landing, with one engine inoperative (OEI), see Figure 6.4. An underestimated power loading results in higher engine power, which have a higher fuel consumption. This phenomena is present for both the ATR72-600 and DUUC models, so the relative difference between the aircraft is not affected by it. However, larger engines are heavier which shift the DUUC OEM c.g. more aft, which eventually results in a higher trim drag. The power loading discrepancy is being researched in another Initiator thesis to propeller sizing, and therefore it is decided to continue the aircraft comparison for the DUUC with an underestimated power loading.

Secondly, the fuel mass of all turboprop aircraft within the Initiator are calculated based on a look-up table which uses the altitude, airspeed, and available shaft power at a certain altitude, to determine the corresponding fuel flow. This look-up table is based on the PW127 turboprops, which are installed in the ATR72-600 [37]. Unfortunately this look-up table is not scalable with the engine geometry and power, which introduces errors in the fuel flow calculation when larger/smaller turboprop engines are used in the Initiator. At this moment, a new Initiator thesis is started which focuses on improving the engine performance models of turbofan and turboprop aircraft, so therefore it is decided to continue the aircraft comparison for the DUUC with the current fuel flow look-up table.

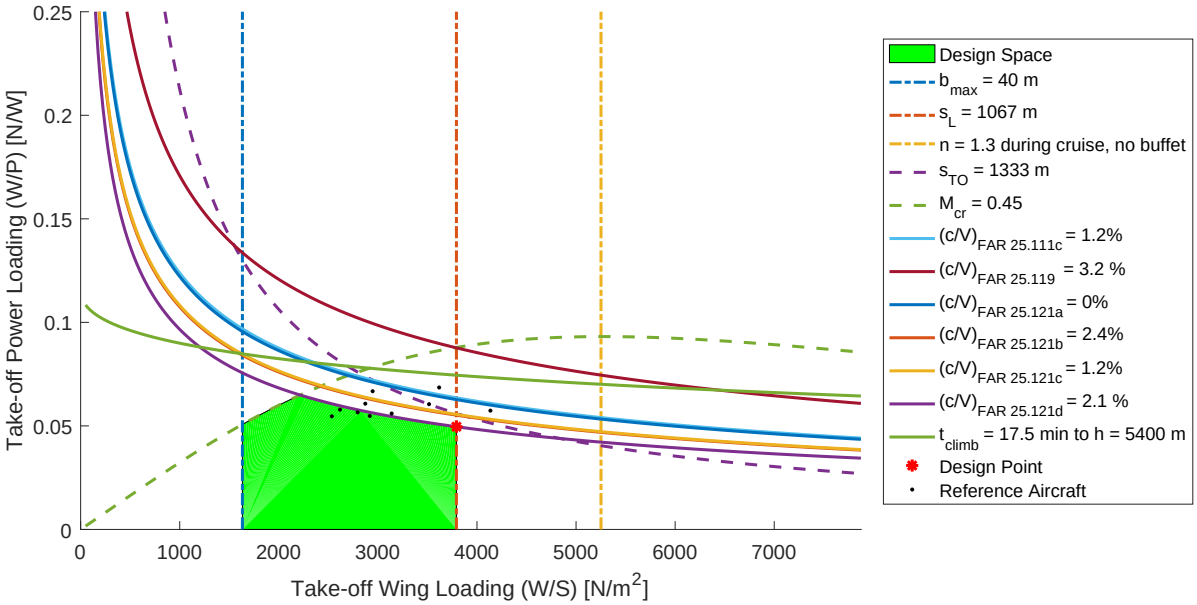

Figure 6.4: Design point for the ATR72-600 in the wing-power loading diagram

6.1.3. CLASS 2 WEIGHT ESTIMATION

The masses of the aircraft components are computed with Torenbeek's Class 2 Weight Estimation method [40]. The mass breakdown is given in Figure 6.5. The wing mass is computed with EMWET, a semi-empirical method which determines the wing mass based on the critical static lift loads which act upon the wing structure [74]. Unfortunately no component mass data of the ATR72-600 is available, however Obert provides component mass data of the ATR42 [73], which is basically a shortened version of the ATR72. The breakdown of the ATR42 is presented in Appendix G.

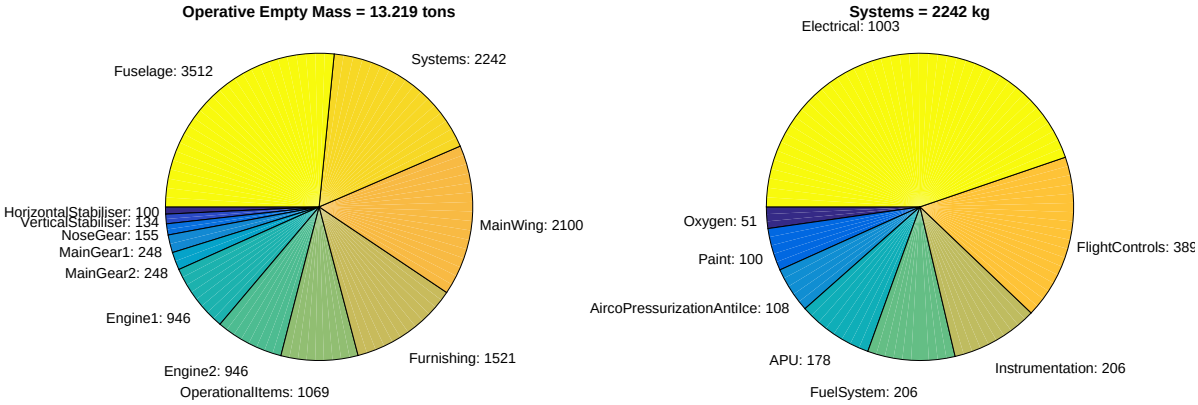

Figure 6.5: Class 2 mass estimation breakdown for the ATR72-600 using Torenbeek and EMWET mass estimation methods. Masses are given in [kg]

A remarkable result, is the fact that both the horizontal and vertical tail areas seem too low compared with the rest of the aircraft. According to Obert, the masses of the horizontal and vertical stabilizer are 220kg and 322kg respectively, however the Initiator predicts masses which are about 50% lower. A probable cause for this significant discrepancy is due to the fact that the Initiator sizes the tail based on the volume coefficient method, as described in Section 5.1. The tail volumes of the actual ATR72-600 are $\overline{V}_H = 1.05$ and $\overline{V}_V = 0.1195$ [75] for the horizontal and vertical stabilizer respectively. Since these parameters are settings in the Initiator, and the HSE-module is not active for turboprop aircraft, the tail volume coefficients are not updated throughout the convergence process. Furthermore, because of the T-tail configuration of the ATR72-600, the position of the horizontal stabilizer is determined by the position of the vertical stabilizer. Based on the LE sweep angle of the vertical stabilizer, the horizontal stabilizer is positioned accordingly.

Because the longitudinal positions of the wing and vertical tail are settings in the Initiator, the horizontal tail surface area S_H follows immediately from the wing and vertical tail geometries in combination with $\overline{V}_H$. If the tail volume coefficient method results an under-predicted value for S_H, the mass of the horizontal stabilizer is also under-predicted, see Equations (F.4) and (F.4) in Appendix F.

In contrary to the wing mass estimation method, EMWET is not used to make a more accurate estimate of the horizontal and vertical stabilizers. The reason for this, is that the student version of EMWET is designed to compute the masses of a wing only. It uses a structural analysis method to compute the design including mass of the primary wing structure (i.e. the wingbox including stringers, spars, webs), to ensure that the stresses in the wingbox do not exceed the maximum allowed material stresses, given the maximum loads which act upon the wing structure. Then, an empirical relation is used to compute the masses of the secondary wing structures, such as spoilers, flaps, etc. [74]:

$$W_{\text{wing}} = 7.6221 \left(W_{\text{wingbox}}\right)^{0.8509} \tag{6.1}$$

The correlation factors used in this equation are based on a regression analysis of various transport aircraft. To apply the same equation to the horizontal and vertical stabilizers, a similar regression analysis should be applied. Unfortunately such data is not available within the Initiator. Furthermore, performing a detailed weight estimation analysis of the horizontal and vertical tail surfaces does not lie within the scope of this thesis research, since the ATR72-600 is merely used to have a baseline aircraft performance model. Additionally, the relevant KPIs (MTOM, OEM, fuel mass) are within acceptable accuracies, so therefore it is not necessary to update the mass estimation methods of the horizontal and vertical stabilizers.

6.2. DUUC BASELINE & COMPARISON ATR72-600

In this section the converged Initiator model of the DUUC baseline model is discussed, where its KPIs are compared to those of the ATR72-600 Initiator model. The geometries of the DUUC baseline model are presented in Figure 6.6, and the KPI comparison is given in Table 6.3.

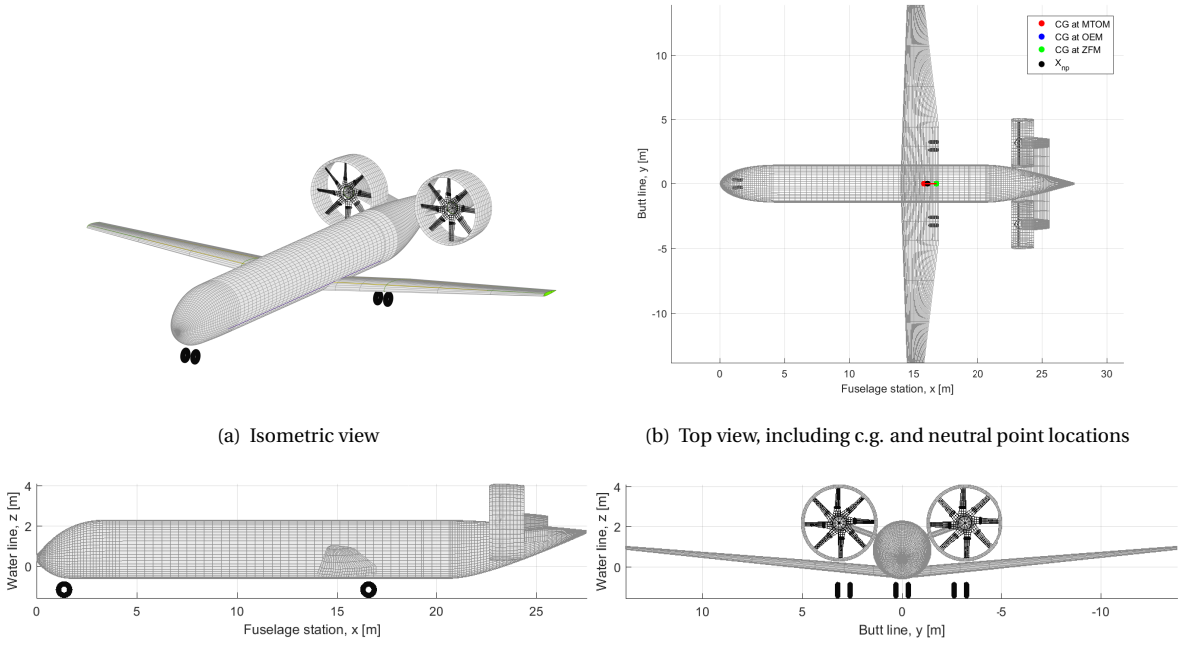

(a) Isometric view

(b) Top view, including c.g. and neutral point locations

(c) Side view

(d) Front view

Figure 6.6: DUUC baseline model geometry, made with the Initiator. $AR_{duct} = 2.0$, $RPM = 1500$, $D_{fan} = 3.48m$, $c_{duct} = 1.74m$.

Table 6.3: Comparison of the Initiator DUUC with the ATR72-600 model.

		Initiator Baseline Models		
Parameter	**Unit**	**ATR72-600**	**DUUC**	*Difference*
MTOM	kg	22300	24800	+11.2%
OEM	kg	13200	15500	+17.4%
Harmonic fuel	kg	1550	1750	+12.9%
Harmonic Fuel fraction	-	0.0695	0.0705	+1.5%
Fuel efficiency	g/pax/km	14.9	16.8	+12.9%
Power loading	N/W	0.0497	0.0504	+1.4%
Wing loading	N/m^2	3790	3800	+0.3%
Engine T-O power	kW	4400	4820	+9.5%
Wing surface area	m^2	57.6	64.1	+11.1%
$\overline{X}_{LE_{wing}}$	-	0.420	0.508	+20.1%
Fuselage length	m	27.8	27.5	-1.2%
Fuselage diameter	m	2.8	2.9	+5.2%
$l_h/L_{fuselage}$	m	0.46	0.30	-34%

6.2.1. PROPELLER PERFORMANCE

In theory the developed propeller analysis program could be used to determine the performances of the DUUC's propulsion system, and the output of the program is formatted in such a manner that it is easily implementable in the Initiator. However, the disadvantage of PAP is that it requires a detailed input model of the propeller blade geometries to determine the local lift and drag components of the blade sections. Unfortunately, the design of the propeller blades is an intricate task which is often done at the end of the aircraft design phase [40]. Hence PAP could not be immediately used to calculate the propulsive performance of the DFS, because no sizing methods for the propeller blades exist in the Initiator. This research is part of another Initiator thesis, which started much later than when the DUUC research was initiated.

Another possibility is to use the F568 propeller blades and to implement it inside an arbitrary duct. Unfortunately this will not give valid output, because the propeller blade geometry of an unducted fan is designed for different flow conditions than for a ducted fan.

To solve this problem, the propulsive efficiencies of the DUUC are based on those of the F568 propeller, see Figure 6.3. To include the increased static thrust effects of ducted fans, it is assumed that the take-off efficiency of the DFS is 10% higher compared to the F568, based on the findings of Black et. al. [7] The resulting propulsive efficiencies for the ATR72-600 and DUUC baseline models are presented in Table 6.4.

Table 6.4: Assumptions for propulsive efficiencies for the ATR72-600 and DUUC

η_{prop}	**ATR72-600**	**DUUC**
Take-off	0.70	0.80
Climb	0.80	0.80
Cruise	0.85	0.85

6.2.2. GENERAL COMMENTS ON FINAL RESULT

On the first sight by investigating the results in Table 6.3, the DUUC baseline model shows to have +17.4% OEM, +12.9% fuel mass, and +11.2% MTOM compared to the ATR72-600 model. The reasons for this are explained in more detail later in this section.

Another interesting fact is that the design point of the DUUC is slightly different in terms of the power loading, compared to the ATR72-600 model. The wing loading is only +0.3% different, however the power loading is +9.5%, see Figure 6.7. For both the ATR72-600 as the DUUC the power loading is constraint by the FAR25.121d requirement, which corresponds to the required power loading to meet the climb gradient of 2.1% during a balked landing, with one engine inoperative (OEI). In the first iteration of both aircraft they have the same power loading, however throughout the design convergence the lift to drag ratio is acquired via the aerodynamic modules based on the aircraft specific geometries, and therefore the lift to drag ratio gets updated in the next iteration of the wing power loading diagram.

All power loading constraints of the wing-power loading diagram corresponding to the take-off phase are calculated with [42]:

$$\left(\frac{W}{P}\right)_{\text{climb}} = \frac{\eta_{\text{prop}_{\text{climb}}}}{RoC + \sqrt{\frac{W}{S}\frac{2}{\rho_0}\frac{C_D^2}{C_L^3}}} \tag{6.2}$$

The rate of climb (RoC, [m/s]) is calculated with [42]:

$$RoC = V \cdot \gamma_{25.121\text{d}} \tag{6.3}$$

The climb gradient corresponding to the FAR 25.121d regulation is $gamma = 2.1\% = 0.0021$. The airspeed at which the rate of climb is calculated is determined with [42]:

$$V_{\text{climb}} = \sqrt{\frac{2}{\rho_0}\frac{W}{S}\frac{1}{C_L}} \tag{6.4}$$

The lift and drag coefficients are acquired from the total aircraft lift-drag polar. Because the DUUC has $C_D^2/C_L^3 = 0.0049$ and the ATR72-600 has $C_D^2/C_L^3 = 0.0056$, the power loading of the DUUC is slightly larger.

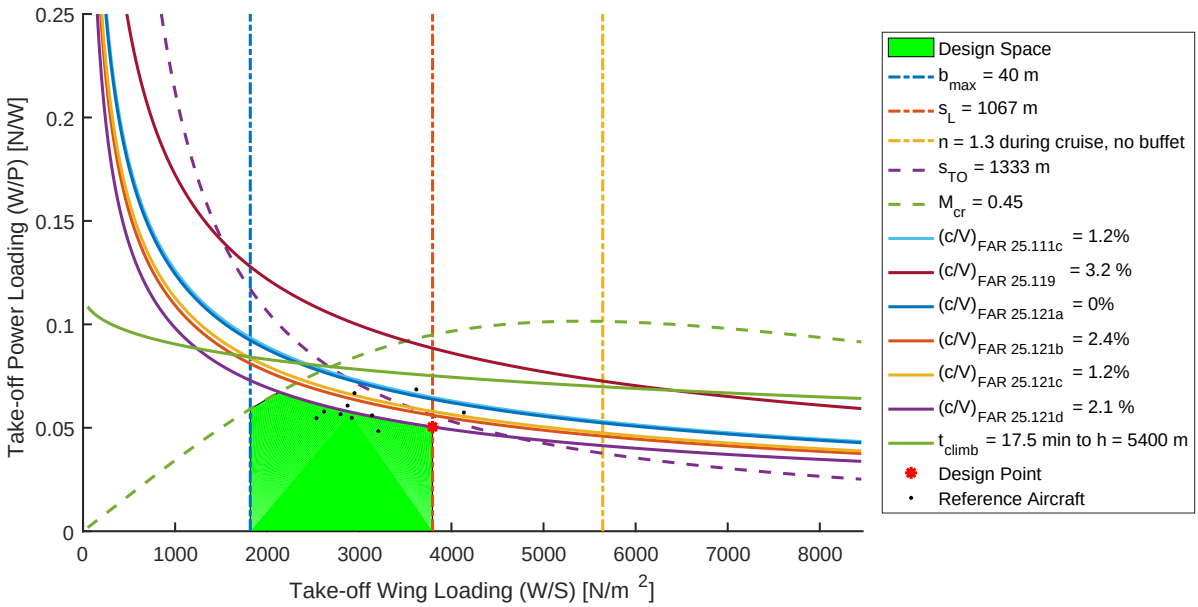

Figure 6.7: Design point for the ATR72-600 in the wing-power loading diagram

Because the propulsive efficiencies of the DFS are defined in a settings file, it means that the DFS geometry will not influence η_{prop}. However, for the mass estimations and stability estimations it is required to have a detailed model of the fan and duct airfoil. The fan geometries of the DUUC are based on the DFS studied by Grunwald et al. [9], because this fan geometry is documented in great detail which facilitated the implementation in the Initiator. The number of fan blades is set to 8, and the duct profile a NACA0009 airfoil. The tip clearance is assumed to be 1% of the fan radius. No aerodynamic considerations were taken when the number of fan blades and duct profile were chosen. For future research to the DUUC concept it is highly advised to couple the DFS geometry to the propulsive performance, because the geometries of the fan and the duct will have a significant influence on it.

6.2.3. CLASS 2 WEIGHT ESTIMATION COMPARISON

A major difference in Table 6.3 indicates that the OEM of the DUUC is significantly larger than of the ATR72-600. This is mainly caused due to an increased mass of the propulsion system, see Figure 6.8. An overview of the propulsion component masses given in Table 6.5 shows that the main contributors to the DFPE mass are the engine, duct, and pylon. The gasturbine mass of the DUUC is similar to the one of the ATR72-600. The slightly larger mass is caused by the larger required gasturbine power, which follows from the power loading in Figure 6.7. The duct mass is dominated by the mass of the duct shell, which is large because of its large

volume. The mass of the blade containment liner is about one order of magnitude smaller than the duct shell mass. Because the duct shell mass is determined by the airfoil shape, an airfoil with a larger thickness to chord ratio will increase the duct shell mass significantly. Because both the gasturbine and duct are heavy systems, the pylon also becomes heavy since it needs to carry both the masses of the duct and the gasturbine on its tip.

The contribution of the fan mass to the total DFPE mass is marginal. In the case of the DUUC baseline model, which has 8 fan blades per engine, the mass of each fan blade is about 10kg, which is approximately 0.6% of the mass of half of the DFPE. The mass estimation of the fan seems to be low when it is compared to the reference propellers as presented in Appendix E. Propellers with a similar diameter, with 4 blades, and a lower take-off power are in the order of 150kg-170kg. Furthermore, the six-bladed F568 fan has the same mass as the eight-bladed DFS. Because there exists an uncertainty in the fan mass estimation, a sensitivity analysis is done in Section 6.3.7 where the mass of the entire DFPE is varied to study the impact on the overall aircraft design.

As stated in the introduction of this report, the idea of integrating the propulsion system with a stabilizing ring-wing lifting surface and jet control vanes, is that possibly a lighter and more fuel efficient design results, which furthermore adds blade-containment and noise shielding. Table 6.6 shows a weight comparison of the propulsion and empennage system, of the ATR72-600 and DUUC. The table shows that the fraction of the DFPE of its OEM is about 5% more than in the case of the ATR72-600. Given the fact that the empennage mass of the ATR72-600 model are likely underestimated, it is uncertain if the comparison is valid.

However, comparing the propulsion and empennage data of the ATR42 as given in Appendix G [73], which has more or less the same empennage size as the actual ATR72-600, it is concluded that the fraction of the combined propulsion and empennage system is in the same order as the ATR72-600 model in this research, see Table 6.6. Because of this, it is likely that the fraction of the combined propulsive and stabilizing systems of the DUUC are heavier, than for the ATR72-600 and ATR42.

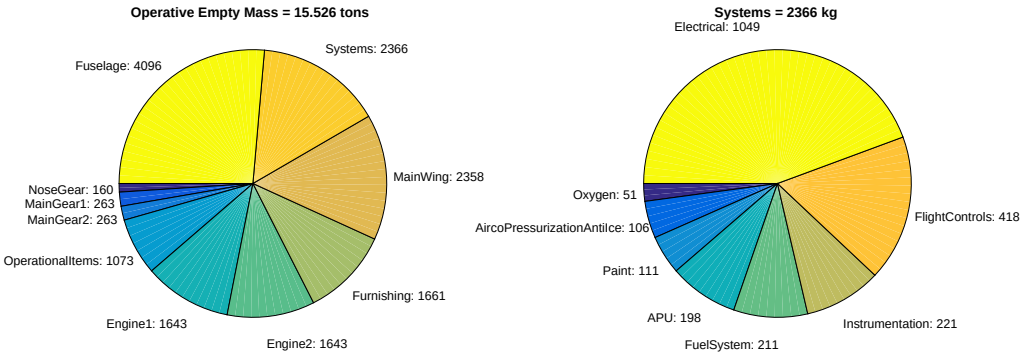

Figure 6.8: Class 2 weight estimation breakdown for the DUUC using Torenbeek and EMWET mass estimation methods. Masses are given in [kg]

Table 6.5: Comparison of propulsion components masses for baseline aircraft, per engine

	ATR72-600		**DUUC**	
Component	Mass [kg]	[%]	Mass [kg]	[%]
Gasturbine	603	64	655	40
Fan	81	9	81	5
Centerbody	181	19	196	12
Systems	81	9	87	5
Pylon	-	-	359	22
Duct	-	-	265	16
(Shell)	-	-	*(245)*	*(14.8)*
(Blade containment liner)	-	-	*(20)*	*(1.2)*
Total	**946**	100	**1643**	100

Table 6.6: Comparison of propulsion and empennage components masses for baseline aircraft, including ATR42 weight results of Obert[73]. OEM: ATR42=10.3tons; ATR72-600=13.2tons; DUUC=15.5tons

	ATR42		ATR72-600		DUUC	
Component	Mass [kg]	OEM-[%]	Mass [kg]	OEM-[%]	Mass [kg]	OEM-[%]
Engine 1	606	5.9	946	7.2	1643	10.6
Engine 2	606	5.9	946	7.2	1643	10.6
Hor. tail	220	2.1	100	0.8	-	-
Vert. tail	322	3.1	134	1.0	-	-
Total	**1754**	**17.1**	**2126**	**16.2**	**3286**	**21.2**

6.2.4. DRAG COMPARISON

Figure 6.9 shows the lift-drag polar for the ATR72-600 and DUUC baseline models, in the trimmed condition. It can be seen that for $C_L = 0$, the DUUC has a lower drag than the ATR72-600, which follows from the lower parasite drag coefficient (C_{D_0}), see Table 6.7. Due to the absence of the horizontal and vertical stabilizer, a significant reduction in C_{D_0} is experienced. To account for the presence of the main landing gear fairing for the ATR72-600, the parasite drag of the fuselage is increased with 3%, based on Torenbeek's assumption for canopies and landing gear fairings [40].

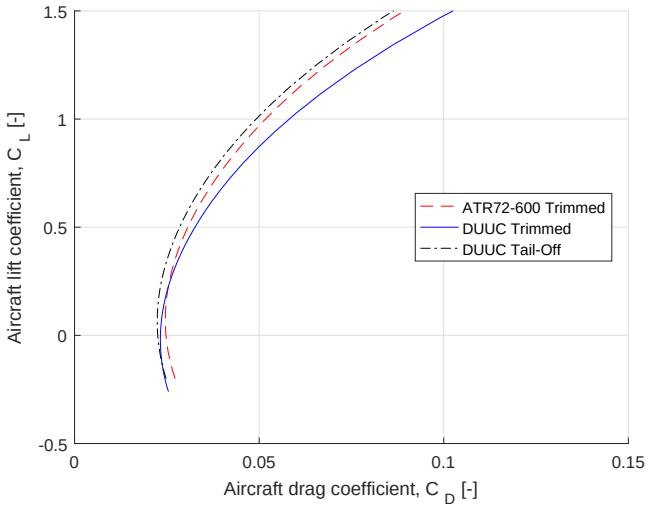

Figure 6.9: Aircraft lift-drag polar comparison

Table 6.7: Comparison of parasite drag components for baseline aircraft. To clarify, 1 drag count [cts] corresponds to $C_D = 10^{-4}$. Wing surface areas: ATR72-600 = 57.6m^2, DUUC = 64.1m^2.

	ATR72-600			DUUC		
Component	S_{wet} [m^2]	C_{D_0} [cts]	[%]	S_{wet} [m^2]	C_{D_0} [cts]	[%]
Wing	104	77	35	116	77	39
Horizontal Tail	35	12	5	-	-	-
Vertical Tail	23	7	3	-	-	-
Fuselage	213	75	34.4	220	69	35
Main Gear Fairing	-	2	0.6	-	-	-
Engine 1	20	23	10	42	26	13
(Duct)	-	-	-	*(38.5)*	*(24.6)*	*(12.3)*
(Pylon)	-	-	-	*(3.5)*	*(1.4)*	*(0.7)*
Engine 2	20	23	10	42	26	13
(Duct)	-	-	-	*(38.5)*	*(24.6)*	*(12.3)*
(Pylon)	-	-	-	*(3.5)*	*(1.4)*	*(0.7)*
Total	**415**	**217**	100	**420**	**199**	100

A remarkable result in Table 6.7 is that both aircraft have approximately the same wetted area(S_{wet}), while the DUUC has a 8% lower parasite drag coefficient than the ATR72-600. This difference has various causes. First of all, all drag coefficients listed in Table 6.7 are normalized with the wing surface area. Because the DUUC has a larger wing surface area, objects with the same geometry for both aircraft will give a lower parasite drag coefficient for the DUUC. Once these drag coefficients are multiplied with the dynamic pressure and reference wing surface area, both result the same drag force.

For example, both aircraft have the same $C_{D_{0_{\text{wing}}}}$, while the DUUC has a larger wetted surface area. Because both wings have the same aspect ratio and taper ratio, and due the normalization with S_{W}, both wings result the same C_{D_0}.

Another interesting example is that the DUUC has a smaller, $C_{D_{0_{\text{fuselage}}}}$ while both aircraft have similar lengths of 27.5m and diameter of 2.8m. The fuselage parasite drag is calculated with the same empirical equation, as used for the nacelle and pylon as described in Section 2.3.4:

$$C_{D_0} = (C_{\text{f}})\left(f_{\text{L/D}}\right)\left(f_{\text{M}}\right)\left(\frac{S_{\text{wet}}}{S_{\text{W}}}\right) \tag{6.5}$$

The main variables in this equation are the slenderness ratio ($f_{\text{L/D}}$) and the fuselage wetted area normalized with the wing area ($S_{\text{wet}}/S_{\text{W}}$). Because the DUUC has a 11% larger wing surface area, the parasite drag of the fuselage is about 11% lower than the ATR72-600, resulting in C_{D_0} = 69cts compared to C_{D_0} = 77cts.

The table shows that the engines of the DUUC have a larger drag than the ATR72-600, which follows from the fact that the ducted fans have an almost twice as large wetted area compared to the turboprop engine. The combination of the increased $S_{\text{wet}_{\text{engine}}}$ and S_{W} of the DUUC, result that the relative increase in $C_{D_{0_{\text{engine}}}}$ is not linearly proportional to the engine wetted area only.

As explained in Section 2.3.4 an empirical relation for nacelles is used to calculate the duct drag, and an empirical relation for planar wings is used to calculate the pylon drag. Based on the wetted areas of the pylon and duct, the respective C_{D_0} values are calculated. Furthermore, it is assumed that the drag effects of the jet vanes, centerbody, and fan are included in propulsive efficiency. However, one could say that the ducted fan is exactly the same as a turboprop with an additional nacelle, and therefore by adding $C_{D_{0_{\text{duct}}}}$ to $C_{D_{0_{\text{turboprop}}}}$ the total drag of the DFS should be acquired. After a close investigation of turboprop parasite drag calculation it is found that the Initiator uses the same empirical parasite drag estimation as given by Equation (6.5) for all turboprop engines, however hard-coded values are used for the wetted area and form factor: $S_{\text{wet}_{\text{turboprop}}} = 20\text{m}^2$ and $f_{\text{M}} = 1.5$. And so the $C_{D_{0_{\text{turboprop}}}}$ only scales with the slenderness ratio ($f_{\text{L/D}}$) of the turboprop engine, but not with the wetted are of the fan. Because of the hard-coded values, it is uncertain how valid the turboprop parasite drag calculation is.

Furthermore, the nacelle parasite drag calculation only looks at the wetted area on the outside of the nacelle, and not at the wetted area on the inside of the nacelle. Both for ducted-fan and turbofan engines only the nacelle parasite drag estimation is used, and not an additional fan related drag. Therefore, it is first of all concluded that it is certain that the $C_{D_{0_{\text{duct}}}}$ is calculated correctly, because it is similar to the turbofan parasite drag calculation. Secondly, it is uncertain how valid the turboprop parasite drag calculation is, based on the hard-coded values.

Although the validity of the parasite drag estimation for the turboprop and ducted-fan engines is uncertain, the induced drag calculation is more realistic. The trim drag of the ATR72-600 is calculated with the AVL-module in the Initiator, and for the DUUC the trim diagram moment balances are used. Figure 6.9 shows that especially for higher lift coefficients the DUUC has a larger drag coefficient than the ATR72-600, which originates from the large trim drag. Both aircraft have $C_{L_{\text{max}_{\text{cruise}}}} = 1.3$, where the ATR72-600 has $C_{D_{\text{max}_{\text{cruise, trimmed}}}} = 0.0721$, and the DUUC has $C_{D_{\text{max}_{\text{cruise, T-O}}}} = 0.0693$ and $C_{D_{\text{max}_{\text{cruise, trimmed}}}} = 0.0823$. The figure shows that the DUUC has a 14% higher cruise drag than the ATR72-600, when flying at its maximum cruise lift coefficient. This result clearly shows that the large trim drag due to the aft shifted OEM c.g. due to the heavy DFPE has an enormous impact on the aircraft drag and therefore the fuel burn of the DUUC concept.

When comparing the aerodynamic efficiency of both aircraft in terms of lift-to-drag ratio, the ATR72-600 results in a mean cruise lift-drag ratio of $(L/D)_{\text{cruise,mean}} = 19.7$, and the DUUC has $(L/D)_{\text{cruise, mean}} = 20.6$. Because the DUUC has a higher L/D-ratio, one could state that the DUUC is aerodynamically more (yet slightly) efficient. However, because the DUUC has a larger OEM it requires more lift force (in Newtons) to fly the aircraft, which results in a larger drag force. To compensate a larger drag force a larger thrust force is required, which increases the fuel burn.

Table 6.8 shows the lift, drag, and thrust values at the start of the cruise phase. It is seen that the DUUC has a larger lift-drag ratio compared to the ATR72-600. However, because these coefficients are normalized with the wing surface are, and the DUUC has 11% more wing surface are compared to the ATR72-600, the actual drag force and consequently the thrust force are larger compared to the ATR72-600. To conclude, although the (L/D)-ratio can be used to analyze the aerodynamic efficiency of an aircraft, this does not necessarily lead into a more fuel efficient design in terms of fuel burn.

Table 6.8: Start of cruise mission analysis results

Parameter	Unit	ATR72-600	DUUC
C_L	-	0.681	0.664
C_D	-	0.0368	0.0347
L/D	-	18.5	19.1
Lift	kN	218	241
Drag	kN	11.8	12.6
Thrust	kN	11.8	12.6
Fuel burn	g/s	102	129
Altitude	m	7190	719
Mach	-	0.45	0.45

6.2.5. HORIZONTAL STABILITY ESTIMATION

Given the fact that the propeller downwash effects on the horizontal stabilizer are not implemented in the current version of the Initiator, it is not possible to use the HSE-module for conventional turboprop aircraft, to minimize the horizontal tail surface area, and to place the wing position accordingly. Since the propeller slipstream causes an increase in lift at the horizontal stabilizer, the required tail surface area can be less than without including this effect [39]. Therefore this section mainly focuses on the effect of the DFPE on the DUUC design itself.

CENTER OF GRAVITY SHIFT

The c.g. shift plots in Figure 6.10 clearly show the effect of the heavy DFPE. For instance, the OEM c.g. of the ATR72-600 lies at 0.35MAC, compared to a 0.65MAC of the DUUC. Furthermore, because the OEM c.g. is far aft, and the fully loaded aircraft shifts the c.g. more front, a large maximum operational c.g. shift is experienced; 0.49MAC compared to 0.33MAC of the ATR72-600. A front shifted c.g. during cruise increases the moment arm of the wing, and therefore the required horizontal stabilizer downforce becomes high ($C_{L_H} = -0.52$ at $C_{L_{\text{tail-off}}} = 1.3$) to maintain balanced horizontal steady cruise flight, see the trim diagram in Figure 6.13.

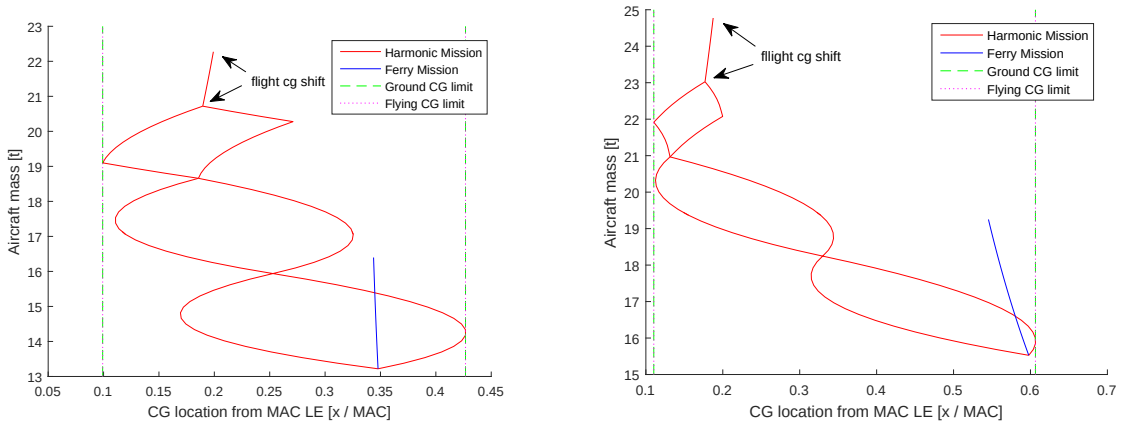

(a) ATR72-600 : $\left.\frac{\Delta x_{cg}}{\bar{c}}\right|_{max} = 0.33$, $\left.\frac{\Delta x_{cg}}{\bar{c}}\right|_{flight} = 0.0095 = 2.2\text{cm}$

(b) DUUC : $\left.\frac{\Delta x_{cg}}{\bar{c}}\right|_{max} = 0.49$, $\left.\frac{\Delta x_{cg}}{\bar{c}}\right|_{flight} = 0.0102 = 2.5\text{cm}$

Figure 6.10: C.g. shift of baseline models. The cruise c.g. shift is only caused by the fuel burn.

One could say that the large operational c.g. shift of the DUUC only poses a problem during the loading of the aircraft on the ground. Once fully loaded the c.g. shift is only 0.0102MAC, compared to 0.0095MAC of the ATR72-600. Although tip-over during ground handling is a severe problem, there are various possibilities to prevent it. A first solution would be to implement proper loading protocols of the passengers, i.e. from front to back in case of the aft shifted OEM c.g. A second solution, could be to implement retractable tail wheel, which is done for example to the Ilyushin IL-62M, see Figure 6.11. By deploying this device during ground handling, it supports the aft part of the fuselage and prevents it from tipping over.

Figure 6.11: Tail wheel on the Ilyushin IL-62M, to prevent tip-over during ground handling [76]

WING-POSITIONING

The wing-positioning plot of the DUUC baseline model is presented in Figure 6.12(a). The plot shows that the wing-position is chosen on the lower bound of the design space, on the intersection of the *"aft cg location"* and *"neutral stability including static margin of 5%"*. The LE of the wing root lies at 50.8% of the fuselage length, measured from the nose. The design space is $\Delta\overline{X}_{\text{LE}_{\text{wing}}} = 0.0134$, which corresponds to 37cm for a fuselage length of $L_{\text{fuselage}} = 27.5$m. This means that the aircraft designer has the freedom to move the wing longitudinally within 37cm, measured 14m from the nose of the aircraft. Of course by placing the wing as much forward as possible, the largest tail arm is resulted which has the lowest tail downforce requirement to keep the aircraft balanced, which consequently produces the lowest trim drag.

An interesting fact is that the line corresponding to *"control at takeoff"* in the wing-positioning plot, see Figure 6.12(b), is remotely located from the other stability and balance lines. Due to the tail downforce generated by the DFPE which uses thrust vectoring, the aircraft can generate a large nose-up moment around the landing gear to rotate the aircraft during take-off. The wing-positioning plot diagram shows that the stall constraint is one of the bounds of the wing-positioning design space. Due to the relatively aft c.g. with respect to the fuselage length, the DUUC tail arm is relatively short; $l_h / L_{\text{fuselage}}$ is 30% compared to 46% of the ATR72-600. Due to the small tail arm, the DFPE needs to generate a larger downforce to maintain balanced during flight.

A possible manner to manipulate the wing-positioning diagram such that a more forward wing position is chosen, is to implement a balance weight which is located in front of the most forward c.g. location. An example of such an implementation is a trim tank filled with water. The trim tank should ideally be installed near the cockpit, to ensure that it has a maximum offset with respect to the c.g. without trim tank. Due to this large offset, a lower trim tank mass is required to shift the c.g. more up front. In Figure 6.12(a) this would yield that the *"forward c.g."* and *"aft c.g."* lines shift more to the left, as such a lower $\overline{X}_{\text{LE}_{\text{wing}}}$ is selected when the *"aft c.g."* line intersects the *"neutral stability including static margin of 5%"* line.

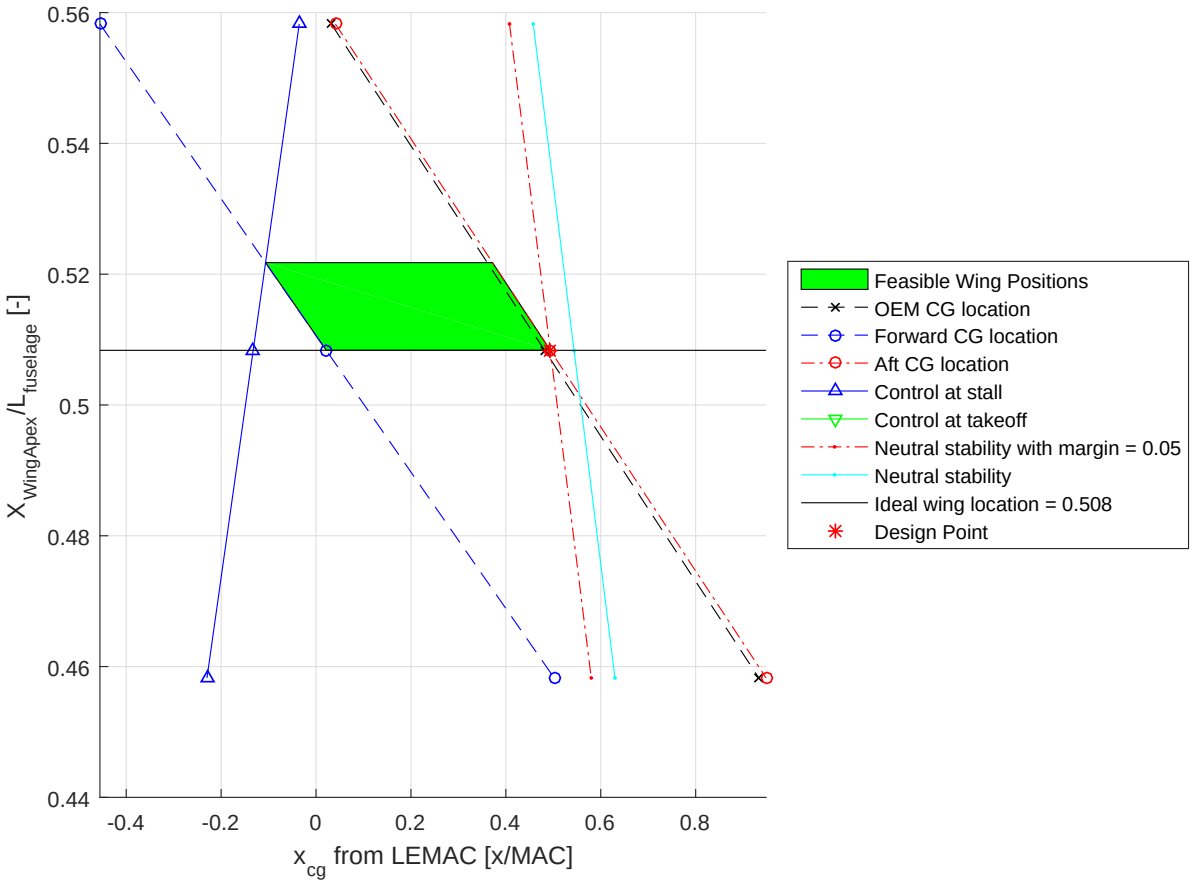

(a) DUUC baseline wing-positioning plot. $\Delta\overline{X}_{\mathrm{LE}_{\mathrm{wing}}} = 0.0134$

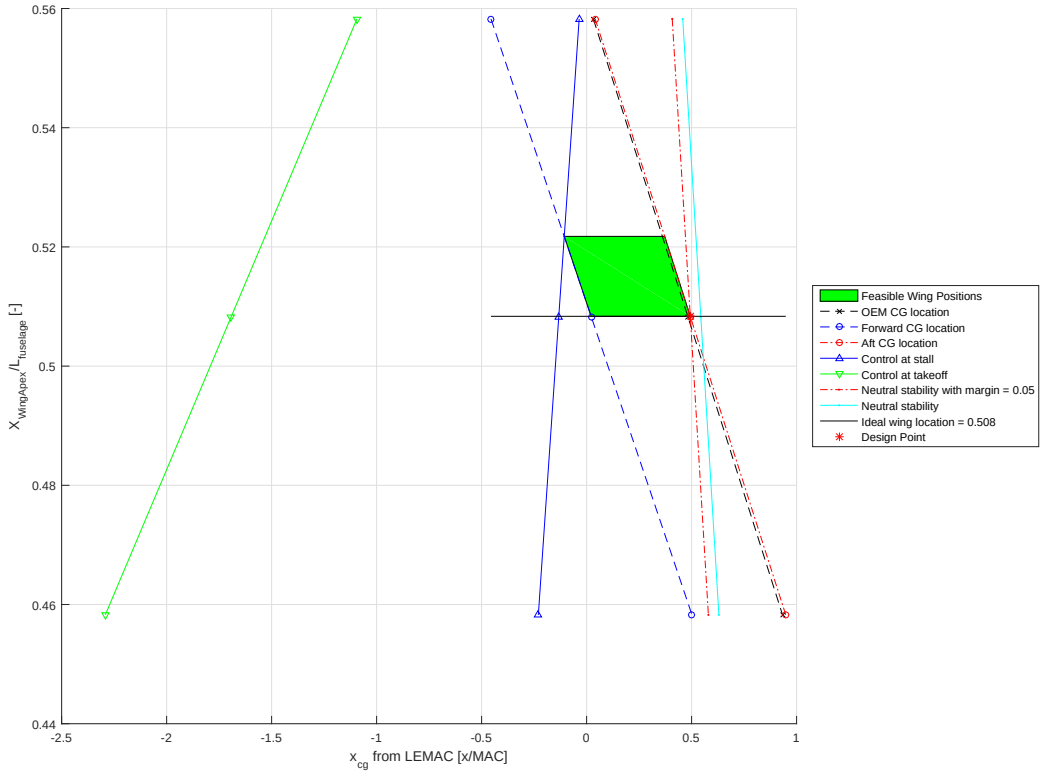

(b) DUUC baseline wing-positioning plot, including "control at takeoff" line. For the other wing-position plots the "control at takeoff" is left outside the figure's horizontal domain, since it is not close to being an active constraint for the wing-positioning design space.

Figure 6.12: DUUC baseline wing-positioning plot

TRIMMING

In Section 5.6.2 it is assumed that the trim drag calculation method is valid for small absolute c.g. during flight, in the order of 1%MAC, and that the forward c.g. bound during cruise flight in the trim diagram is taken. The loading diagram of the DUUC in Figure 6.10(b) firstly shows that the c.g. during flight lies forward on the MAC, so therefore the trim diagram bound corresponding to forward c.g. in cruise can be taken. Secondly, the figure shows that the c.g. shift during flight is in the same order of magnitude as stated by the assumption. A c.g. shift of 2.5cm is insignificant compared to the total aircraft length of 27.5m, and therefore the trim drag calculation method described in Section 5.6.2 is valid for the current design of the DUUC. However, by modifying the wing sweep significantly or by adding more mass to the front of the aircraft it is likely that the c.g. shift becomes more than 1% MAC, which means that the trim drag calculation method needs to be reviewed on its validity.

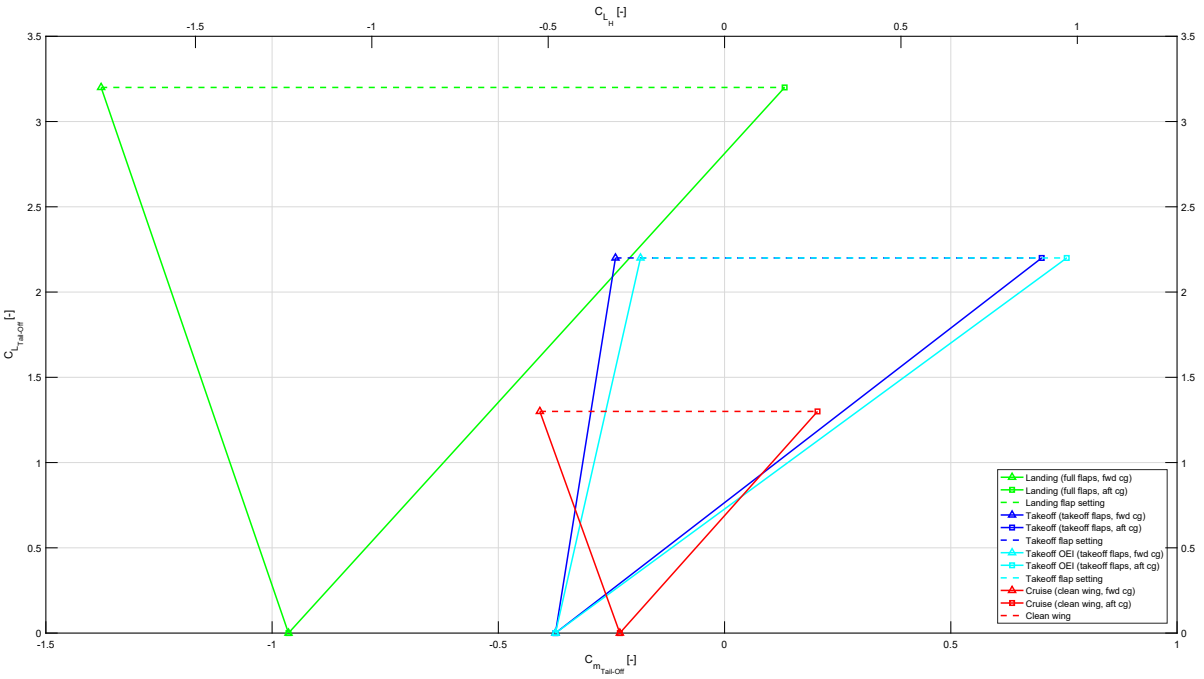

Figure 6.13: DUUC Trim Diagram

The trim diagram of the DUUC is given in Figure 6.13. Because the HSE-module of the Initiator does not work for conventional turboprop aircraft, it is not possible to generate a similar diagram for the ATR72-600. The diagram consists mainly three important triangles: cruise (clean), landing (full flaps), and take-off (incl. flaps). In addition, a one-engine-out case is included, to demonstrate its effect on the tail downforce. Because the thrust setting affects the lift generation of the DFPE, see Section 2.3.3, the OEI-case will affect the results in the trim diagram for the DUUC.

In general the tail diagram looks as expected, given the example diagram in Figure 5.7. In the cruise condition the aircraft generates the lowest lift since there is no flap deflection ($C_{L_{\text{T-O}}} = 1.3$). During take-off the flaps are deflected to gain extra lift ($C_{L_{\text{T-O}}} = 2.2$), which also give a higher nose-down pitching moment, i.e. $C_{m_{\text{T-O}}}$ becomes more negative. Because the difference between the take-off and landing cases is the maximum flap setting, the landing case gives the highest lift force ($C_{L_{\text{T-O}}} = 3.2$) and the highest nose-down pitching moment, i.e. lowest value of $C_{m_{\text{T-O}}}$.

The reason why the trim drag triangle corresponding to the take-off condition looks different compared to the cruise and landing trim drag triangles, is that for the take-off rotation the moment balance is taken with respect to the landing gear, and not with respect to the center of gravity. Because the landing gear is more aft on the MAC than the most forward c.g. location, it reduces the wing moment arm and therefore the tail-less pitching moment, which has as consequence that the tail should generate a lower downforce.

Because the cruise flight triangle in the trim diagram is the most important for the trim drag calculation, a closer look is taken to this particular item. The diagram shows that for the forward c.g. location, an increasing wing lift generates a larger nose-down pitching moment. In this case, the point where the resultant lift force of

the tailless aircraft (i.e. the neutral point) is located at $x_{np} = 0.13\overline{c}$ and the most forward c.g. lies at $x_{cg} = 0.02\overline{c}$. Because the neutral point is behind the most forward c.g. location, a larger nose-down pitching moment is generated with increasing wing lift. To compensate this larger nose-down pitching moment, the DFPE requires to generate a larger nose-up pitching moment, and therefore it generates more negative lift (i.e. more downforce). In case of the most aft c.g. condition, the DFPE needs to generate a nose-up pitching moment, because the c.g. lies behind the wing at $x_{cg} = 0.49\overline{c}$ which gives a nose-up pitching moment with increasing wing lift.

It might seem peculiar that with increasing aircraft lift coefficient, a larger nose-down pitching moment is resulted. Looking to the wing-positioning diagram in Figure 6.12(a) at the wing position of $X_{WingApex}/L_{fuselage} = 0.508$, it is seen that the most forward c.g. location lies at $\overline{x}_{cg,forward} = 0.02$. Normally it is assumed that the lift force of a planar wing lies around 25% MAC [46], so one could expect that the tailless aircraft creates a pitch up moment with increasing lift coefficient. However, in for the moment balances in the trim diagram the tail-off aerodynamic moment ($C_{m_{T\text{-}O}}$) is calculated with the tail-off lift coefficient ($C_{L_{T\text{-}O}}$), the point of rotation, i.e. the center of gravity ($\overline{x}_{cg}$), and the location of the aerodynamic center of the tailless aircraft ($\overline{x}_{T\text{-}O}$).

From Section 5.4.4 it is recalled that in the Initiator the location of the aerodynamic center of the tailless aircraft is defined by [40]:

$$\overline{x}_{ac} = \left(\frac{x_{ac}}{\overline{c}}\right)_{wing} + \left(\frac{x_{ac}}{\overline{c}}\right)_{fuselage} + \left(\frac{x_{ac}}{\overline{c}}\right)_{nacelles} + \left(\frac{x_{ac}}{\overline{c}}\right)_{thrust} \tag{6.6}$$

Because the nacelles of the DUUC are part of the horizontal stabilizer, it is calculated that $\overline{x}_{ac_{nacelles}} = 0$. The wing aerodynamic center lies at $\overline{x}_{ac_{wing}} = 0.24$, which complies with the expectation.

The shift in aircraft aerodynamic center caused by the fuselage sections forward and aft of the wing, is defined by Torenbeek [40]:

$$\left(\frac{x_{ac}}{\overline{c}}\right)_{fuselage} = \frac{-1.8}{(C_{L_\alpha})_{T\text{-}O}} \frac{b_f h_f l_{fn}}{S_W \overline{c}} \tag{6.7}$$

The fuselage correction depends on the tail off lift gradient $(C_{L_\alpha})_{T\text{-}O}$, fuselage width ($b_f$), fuselage height ($h_f$), and the distance between the wing fuselage root and the fuselage nose (L_{fn}). This equation yields for the DUUC baseline $\overline{x}_{ac_{fuselage}} = -0.25$. Mainly the shape of the nose contributes to this shift [40].

The contribution of the thrust depends on the location of the nacelle, the number of blades (N_{bl}), fan diameter (D_{fan}), longitudinal distance between the quarter chord point of the MAC and the fan ($x_{0.25\overline{c}} - x_{fan}$). The following equation is valid for one engine, therefore result should be multiplied with the number of engines [40]:

$$\left(\frac{x_{ac}}{\overline{c}}\right)_{thrust} = \left(\frac{x_{ac}}{\overline{c}}\right)_{nacelles} - 0.05 N_{bl} D_{fan}^2 \frac{x_{0.25\overline{c}} - x_{fan}}{S_W \overline{c} (C_{L_\alpha})_{T\text{-}O}} \tag{6.8}$$

The thrust contribution for all engines combined yields $\overline{x}_{ac_{thrust}} = 0.14$.

Filling in the numbers in Equation (5.13) yields: $x_{ac} = 0.24 - 0.25 + 0 + 0.14 = 0.13$, which is after the most forward c.g. location of $x_{cg} = 0.02\overline{c}$. This calculation shows that the thrust contribution significantly shifts x_{ac} aft, such that the neutral point lies aft of the most forward c.g. Therefore, an increase in $C_{L_{T\text{-}O}}$ acting upon x_{ac} gives a nose-down pitching moment around the most forward c.g. location during flight.

When investigating the zero lift aircraft pitching moments in Figure 6.13, it seems that the absolute values are quite high. For instance, the cruise zero lift tail-off pitching moment has a value of $C_{m_{T\text{-}O}} = -0.231$. At zero lift of the tailless aircraft ($C_{L_{T\text{-}O}} = 0$), the tail-off pitching moment equals the moment around the aerodynamic center of the aircraft $C_{m_{ac}}$, see Equation (5.9). In the Initiator, $C_{m_{ac}}$ is defined by the contributions of the wing, fuselage, and nacelles:

$$C_{m_{ac}} = C_{m_{ac_{wing}}} + C_{m_{ac_{fuselage}}} + C_{m_{ac_{nacelles}}} \tag{6.9}$$

Based on Torenbeek's empirical relation of high-placed nacelles, it is concluded that $C_{m_{ac_{nacelles}}} = 0.020$, see Section 2.3.2. For the DUUC baseline model the wing generates $C_{m_{ac_{wing}}} = -0.026$. This means that the contribution of the fuselage to the aerodynamic moment is $C_{m_{ac_{fuselage}}} = -0.225$. The fuselage contribution is based on a combination of a DATCOM method, corrected with Torenbeek correction factors. To acquire a more accurate estimate for this parameter, it is advised to use a higher order model within the Initiator. If $C_{m_{tail\text{-}off}}$ becomes lower, the required tail downforce would also decrease, which reduces the trim drag and therefore the fuel consumption. DUUC thesis.

AERODYNAMIC PERFORMANCE OF THE DFPE

All results of the HSE-module for the DUUC rely on the aerodynamic properties of the DFPE. However, these properties vary per flight phase, thus some bookkeeping is required for the HSE-module. The first aspect which affects the aerodynamic performance of the DFPE besides its geometry, is the flight condition. For the HSE-module three critical cases are investigated: longitudinal static stability during cruise, trimming the aircraft up to stall in the landing flight, and balancing the aircraft for the take-off rotation. For the stability case the lift gradient of the DFPE is relevant, and for the balancing cases the maximum lift coefficient is important. Table 6.9 gives an overview of the DFPE lift gradient and lift force for these various conditions.

The table shows that the thrust coefficient (T_c) in take-off is maximum, zero in the stall condition, and non-zero in the cruise flight. For the stall condition the engines are in idle mode, and for the other cases the thrust coefficient is based on the airspeed and thrust force, available power, and propulsive efficiency, see Equations (2.23). Because the thrust coefficient affects the lift gradient of the DFS, see Equation (2.24), the total lift gradient of the DFPE is different in each flight condition.

Recall that in Section 2.3.3 it is stated that the interaction between the pylon and the DFS is unknown, and therefore it is unknown how the pylon would contribute to $C_{L_{\text{DFPE}}}$. Because of this reason, the values given in the table assume that $C_{L_{\max_{\text{DFPE}}}} \approx C_{L_{\max_{\text{DFS}}}}$.

Table 6.9: Characteristics of the DFPE of the DUUC baseline model. Values are given for half of the DFPE. Total horizontal projected surface area, $S_{H_{proj,tot}} = 16.2m^2$. For half of the DFPE: $S_{H_{DFS}} = 6.3m^2$, $S_{H_{Pylon}} = 1.8m^2$. The negative lift coefficients indicate downforces. Lift coefficients given are the maximum achievable given the certain flight condition

		Flight Conditions		
Parameter	**Unit**	**Cruise**	**Take-Off**	**Stall at landing**
T_c	-	0.43	2.88	0.00
$C_{L_{\alpha_{\text{rw}}}}$	1/rad	4.83	4.83	4.83
$C_{L_{\alpha_{\text{DFS}}}}$	1/rad	5.24	7.61	4.83
$C_{L_{\alpha_{\text{Pylon}}}}$	1/rad	3.05	3.05	3.05
$\mathbf{C_{L_{\alpha_{DFPE}}}}$	1/rad	**4.75**	**6.59**	**4.43**
$C_{L_{\text{rw}}}$	-	-2.0	-2.0	-2.0
$C_{L_{\text{DFS}_{\text{clean}}}}$	-	-2.0	-5.0	-2.0
$C_{L_{\text{DFS}_{\text{tv}}}}$	-	-2.4	-6.0	-2.4
$C_{L_{\text{Pylon}}}$	-	-0.4	-0.4	-0.4
$\mathbf{C_{L_{DFPE}}}$	-	**-2.4**	**-6.0**	**-2.4**

6.3. SENSITIVITY ANALYSIS

This section focuses on the DUUC design changes for various parameters which are presented in this report. For instance, in Chapter 2 a set of assumptions is made for the propeller, such as maximum tip Mach number and the propulsive efficiency at take-off for ducted fans. Another set of assumptions is made in Chapter 4, to account for safety factors and uncertainties in the propulsion weight estimation. Each one of these assumptions affects the final DUUC design, and therefore this chapter investigates the impact of the assumptions.

Besides the assumptions which are made to complete the numerical model, the DFPE design of the DUUC baseline model in Section 6.2 is sized based on choices for the ducted-fan main design parameters; $AR_{\text{duct}} = 2.0$ and RPM = 1500. These values are chosen because the design first of all converged, but also because it looked esthetically right. Although the DUUC baseline model is a feasible design, it is by definition not the optimum design.

The purpose of this section is to show the multiple variations in the DUUC design, and to compare its KPIs with respect to the Initiator DUUC baseline model, and the Initiator ATR72-600 model.

6.3.1. DUCT ASPECT RATIO

The duct aspect ratio is probably the most critical design parameter of the DFS. On the one hand, given a certain fan diameter, the AR_{duct} determines the chord length of the duct and therefore the geometry of the DFS, which is directly coupled to the mass and c.g. estimation of the DFPE. Furthermore, AR_{duct} determines the lift gradient of the DFS, which affects the stability equations in the wing-positioning plot. To summarize, the AR_{duct} will have a major impact on the total DUUC design, so it is wise to investigate this parameter in more detail. The results of the analysis are given in Table 6.10.

Table 6.10: Effect of fan duct aspect ratio on the DUUC converged design, comparison with Initiator ATR72-600 model

Parameter	Unit	ATR72-600	DUUC Models				
		Initiator	$AR = 1.5$ *exceeds fuselage*	$AR = 2.0$ *Baseline*	$AR = 2.5$	$AR = 3.0$	$AR = 3.5$ *Instable*
MTOM	kg	22300	+13.5%	+11.2%	+9.9%	+9.4%	+8.5%
OEM	kg	13200	+21.2%	+17.4%	+15.9%	+15.2%	+13.6%
Harmonic fuel	kg	1550	+18.1%	+12.9%	+10.3%	+8.4%	+7.7%
Harmonic fuel fraction	-	0.0695	+4.2%	+1.5%	+0.1%	-0.5%	-0.8%

By increasing AR_{duct}, the duct chord decreases for a fixed fan diameter. By doing so, the duct mass decreases, which leads to a lighter DFPE, and reduced OEM. Reducing the OEM results in a lower fuel burn and therefore reduced MTOM. Table 6.10 proves that the DUUC design can be further improved by increasing the duct aspect ratio. Unfortunately the aspect ratio cannot be increased unlimitedly, because it also decreases the wing-position design space, see Figure 6.14.

Decreasing the duct aspect ratio has a negative impact on the OEM, fuel mass and MTOM, because the ducts become longer and heavier. Furthermore, if the engine location is not updated, the duct length can go beyond the fuselage length, which results that during the take-off rotation the duct would scrape the runway.

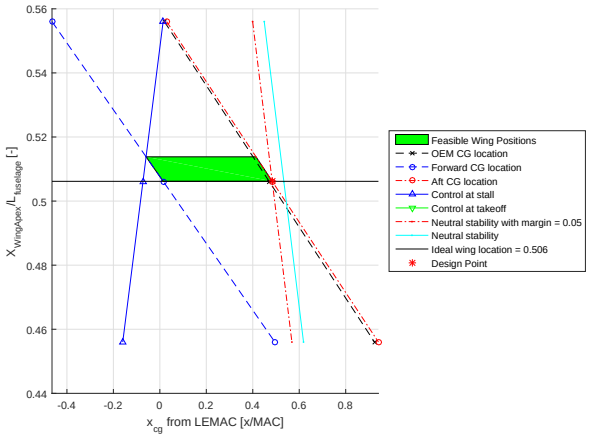

(a) DUUC with $AR_{\text{duct}} = 2.5$. Active stability constraint

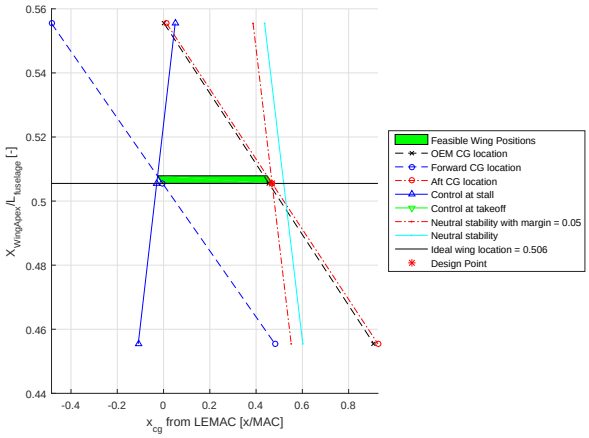

(b) DUUC with $AR_{\text{duct}} = 3.0$. Active stability constraint

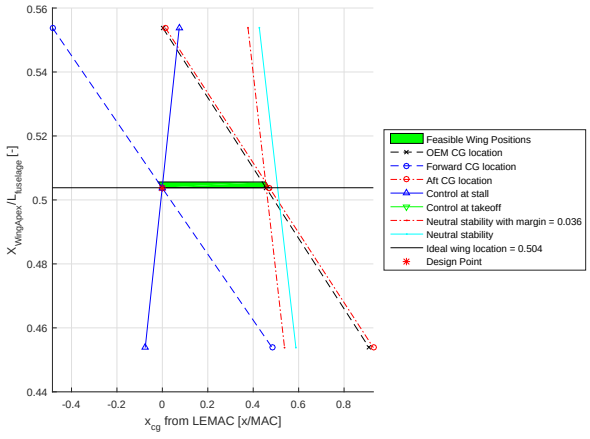

(c) DUUC with $AR_{\text{duct}} = 3.5$. Active stall constraint

Figure 6.14: Variation of the wing-position design space with duct aspect ratio, including active constraints which result in the most forward wing location

For an increasing AR_{duct}, the LSSC-bounds in the wing-positioning diagrams are shifting in such a manner that the upper bound shifts more down. For $AR_{duct} = 3.0$ the constraint which determines the lower bound of the design space is still the *"neutral stability inc. S.M."* line, which means that the aircraft is still neutrally stable including a static margin of 5%. However for $AR_{duct} = 3.5$ the lower bound of the design space is constraint by the *"control at stall"* line, and if the aircraft designer then chooses to use the most forward wing position, the aircraft is no longer neutrally stable, hence an active stabilization such as fly-by-wire is required to maintain stable flight.

6.3.2. FAN TIP MACH NUMBER

In Section 2.1.1 the assumption is made that the maximum fan tip number should be below $M_{tip} = 1$. Based on a reference aircraft, it is decided that for the DUUC baseline model the fans are sized with $M_{tip} = 0.99$. However, the HS F568 propeller on the ATR72-600 has $M_{tip} = 0.916$. Since lowering M_{tip} yields a smaller D_{fan} and thus lighter DFS design, it is investigated how this parameter affects the total aircraft design. The results in Table 6.11 show the results of the sensitivity analysis for $M_{tip} = 0.99, 0.95, 0.90$.

Table 6.11: Effect of fan tip Mach number on the DUUC converged design, comparison with Initiator ATR72-600 model

Parameter	**Unit**	**ATR72-600**	**DUUC Models**		
			$M_{tip} = 0.99$	$M_{tip} = 0.95$	$M_{tip} = 0.90$
		Initiator	*Baseline*		*Instable*
MTOM	kg	22300	+11.2%	+10.3%	+9.4%
OEM	kg	13200	+17.4%	+16.7%	+15.2%
Harmonic fuel	kg	1550	+12.9%	+11.6%	+10.3%
Harmonic fuel fraction	-	0.0695	+1.5%	+1.3%	+0.8%
D_{fan}	m	3.91	3.48	3.30	3.09

The results presented in the table show that lowering M_{tip} has favorable effects on the DUUC design. A reduction of ≈1% in MTOM, OEM, and fuel mass can be expected with lowering the M_{tip} with 5% compared to the DUUC baseline model. The unfortunate consequence of making the DFS smaller and lighter, and without modifying the engine location, is that $S_{H_{proj}}$ also decreases. Because the DFPE generates less downforce with decreasing horizontal project surface area, the design space in the wing-positioning plot also decreases. With $M_{tip} = 0.90$ the wing-positioning plot chooses the "stall-control" constraint for the design point, which means that the stability constraint cannot be satisfied, and therefore the aircraft is neutrally instable.

6.3.3. FAN RPM

Another method to change the duct diameter, is to modify the fan RPM. As stated in Equation (2.2), the fan diameter is directly sized based on an input RPM, for given free-stream and fan tip Mach numbers. Similar to the previous analysis, by modifying D_{fan} the a smaller and lighter DFPE design is resulted. The results are presented in Table 6.12.

Table 6.12: Effect of fan revolutions per minute on the DUUC converged design, comparison with Initiator ATR72-600 model

Parameter	**Unit**	**ATR72-600**	**DUUC Models**			
			RPM = 1400	RPM = 1500	RPM = 1600	RPM = 1700
		Initiator		*Baseline*		*Instable*
MTOM	kg	22300	+12.1%	+11.2%	+10.3%	+9.4%
OEM	kg	13200	+19.7%	+17.4%	+15.9%	+15.2%
Harmonic fuel	kg	1550	+14.2%	+12.9%	+11.6%	+10.3%
Harmonic fuel fraction	-	0.0695	+2.0%	+1.5%	+1.1%	+0.7%
D_{fan}	m	3.91	3.73	3.48	3.26	3.07

In fact, the results in Table 6.11 are similar to those in Table 6.12. Obviously, modifying the tip Mach number and fan RPM result in the same geometric changes of the fan diameter, and therefore the duct diameter. Therefore the explanation for the phenomena in both tables are the same.

Similar to the analysis on the duct aspect ratio, the RPM cannot be increased too much since it results in instable aircraft design in the wing-positioning plot. The limitations to the wing-positioning design space are depicted in Figure 6.15.

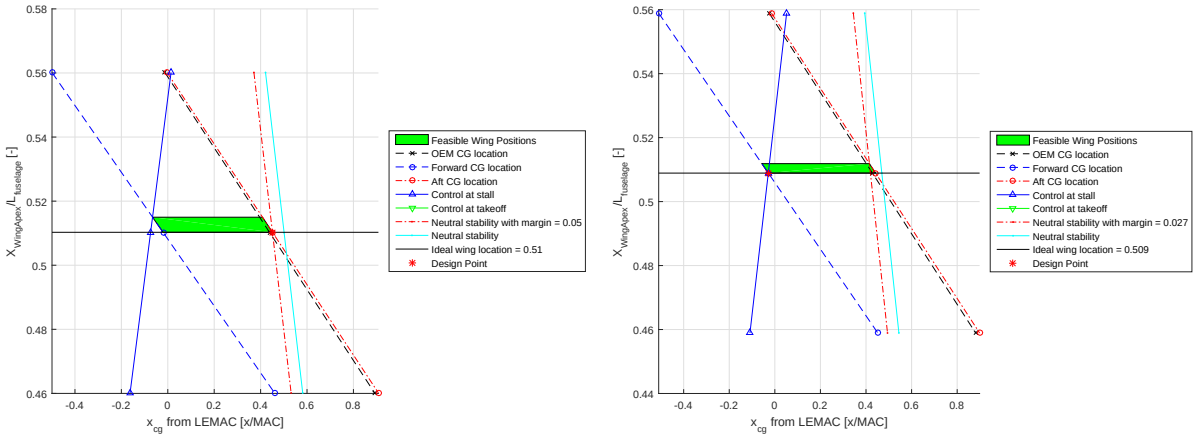

(a) DUUC with $RPM = 1600$. Active stability constraint

(b) DUUC with $RPM = 1700$. Active stall constraint indicates instable aircraft

Figure 6.15: Variation of the wing-position design space with fan RPM (and therefore the duct radius), including active constraints which result in the most forward wing location

Without modifying the engine location, a higher RPM and therefore a smaller DFS design eventually results into an instable aircraft design, because the "control at stall" curve is taken as the active constraint. This phenomena happens for the same reasons as stated in Section 6.3.2.

6.3.4. NUMBER OF FAN BLADES

Because the propulsive efficiency of the DFS is not coupled to the geometry of the DFS, the designs for the duct and fan are chosen arbitrarily. The duct shape is chosen for minimum mass, however the fan geometry and especially the number of fan blades are mainly chosen because of esthetic reasons. Although the fan mass is not the most heavy part of the DFPE, see Table 6.5, it will have a more significant impact on the stability calculations, and therefore the wing-positioning plot, see Equation (5.15). Therefore the effect of the number of blades on the total aircraft design is analyzed in this section. The results of the analysis are presented in Table 6.13.

Table 6.13: Effect of number of fan blades on the DUUC converged design, comparison with Initiator ATR72-600 model

Parameter	**Unit**	**ATR72-600**	**DUUC Models**			
		Initiator	$N_{bl} = 8$ *Baseline*	$N_{bl} = 6$	$N_{bl} = 4$	$N_{bl} = 3$
MTOM	kg	22300	+11.2%	+10.8%	+10.3%	+10.3%
OEM	kg	13200	+17.4%	+17.4%	+16.7%	+16.7%
Harmonic fuel	kg	1550	+12.9%	+12.3%	+12.3%	+12.3%
Harmonic fuel fraction	-	0.0695	+1.5%	+1.5%	+1.6%	+1.7%
$\overline{X}_{LE_{wing}}$	-	0.420	0.508	0.507	0.506	0.505
$\Delta\overline{X}_{LE_{wing}}$	-	-	0.0135	0.0041	0.0144	0.0149

The results of the analysis show that there is a marginal reduction in OEM, MTOM, and fuel mass with decreasing number of fan blades. Mainly the effects on the structural mass are small, because each fan blade weighs approximately 10kg, see Table 6.5. On the other hand, Section 6.2.3 also stated that the mass estimation of the fan is uncertain. The fan mass uncertainty is further analyzed in Section 6.3.7, and the objective of the analysis in this section is to investigate the effect of the number of fan blades on the stability and balance equations.

The table shows that a forward shift in wing position is seen for decreases number of fan blades, which indicates that the tail arm is increased, which reduces the required tail downforce to maintain an balanced

aircraft, which decreases the trim drag. Based on the wing position design space freedom, indicated with $\Delta\overline{X}_{\text{LE}_{\text{wing}}}$, no direct effects are found based on the number of fan blades.

Equation (5.15) shows that by decreasing the number of blades, the contribution of the fan to the location of the aerodynamic center (x_{ac}) decreases. Therefore, reducing the number of blades shifts the tailless aerodynamic center more forward, see Equation (5.13). Because the aerodynamic center lies after the most forward c.g. location during flight ($\overline{x}_{\text{cg,fwd}} = 0.02$), the tailless aircraft generates a nose-down pitching moment. If the aerodynamic center is shifted so far forward, such that $\overline{x}_{\text{ac}} < \overline{x}_{\text{cg}}$, the tailless aircraft would generate a nose-up pitching moment. This has as consequence that the tail should generate a upforce to generate a nose-down pitching moment to maintain a balanced aircraft. From an aerodynamic point of view, this is more efficient compared to generating downforce, since in the first case the DFPE would contribute positively to the total aircraft lift generation.

Based on Equation (5.15), it is concluded that the contribution of each fan blade to $\overline{x}_{\text{ac}_{\text{thrust}}}$ for the DUUC baseline model with 8 fan blades, equals $0.14/8/2 = 0.0088$. Because $\overline{x}_{\text{ac}_{\text{thrust}}} = 0.14$ includes all engines, the contribution per engine equals 0.07. In case of 3 fan blades, the total contribution of all engines to the position of the aerodynamic center of the tailless aircraft becomes $\overline{x}_{\text{ac}_{\text{thrust}}} = 3 \cdot 2 \cdot 0.0088 = 0.0528$.

Reviewing the DUUC baseline calculation for the determination of $\overline{x}_{\text{ac}}$ with Equation (5.13): $\overline{x}_{\text{ac}} = \overline{x}_{\text{ac}_{\text{wing}}} + \overline{x}_{\text{ac}_{\text{fuselage}}} + \overline{x}_{\text{ac}_{\text{nacelles}}} + \overline{x}_{\text{ac}_{\text{thrust}}}$, gives $0.13 = 0.24 - 0.25 + 0 + 0.14$. Implementing $\overline{x}_{\text{ac}_{\text{thrust}}} = 0.0528$ gives $\overline{x}_{\text{ac}} = 0.24 - 0.25 + 0 + 0.0528 = 0.04$. Under the assumption that the c.g. location of the baseline is not affected too much by reducing the number of blades, it is safe to state that even with N_{bl} =3 the tailless aircraft will still generate a nose-down pitching moment ($\overline{x}_{\text{ac}} > \overline{x}_{\text{cg}}$). In reality, by decreasing the number of fan blades the DFPE becomes lighter, which shifts the OEM c.g. even more forward, which increases the distance between the c.g. and a.c. even more.

The sensitivity analysis for the various number of fan blades concludes firstly that there exists a marginal effect on the KPIs, and secondly that the impact on the stability and balance of the aircraft is acceptable.

6.3.5. TAKE-OFF PROPULSIVE EFFICIENCY

In Section 6.2.1 it is assumed that the DUUC propulsive system has similar propulsive efficiencies as the ATR72-600, except for that the DUUC has an improved take-off efficiency. It is assumed that this improvement is 10%, however in reality this could also be more or less. Table 6.14 shows the variation in the DUUC design for $\eta_{\text{prop}_{\text{TO}}} = 0.80, 0.75, 0.70$.

Table 6.14: Effect of propulsive take-off efficiency on the DUUC converged design, comparison with Initiator ATR72-600 model

Parameter	**Unit**	**ATR72-600**	**DUUC Models**		
			$\eta_{\text{TO}} = 0.80$	$\eta_{\text{TO}} = 0.75$	$\eta_{\text{TO}} = 0.70$
		Initiator	*Baseline*		*Same as ATR72-600*
MTOM	kg	22300	24774	24775	24776
OEM	kg	13200	155276	15527	15526
Harmonic fuel	kg	1550	1748	1748	1750
Harmonic fuel fraction	-	0.0695	0.0705	0.0706	0.0706

The table shows that by increasing $\eta_{\text{prop}_{\text{TO}}}$ the fuel consumption decreases, however this is effect is marginal. Because the effects are so small, the absolute values are given in Table 6.14 instead of the relative difference in percentages. Therefore it is concluded that an increase in aircraft efficiency during the take-off phase has little effect on the total design, since the fuel burn is dominated in the cruise phase. In terms of saving fuel, it is more beneficial to increase the efficiency during cruise than during take-off.

Related to this, it is concluded that the increased static thrust advantage of ducted-fans, which is one of the major benefits of the DFS as given in literature, has little effect on the total aircraft design because the fuel burn in the cruise-phase is dominating. Indeed the DFS prove to have a larger propulsive efficiency at the lower velocities, but the benefits gained from that are too small to have a visible benefit on the total aircraft design.

The only advantage which could be derived from the increased static thrust performance of a DFS is that it could reduce the take-off distance, and therefore the DUUC could take-off from smaller runways than the ATR72-600. On the other hand, to increase aircraft sustainability during take-off pilots can choose to have a "reduced thrust take-off". This procedure means that for a given runway length, the pilots choose to take-off

with a lower engine thrust than the maximum take-off thrust. The main benefit is that it reduces the wear on engine components and therefore increasing its lifetime. Additional benefits include reduced fuel burn during take-off and lower noise emissions. The disadvantages of a reduced thrust take-off is that a longer runway is required, and miscalculations in the take-off simulation can cause dangerous situations. [77, 78].

6.3.6. TAKE-OFF DISTANCE

Another fact of the Initiator is that it uses a design take-off distance (s_{TO}) to calculate the design point in the wing-power loading diagram. Both the ATR72-600 and DUUC baseline model use s_{TO} = 1333m, which is based on the take-off distance of the reference ATR72-600.[79] Because the DFS has an increased static thrust and therefore increased propulsive efficiency during take-off, a possible advantage of the DUUC is that it could use a shorter runway to take-off. An additional set of simulations for the DUUC is done with s_{TO} = 1150m, 1000m. With s_{TO} = 1000m the aircraft has the same take-off length as the Cessna Citation-II.[80] For all analysis, the DUUC uses $\eta_{\text{prop}_{TO}} = 0.80$ The results of the analysis are given in Table 6.15.

Table 6.15: Effect of design take-off distance on the DUUC converged design, comparison with Initiator ATR72-600 model. For all analysis, the DUUC uses $\eta_{prop_{TO}} = 0.80$

Parameter	**Unit**	**ATR72-600**	**DUUC Models**		
		Initiator	s_{TO}=1333m *Baseline*	s_{TO}=1150m	s_{TO}=1000m
MTOM	kg	22300	+11.2%	+12.1%	+16.6%
OEM	kg	13200	+17.4%	+18.9%	+24.2%
Harmonic fuel	kg	1550	+12.9%	+16.8%	+31.6%
Harmonic fuel fraction	-	0.0695	+1.5%	+3.9%	+13.1%
Power loading	N/W	0.0497	+1.4%	-2.9%	-16.1%
Wing loading	N/m^2	3790	+0.3%	+0.3%	+0.8%
Engine T-O power	kW	4400	+9.5%	+15.9%	+38.9%
Wing surface area	m^2	57.6	+11.3	+12.3	+15.9%

The results in Table 6.15 show that decreasing the design take-off distance increases the OEM, MTOM, and fuel consumption. The cause of this is a decreased power loading, which follows from the design point in the wing-power loading diagram, see Figure 6.16. For lower take-off distances the power-loading curve corresponding to s_{TO} shifts down and becomes an active constraint, decreasing the design space and thus lowering the power-loading. As explained in Section 6.1.2 a lower power-loading results in more powerful engines. With increasing engine power, the fuel consumption and therefore the fuel mass increase. Additionally, more powerful engines increase the engine mass, which increase the OEM. Both the increases in fuel mass and OEM, increase the MTOM.

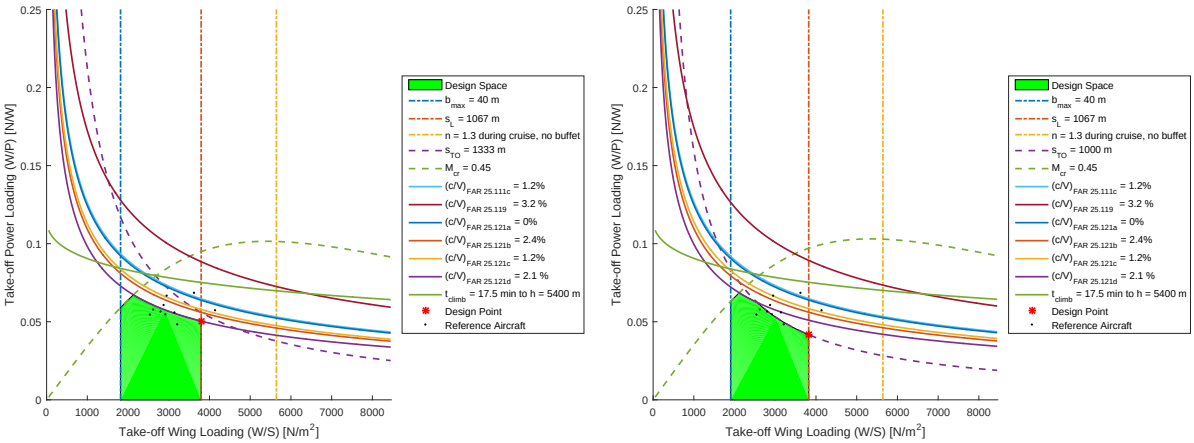

(a) DUUC baseline with s_{TO} = 1333m

(b) DUUC model with s_{TO} = 1000m

Figure 6.16: Difference in wing-power loading diagrams, for various input take-off runway lengths

Unfortunately it was not possible to have a successful design convergence with the ATR72-600 with s_{TO} = 1150m. During the mission analysis simulation it is concluded that the aircraft did not have sufficient thrust available to lift off from the given runway length. Only by increasing the propulsive efficiency to $\eta_{prop_{TO}} = 0.75$ it was possible to have a successful take-off simulation. This analysis proves that the increased static thrust performance of a DFS aids in lifting an aircraft off from a shorter runway.

6.3.7. PROPULSION WEIGHT FACTOR

In the weight estimation method described in Chapter 4 various correction factors are implemented in the DFPE component calculations. Because these correction factors are chosen arbitrarily, it is uncertain how accurate these assumptions are. Additionally, an uncertainty in the results of the fan mass estimation is found in Section 6.2.3. Therefore a sensitivity analysis is done where the masses of all propulsion components are varied. To do so, a propulsion weight factor (PWF) is implemented in the Class 2 Weight Estimation calculations. This factor is used to correct the weight of each component:

$$W_{propulsion} = PWF\left(W_{eng} + W_{cb} + W_{fan} + W_{duct} + W_{pylon}\right) \tag{6.10}$$

The DUUC baseline model is executed with PWF = 1.00, and additional design convergences are done with PWF = 1.75, 1.50. The results are presented in Table 6.16.

Table 6.16: Effect of propulsion weight correction factor the DUUC converged design, comparison with Initiator ATR72-600 model

Parameter	**Unit**	**ATR72-600**	**DUUC Models**				
			PWF = 1.75	PWF = 1.50	PWF = 1.00	PWF = 0.75	PWF = 0.50
		Initiator			*Baseline*		
MTOM	kg	22300	+20.2	+17.0%	+11.2%	+8.5%	+5.8%
OEM	kg	13200	+31.8	+27.3%	+17.4%	+13.6%	+9.1%
Harmonic fuel	kg	1550	+21.9	+19.4%	+12.9%	+11.0%	+8.4%
Harmonic fuel fraction	-	0.0695	+1.6	+1.7%	+1.5%	+2.0%	+2.3%

As expected, with decreasing PWF the OEM decreases, which consequently reduces the fuel mass and MTOM. Although the fuel mass decreases with decreasing PWF, the fuel fraction increases. Because the fuel fraction is defined as the fuel mass divided by the MTOM, an increasing fuel mass indicates a less fuel efficient design. If the fuel fraction becomes infinitely small, it means that it costs hardly any fuel to transport the aircraft. Because the relative decrease in fuel mass in Table 6.16 is less than the relative decrease in OEM, the fuel fraction increases with decreasing PWF.

For an aircraft designer it could be a reason to choose the most efficient aircraft design in terms of fuel fraction, which is in this case the DUUC with PWF = 1.00, even though it seems contradictory. However, an airliner is mainly interested in flying as efficient as possible in terms of kilograms of fuel, because a lower absolute fuel consumption costs them less money. Therefore, if an airliner has to choose the most efficient design, it tends to look at the fuel mass instead of the fuel fraction, since in terms of aircraft fuel economy airliners are more interested in the number of kilograms fuel it costs to transport one passenger over a certain range. [81] And so the term fuel-efficient is rather ambiguous, because an aircraft designer might interpret it different than an airliner. In the end the airliner chooses which aircraft it operates to transport its customers, and therefore it makes more sense to evaluate the fuel-efficiency of the DUUC design in terms of kilograms fuel per passenger per kilometer. And because the number of passengers and the design range of the DUUC is kept constant in this thesis research, automatically a lower fuel mass corresponds to a more efficient design.

Another interesting effect is the location of the wing position, which follows from the wing-positioning diagrams, see Figure 6.17. It is seen that with increasing the PWF, and therefore the DFPE mass decreases, a more forward wing location is selected. If the DFPE mass decreases, the OEM c.g. shifts more forward, which increases the moment arm of the DFPE around the c.g. of the aircraft. With a larger moment arm the DFPE can generate a larger aerodynamic moment based on its maximum achievable lift coefficient, to keep the aircraft balanced during flight.

With increasing tail arm (l_h), the required c.g. location ($\overline{x}_{cg}$) calculated with Equation (5.8) becomes larger. Therefore all stability lines in the wing-positioning plot shift more right. Furthermore, with increasing tail arm, the required c.g. calculated with Equation (5.9) becomes smaller, therefore all controllability lines in the

wing-positioning plot shift more left. These effects combined first of all increase the wing-positioning design space, and secondly they allow to select a more forward wing position.

For a large PWF, the wing-positioning design space becomes infeasible, such that an instable aircraft is resulted, see Figure 6.17(a). This situation shows that for an underestimation of the DFPE mass, it is required to manually modify the design such that a feasible wing-positioning design space results. This can be done by:

- Shift engine more aft
- Shift engine more down
- Increasing $S_{H_{proj}}$ by increasing D_{fan}
- Increasing $S_{H_{proj}}$ by increasing c_{chord} (decreasing AR_{duct})

Because each one of the above mentioned solutions affect the c.g. location, and stability and balance equations, an iterative process should be applied to design a feasible aircraft in case of a significant increase in DFPE mass.

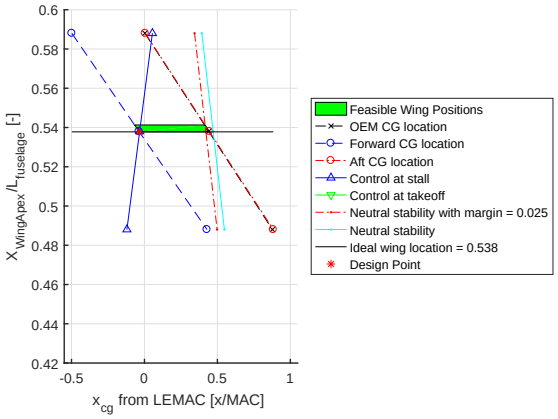

(a) DUUC model with PWF=1.75. Active stall constraint indicates instable aircraft

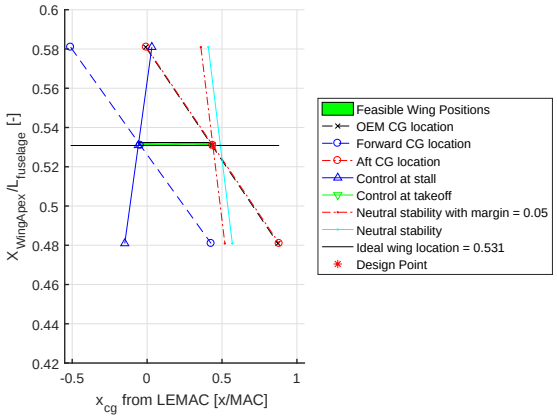

(b) DUUC baseline with PWF=1.50

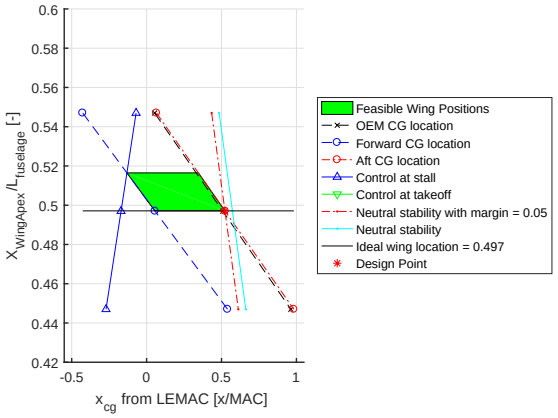

(c) DUUC model with PWF=0.75

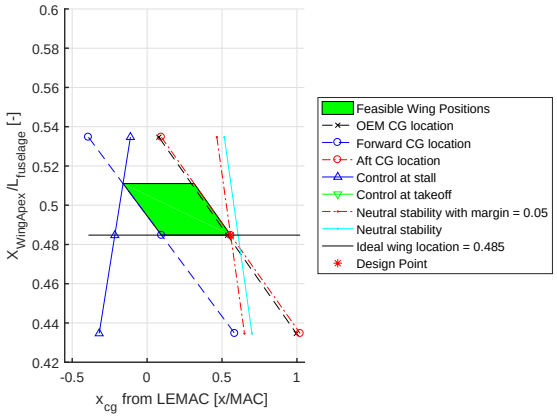

(d) DUUC model with PWF=0.50

Figure 6.17: Difference in wing positioning design space, for various propulsion weight factors

6.3.8. ENGINE LONGITUDINAL LOCATION

Currently the DFS are placed as much aft as possible, to prevent that nacelle scrapes the runway upon take-off rotation. However, placing the DFPE more forward shifts the OEM c.g. more forward, which could increase the tail arm if the wing does not shift, which could reduce the required tail downforce, and thus it could reduce the trim drag. The longitudinal location of the engine is defined by $\overline{X}_{eng} = x_{LE_{engine}} / L_{fuselage}$, which is a setting in the Initiator. This point corresponds to the location of the LE of the engine, in this case the duct, normalized with the fuselage length. The results of the analysis are presented in Table 6.17.

Table 6.17: Effect of fan tip Mach number on the DUUC converged design, comparison with Initiator ATR72-600 model

Parameter	Unit	ATR72-600	DUUC Models		
			$\overline{X}_{eng} = 0.839$	$\overline{X}_{eng} = 0.800$	$\overline{X}_{eng} = 0.739$
		Initiator	*Baseline*		*Instable*
MTOM	kg	22300	+11.2%	+10.8%	+10.8%
OEM	kg	13200	+17.4%	+17.4%	+16.7%
Harmonic fuel	kg	1550	+12.9%	+13.5%	+14.2%
Harmonic fuel fraction	-	0.0695	+1.5%	+2.1%	+3.2%
$\overline{X}_{LE_{wing}}$	-	0.420	0.508	0.504	0.490

The results in the table show that shifting the engines more forward does not directly improve the design. In fact, an increase in fuel mass is seen for $\overline{X}_{eng} = 0.800$. When the DFPE is shifted more forward, a reduction in structural mass is seen, however the fuel consumption increases again. A plausible reason for the reduced OEM is the fuselage weight. In Torenbeek's fuselage weight estimation method, see Section F.2.3, the tail arm is used. For a more forward wing location, the tail arm decreases, which reduces the fuselage mass.

This analysis shows that shifting the DFPE more forward does not give benefits in terms of fuel burn. Even more, shifting the engines more forward reduces the design space in the wing-positioning plot, because with $\overline{X}_{eng} = 0.739$ the aircraft becomes unstable. Therefore it is advised to have the engines as far aft as possible, to maximize the tail arm.

6.3.9. IDEAL AIRCRAFT

The DUUC results are strongly depended on the propulsive efficiencies, and DFPE mass estimation. Although the take-off efficiency proved to have an insignificant effect on the total aircraft design, the cruise efficiency however will have a larger impact. Secondly, the weight estimation of the duct is a new method implemented in the Initiator. Since the duct mass directly influences the pylon mass, and the pylon mass is one of the heaviest propulsion components, the duct has a large influence on the total DFPE mass. Therefore it is decided to perform an "ideal" comparison between the ATR72-600 and DUUC, where an analysis for both aircraft is done with maximum propulsive efficiency during all flight phases of $\eta_{prop} = 1.0$, and a "super-light" duct design of $W_{duct} = 0$kg. The results are presented in Table 6.18.

Table 6.18: Effect of ideal propulsive efficiency $\eta_{prop} = 1.0$ with a super lightweight duct design with $W_{duct} = 0kg$. Comparison with ideal Initiator ATR72-600 model

Parameter	Unit	*Reference* ATR72-600	*Initiator Ideal Aircraft* ATR72-600	Diff *with reference ATR72-600*	DUUC	Diff *with ideal Initiator ATR72-600*
MTOM	kg	22800	21600	-5.3%	22700	+5.1%
OEM	kg	13311	12800	-3.8%	13800	+7.8%
Harmonic fuel	kg	1989	1310	-34.1%	1410	+7.6%
Harmonic fuel fraction	-	0.0872	0.0605	-6.8%	0.0622	+2.9%

The comparison of the ideal aircraft shows that the ATR72-600 with ideal propulsive efficiency has a lower OEM, MTOM, and fuel mass, compared to the reference aircraft. Especially a major gain in fuel mass is expected. The differences of the ideal DUUC are taken with respect to the ideal ATR72-600. The table shows that even though both propulsion systems are ideal, and the duct is weightless, the DUUC has still a 7.8% higher OEM and 7.6% higher fuel consumption. These values show that the assumptions done to the propulsive efficiencies and duct mass estimations are not the cause of the lower KPIs of the DUUC compared to the ATR72-600. Therefore it is concluded that the increased trim drag due to aft shifted c.g. caused by the heavy DFPE is the main disadvantage of the DUUC concept.

6.3.10. SUMMARY ON DESIGN PHENOMENA

This section shortly summarizes the most important design phenomena which were identified during the DUUC sensitivity analysis.

First of all, there is the set of effects which are caused by the heavy DFPE, which is visualized in Figure 6.18. Due to the large pylon tip mass, the pylon mass itself is a large contributor to the total propulsion mass. The large DFPE first of all increases the OEM. In the next weight iteration the increased OEM results in a larger MTOM. For a given power to weight ratio, the engines need to be more powerful to lift off the heavy aircraft. More powerful engines consume more fuel, because they need to generate more thrust to fly the heavy aircraft, which consequently increases the MTOM again. This iterative process is implemented in the aircraft design convergence.

Secondly, the large DFPE mass shifts the OEM c.g. more aft on the MAC. This effects results in smaller tail arm, which requires a larger tail downforce to keep the aircraft balanced during flight. A larger tail downforce increases the trim drag, and therefore the fuel consumption.

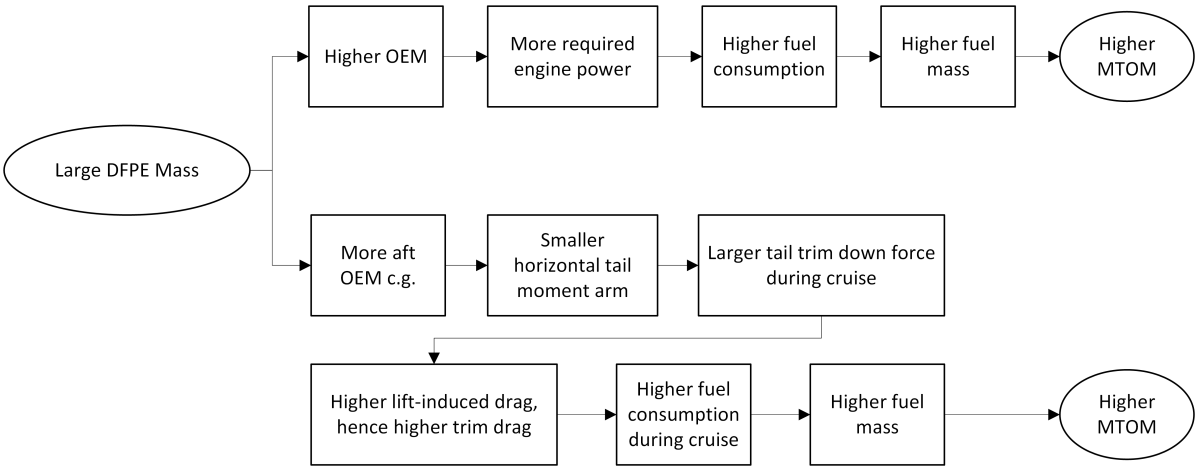

Figure 6.18: Effect of large DFPE mass in the Class 2 Weight Estimation Module

7

CONCLUSION & RECOMMENDATIONS

In this final chapter of the thesis report, an overview of all conclusions about the research to the DUUC conceptual design synthesis is presented. Additionally, a set of recommendations is presented on the current implementation in the Initiator, combined with future research possibilities for the concept.

7.1. CONCLUSION

The objective of this thesis is to find an answer to the main research question:

> **Research Question**
> *"What is the effect of the DUUC concept, an aircraft featuring a ducted fan propulsive empennage, on the key performance indicators of the aircraft design, while providing sufficient longitudinal static stability and balance during flight?"*

The research goals derived from the main research question include: the implementation of turboprop reference aircraft and DUUC concept in the Initiator, aircraft performance comparison, and sensitivity study on the DUUC main design parameters. The conclusions presented in this section are categorized according to these research goals.

7.1.1. IMPLEMENTATION OF TURBOPROP REFERENCE AIRCRAFT IN THE INITIATOR

The first step in the thesis was to model a reference turboprop aircraft in the Initiator from which the DUUC design could be derived. After consideration it was decided to continue with the research on the ATR72-600 development within the Initiator research group. The final model of the ATR72-600 has a -2.2% difference in MTOM, and -0.8% difference in OEM compared to the actual aircraft. Large discrepancies in the fuel consumption up to 22% are found, which are caused by an underestimated power loading and unscalable engine fuel flow look-up table. This causes more powerful and heavier engines, with higher fuel consumption. The power loading underestimation influences both the results of the ATR72-600 and DUUC. Solving this problem would increase the power loading, which results smaller engines and therefore lighter DFPE design for the DUUC. This shifts the OEM c.g. more forward, which increases the tail arm, and therefore decreases the required tail downforce and trim drag, reducing the fuel consumption. Unfortunately, these propeller specific modules are currently being improved by two recently started Initiator theses, and therefore it was not possible to include the updates in the current DUUC design.

An extensive propeller analysis program is developed to calculate the propulsive efficiency of an arbitrary unducted and ducted fan system, and to perform a parametric study to the main ducted fan design parameters. The propeller module is implemented in the Initiator to determine the exact propulsive efficiency during all flight phases. Unfortunately the output of this program is only useful if the input propeller geometry is designed correctly for the free-stream conditions in which the aircraft would operate. Because the propeller design study in the Initiator research group is still under development, this module cannot be activated yet.

In the drag calculation it is found that a hard-coded value is used to determine the parasite drag of the turboprop engine. Because of this, it is difficult to state how accurate the drag parasite drag calculation of the ATR72-600 is.

The empennage of turboprop aircraft is sized only with the tail volume coefficient method, which means that the wing position and tail size are not scaled during each aircraft design iteration based on the longitudinal static stability and balance constraints. Because the empennage is not sized with a higher order analysis method, the horizontal and vertical stabilizer are undersized, which results in a lighter than expected solution. Implementing the horizontal stability estimation module for turboprop aircraft in the current version of the Initiator is advised to solve this problem.

7.1.2. IMPLEMENTATION OF DUUC CONCEPT IN THE INITIATOR

The DUUC is directly derived from the ATR72-600 model. A major update to the core of the Initiator is made to modify the engine geometry, such that it is more modular. By defining an engine (gasturbine), centerbody, fan, duct, and nacelle, virtually all engine architectures can be modeled.

Wing positioning for longitudinal static stability and trimming is the crux of the DUUC design. A modified version of Torenbeek's X-plot method is developed, which is used to position the wing such that the aircraft is neutrally stable, and that it can be balanced during the critical flight conditions, i.e. stall at landing and the take-off rotation. The wing-positioning diagram uses the *"control at stall"* as active constraint, which results in the most forward wing position, and allows the aircraft to be controllable in this critical condition. Manual trial-and-error of varying the main DFS design parameters AR_{duct} and RPM, and the engine location, is required to tune the design to ensure that there is a feasible design space in the wing-positioning plot.

The tail downforce calculated in the trim diagram for the most forward c.g. during cruise, combined with superposition of the lift induced drag of the tailless aircraft and DFPE, result in the total aircraft lift and drag polar. This method is only valid for wings with a small leading edge sweep, and an absolute c.g. shift during flight which is maximum about 1% MAC. This assumption yields that the moment arms of the tail and tailless aircraft do not change throughout the flight. The DUUC total drag is only lower for low aircraft lift coefficients. For higher aircraft lift values the trim drag becomes too large, due to the significant tail downforce required to trim the aircraft. Because the tail-off lift force acts upon the aerodynamic center of the aircraft, which is located after the most forward c.g. location in flight, the tailless aircraft creates a nose-down moment.

The trim diagram shows high values for $C_{m_{\text{tail-off}}}$ caused by a high fuselage nose-down pitching moment, which affect the required $C_{L_{\text{H}}}$ and trim drag during cruise. For future research within the Initiator it is advised to implement a higher-order model to calculate these aerodynamic coefficients more accurately.

7.1.3. PERFORMANCE COMPARISON OF DUUC AND ATR72-600 MODELS

The DUUC baseline model shows to have +17.4% OEM, +12.9% fuel mass, and +11.2% MTOM compared to the ATR72-600 model. One cause of these higher values is the heavy DFPE which is located near the rear of the aircraft. This puts the c.g. far aft with respect to the fuselage length, which results in a decreased tail Therefore the DFPE needs to generate a larger downforce to keep the aircraft balanced during flight, which increases the trim drag and consequently also the fuel burn.

The DUUC has a lower parasite drag coefficient compared to the ATR72-600, which is mainly caused by the fact that the drag force is normalized with the wing surface area, and the DUUC has a larger wing than the ATR72-600. However, undersizing of the ATR72-600 empennage and uncertainties in the turboprop parasite drag estimation could decrease this difference between the two baseline aircraft. For certain, the trim drag disadvantage overrules the reduced parasite drag gain. During cruise flight the DUUC has 14% more drag than the ATR72-600.

7.1.4. DUUC SENSITIVITY ANALYSIS

The analysis of the variable duct diameters, i.e. done via modifying M_{tip} or the fan RPM, showed that smaller and lighter duct designs lower the OEM, MTOM, and fuel mass. Consequently, decreasing the size of the DFS decreases the horizontal projected surface area, and therefore the design space in the wing-positioning plot decreases up to the point were the aircraft becomes neutrally instable. The aircraft designer chooses if this is an acceptable result, however without any fly-by wire systems and for the sake of safety it is advisable to design the aircraft to be neutrally stable with an additional static margin of 5%.

The DUUC baseline is designed with 8 fan blades per DFS. An analysis with 6, 4, and 3 fan blades per DFS concluded that there is a marginal effect on the OEM, MTOM, and fuel, mass. However the DUUC baseline model shows to have an underestimated fan mass compared to reference fans. A sensitivity analysis on the total DFPE mass variation is done to investigate this uncertainty. On the aerodynamic side, decreasing the number of fan blades shifts the tailless aerodynamic center more forward, however it will not go beyond the most forward c.g. location, and therefore the tailless aircraft will still generate a nose-down pitching moment.

The increased static thrust and therefore higher propulsive efficiency of the DFS proved to have a marginal benefit on the converged DUUC design in terms of OEM, MTOM, and fuel consumption. The total reduction in fuel consumption is in the order of 2kg-4kg, between $\eta_{\text{prop}_{\text{TO}}} = 0.70 - 0.80$. This shows that the cruise phase is dominant for the fuel burn. The main benefit of the ducted-fans, i.e. increased static thrust performance, does not result in a significant benefit on the overall aircraft design.

Because of the uncertainties in the DFPE mass estimatin, a sensitivity analysis is done with a propulsion weight factor ranging from 0.50 to 1.75. This results that MTOM varies from +5.8% to +20.2%, OEM varies from +9.1% to +31.8%, and harmonic fuel burn varies from +8.4% to +21.9%, with respect to the ATR72-600 Initiator model. With decreasing DFPE mass the fuel fraction increases (fuel mass divided by MTOM), meaning that from an engineering point of view the design becomes more efficient. It is decided that from an operational point of view the absolute fuel burn in kilograms per passenger per kilometer is a more effective indication of the fuel efficiency of an aircraft than the fuel fraction. Because the number of passengers and harmonic range is kept constant over all analysis, an aircraft with a lower fuel mass is a more efficient design based on this definition. An increasing DFPE mass shifts the c.g. more aft. This tail moment arm, increases the required downforce, and therefore increases the trim drag and fuel consumption. For a large DFPE mass it is possible that the wing-positioning diagram results an instable aircraft configuration. Manual fine tuning of the DFPE design and location is required to ensure that the DFPE can result a sufficient downforce. For a

A comparison of ideal aircraft with $\eta_{\text{prop}} = 1.0$ in all flight conditions and $W_{\text{duct}} = 0$kg shows that ideal DUUC has still 7.8% higher OEM and 2.9% higher fuel fraction than the ideal ATR72-600 model. This analysis indicates that even in the ideal configuration the chance is unlikely that the DUUC will have a more efficient design compared to its reference aircraft, in terms of of the KPIs (OEM, MTOM, fuel mass).

7.1.5. OVERALL CONCLUSION

The objective of this thesis is to answer the following main research question: ***"What is the effect of the DUUC concept, an aircraft featuring a ducted fan propulsive empennage, on the key performance indicators of the aircraft design, while providing sufficient longitudinal static stability and trimming during flight?"***

At this moment, within the scope of this research, the following answers are found to this question:

1. No direct benefits of the improved static thrust performance of the ducted fans are found on the overall aircraft design
2. The ducted-fan propulsive empennage is a heavy structure, due to the large nacelle diameter and pylon tip mass, which furthermore shifts the OEM c.g. far aft.
3. Since the OEM increases due to the heavy DFPE, larger and more powerful engines are required, which increase the fuel consumption.
4. Far aft OEM c.g. reduces the tail arm, which requires a large tail downforce to remain balanced during flight, which consequently increases the trim drag and therefore fuel consumption.
5. Via an optimization routine it would be possible to develop a more efficient DUUC design, with smaller ducts which still satisfy the stability and balance constraints, however it is unlikely that a more efficient design than a similar sized conventional propeller reference aircraft is resulted.

All research goals as stated in Section 1.4 are completed. Based on the above mentioned conclusions, all hypothesis stated in Section 1.4 are rejected.

7.2. RECOMMENDATIONS

The recommendations in this section are on the one hand aimed on improvements to the Initiator, and secondly to the improvements to the DUUC design.

7.2.1. IMPROVEMENTS TO THE INITIATOR

1. There exists still a large discrepancy in the power loading of turboprop and ducted fan aircraft. It is advised to review the current wing-power loading analysis method, to identify the root cause of this discrepancy. Especially for the DUUC this will have benefits, because a lighter DFPE design shifts the OEM c.g. more front, which increases the tail arm and reduces the trim drag.
2. Improve the trim drag calculation for the DUUC. Currently the superposition method only works for small c.g. shifts during flight, however for swept wings and a larger aft OEM c.g. this method would most likely no longer be valid.

3. Implement the propeller blade geometry sizing module. With this module in place, the propeller analysis modules can be activated, which allow the user to determine the exact propeller efficiency during flight. Currently the Initiator works with propeller propulsive efficiency settings for the take-off, climb, and cruise phase. Therefore the geometries for the fan including the number of blades are chosen arbitrarily. However it would be more favorable if these efficiencies are calculated with analysis methods such as XROTOR and DFDC By doing so the geometry of the turboprop and DFS will have a more direct influence on both the propulsion performance and mass estimation.

7.2.2. IMPROVEMENTS TO THE DUUC ANALYSIS METHODS

1. Implement a more accurate lift and drag model for the ducted fans. Currently the lift and drag performance of the DFPE relies on experimental data, and modified empirical relations. Because the lift and drag analysis of the DFPE is critical to the trim drag calculation, any gains in the lift-drag polar will have major benefits to the overall aircraft design.
2. Detailed computational fluid dynamics (CFD) analysis of the DFPE could give more answers to the interactions between the airflows around the fan, duct, centerbody, pylon, and jet vanes. Similar to the lift-drag model, assumptions were made on the aerodynamic behaviors of these components, because their actual mutual interactions are unknown. The outcomes of this research will also contribute to improving the propulsive efficiency model of the ducted fans. This analysis can be extended to a tandem ducted-fan configuration, to investigate what the effect of the one duct on the other is. Especially in side-slipped flight or high angle of attack flight this could be interesting to investigate.
3. The mass estimation for the DFPE relies mostly on empirical relations, with an exception of the duct shell thickness and blade containment liner thickness. Furthermore, it is probable that the fan mass estimation is underestimated. Additionally, it would be interesting what the forces on the DFPE would be for various extreme flight conditions, high-g turns, hard landing, etc. Via detailed finite element analysis (FEM) it is possible to achieve a more accurate prediction of the structural load in the DFPE, which could result in an optimized DFPE design with a lower mass.

7.2.3. IMPROVEMENTS TO THE DUUC DESIGN

1. Implementing mechanical fixes to cope with the aft shifted OEM c.g. A trim tank in the front of the aircraft shifts the c.g. during flight more forward, hence increasing the tail arm. This will reduce the trim drag significantly. A tail wheel would prevent the aircraft from tipping-over during ground handling.
2. Implementing a tail wheel during ground handling prevents the aircraft from tipping over. It is not proven that this is an essential feature for the DUUC design, however tail-tipping could definitely be a problem with a far aft OEM c.g.
3. Implementing a beam between the ducts, to reduce the structural loading such that the structural mass of the DFPE decreases.
4. Improve the duct design. In the DUUC baseline model a simple NACA0009 shape is used, since it gives the lowest duct mass. However, for the duct shape itself the propulsive performance is not analyzed. Furthermore, in the current design an axi-symmetric duct is chosen, however because of the large downforce requirement to trim the aircraft, it might benefit from a non-axi-symmetric profile which automatically gives more downforce.

7.2.4. FUTURE RESEARCH POSSIBILITIES TO THE DUUC CONCEPT

1. One of possible benefits of the ducted fans is that it could aid to noise shielding. Especially during the take off and landing phase, this could be a great benefit compared to the conventional propeller aircraft. However, to make a good conclusion on this the airflow inside the DFS, and especially the interaction of the airflow between the fan and duct should be investigated. The required model for this analysis should contain a detailed shape of the fan blade and a duct airfoil which is designed accordingly for the correct free-stream conditions and thrust requirement. Currently the fan and duct shapes are chosen arbitrarily. Unfortunately, given the time this topic falls outside the thesis research scope.
2. Although a hybrid-electric version of the DUUC is investigated during the literature research, it was decided to leave it out in the final DUUC model, mainly because the implementation of hybrid electric aircraft in the current version of the Initiator was not available. One of the main benefits of a hybrid electric propulsion system (HEPS) for the DUUC is that it could reduced the pylon tip mass, and therefore the total mass of the DFPE.

BIBLIOGRAPHY

[1] Airbus, *Airbus A350 XWB,* http://www.airbus.com/aircraftfamilies/passengeraircraft/a350xwbfamily/ (), [Online; 27-03-2017].

[2] Airbus, *Technical Specifications A350-900,* http://www.a350xwb.com/technical-specifications/ (), [Online; 27-03-2017].

[3] Janes All the Worlds Aircraft, *Boeing-Douglas DC-3,* https://janes.ihs.com/Janes/Display/1337324 (), [Online; 27-03-2017].

[4] Aerospaceweb, *de Havilland Comet,* http://www.aerospaceweb.org/aircraft/jetliner/comet/, [Online; 27-03-2017].

[5] J.D. Anderson, *Introduction to Flight (7th edition)* (McGraw-Hill Higher Education, 2011).

[6] Historic Wings, *Stipa-Caproni: The Flying Barrel,* http://fly.historicwings.com/2012/10/the-flying-barrel/, [Online; 14-03-2017].

[7] D.M. Black, H.S. Wainauski, C. Rohrback, *Shrouded propellers - a comprehensive performance study,* in *5th AIAA Annual Meetint and Technical Display* (1968).

[8] K.W. Mort, B. Gamse, *A Wind-Tunnel Investigation Of A 7-Foot-Diameter Ducted Propeller - Technical Note 4142*, Tech. Rep. (National Aeronautics and Space Adiministration (NASA), 1967).

[9] K.J. Grunwald, K.W. Goodson, *Aerodynamic Loads On An Isolated Shrouded-Propeller Configuration For Angles Of Attack From -10 to 110 - Technical Note 995*, Tech. Rep. (National Aeronautics and Space Administration (NASA), 1962).

[10] A.I. Abrego, R.W. Bulaga, *Performance study of a ducted fan system,* in *AHS Aerodynamics, Aeroacoustic, Test and Evaluation Technical Specialist Meeting* (2002).

[11] S. Yilmaz, D. Erdem, M. Serif Kavsaoglu, *Effects of Duct Shape on a Ducted Propeller Performance,* in *51st AIAA Aerospace Sciences Meeting including the New Horizons Forum and Aerospace Exposition* (2013).

[12] N.P. Bi, K.R. Kimmel, D.J. Haas, *Performance Investigation of Ducted Aerodynamic Propulsors,* in *First International Symposium on Marine Propulsors.*

[13] R.J. Weir, *Aerodynamic Design Considerations for a Free Flying Ducted Propeller,* in *Atmospheric Flight Mechanics Conference, Guidance, Navigation, and Control and Co-located Conferences* (1988).

[14] A.H. Sacks, J.A. Burnell, *Ducted Propellers - A Critical Review of the State of the Art,* Progress in Aerospace Sciences **3** (1962).

[15] J. Ahn, K. Tae Lee, *Performance Prediction and Design of a Ducted Fan System,* in *40th AIAA/ASME/SAE/ASEE Joint Propulsion Conference and Exhibit* (2004).

[16] H.H. Hubbard, *Sound Measurements for Five Shrouded Propellers at Static Conditions - Technical Note 2024*, Tech. Rep. (National Advisory Committee for Aeronautics (NACA), 1950).

[17] R.D. Oleson, H. Patrick, *Small Aircraft Propeller Noise with Ducted Propeller,* in *4th AIAA/CEAS Aeroacoustics Conference.*

[18] Boeing, *V-22 Osprey,* http://www.boeing.com/defense/v-22-osprey/, [Online; 14-03-2017].

[19] Aviastar, *Bell X-22,* http://www.aviastar.org/helicopters_eng/bell_x-22.php, [Online; 14-03-2017].

[20] N.H.M. van den Dungen, *Literature Study: Synthesis of an aircraft featuring a ducted-fan propulsive empennage*, Tech. Rep. (Delft University of Technology, 2016).

[21] Wikipedia, *Stipa-Caproni,* https://it.wikipedia.org/wiki/Stipa-Caproni, [Online; 11-02-2016].

[22] AviaDejaVu, *Mississippi State University XAZ-1 Marvelette,* http://aviadejavu.ru/Site/Crafts/Craft33749.htm, [Online; 11-02-2016].

[23] Diseno-Art, *Bell X-22,* http://www.diseno-art.com/encyclopedia/strange_vehicles/bell_x-22.html, [Online; 14-03-2017].

[24] Airbus Group, *E-fan Technology Demonstrator,* http://www.airbusgroup.com/int/en/news-media/media~item=cd22fc69-5cc6-4a8f-8387-96f7744396f2~.html, [Online; 11-02-2015].

[25] Rolls-Royce plc., *Trent XWB,* http://www.rolls-royce.com/products-and-services/civil-aerospace/products/civil-large-engines/trent-xwb.aspx, [Online; 15-03-2017].

[26] FLIGHT International, *Dowty ducted propulsor flies,* https://www.flightglobal.com/FlightPDFArchive/1977/197720-202211.PDF, [Online; 15-03-2017].

[27] Janes All the Worlds Aircraft, *Rolls-Royce Trent XWB,* https://janes.ihs.com/Janes/Display/1306513 (), [Online; 15-03-2017].

[28] Jane's All the World's Aircraft, *Kuznetsov NK-93,* https://janes.ihs.com/Janes/Display/1306105, [Online; 04-1-2016].

[29] Aviadejavu, *Ducted Dowty Fan,* http://aviadejavu.ru/Images6/AI/AI77-11/16-2.jpg, [Online; 15-03-2017].

[30] D.P. Raymer, *Aircraft Design: A Conceptual Approach* (American Institute of Aeronautics and Astronautics (AIAA), 2004).

[31] Epstein, *Trent of Engine Bypass Ratio (BPR),* http://web.mit.edu/16.unified/www/FALL/thermodynamics/notes/node84.html, [Online; 15-03-2017].

[32] Ahmed F. El-Sayed, *Aircraft Propulsion and Gas Turbine Engines* (CRC Press by Taylor & Francis Group, 2008).

[33] M. Hoogreef, *Aircraft Design Initiator Documentation,* http://aircraftinitiator.lr.tudelft.nl/index.php/Synthesis/Initiator.

[34] R.J.M. Elmendorp, *Synthesis of Novel Aircraft Concepts for Future Air Travel*, Degree of Master of Science in Aerospace Engineering, Delft University of Technology (2014).

[35] MathWorks, *MATLAB,* http://nl.mathworks.com/products/matlab/?refresh=true.

[36] Janes All the Worlds Aircraft, *Fokker 50,* https://janes.ihs.com/Janes/Display/1336887 (), [Online; 04-01-2016].

[37] Janes All the Worlds Aircraft, *ATR 72,* https://janes.ihs.com/Janes/Display/1342570 (), [Online; 18-12-2015].

[38] J. Van Bogaert, *Assessment of Potential Fuel Saving Benefits of Hybrid-Electric Regional Aircraft*, Degree of Master of Science in Aerospace Engineering, Delft University of Technology (2015).

[39] T. Bouquet, *Modelling the Propeller Slipstrem Effect on the Longitudinal Stability and Control*, Degree of Master of Science in Aerospace Engineering, Delft University of Technology (2016).

[40] E. Torenbeek, *Synthesis of Subsonic Airplane Design* (Delft University Press, 1976).

[41] Federal Aviation Administration (FAA), *FAA Regulations,* https://www.faa.gov/regulations_policies/faa_regulations/, [Online; 29-12-2016].

[42] J. Roskam, *Airplane Design Part I-VII* (DARcorporation, 1985).

[43] V. Harinarain, *Aerodynamic Performance Study on Ducted Propeller System for Propulsion, Control and Stability Applications*, Degree of Master of Science in Aerospace Engineering, Delft University of Technology (2017).

[44] H. Glauert, *The Elements of Aerofoil and Airscrew Theory* (Cambridge Science Classics, 1983).

[45] G.J.J. Ruijgrok, *Elements of Airplane Performance* (VSSD, 2009).

[46] J.D. Anderson, *Fundamentals of Aerodynamics (5th Edition)* (McGraw-Hill Higher Education, 2010).

[47] A. Filippone, *Advanced Aircraft Flight Performance* (New York : Cambridge University Press, 2012).

[48] H.C. Marquardi, *X-22A Progress Report No. 73*, Tech. Rep. (Bell Aerospace Company, 1969).

[49] R.D. Kimberlin, *Flight Testing of Fixed Wing Aircraft* (AIAA Education Series, 2003).

[50] L.L.M. Veldhuis, *Propeller Wing Aerodynamic Interference*, Ph.D. thesis, Delft University of Technology (2005).

[51] Massachusetts Institude of Technology - Online Educational Learning Unit, *Performance of Propellers,* .

[52] Snorri Gudmundsson, *General Aviation Aircraft Design - Applied Methods and Procedures* (Elsevier, 2014).

[53] M.J. Werle, *Aerodynamic Loads and Moments on Axisymmetric Ring-Wing Ducts,* AIAA Journal **52** (2014).

[54] H.S. Ribner, *The Ring Airfoil in Nonaxial Flow,* Journal of the Aeronautical Sciences **14** (1947).

[55] A. Maqsood, T. H. Go, *Aerodynamic Estimation of Annular Wings Based on Leading-Edge Suction Analogy,* AIAA Journal **52** (2013).

[56] M. Drela, H. Youngren, *XROTOR,* (2014), http://web.mit.edu/drela/Public/web/xrotor/.

[57] M. Drela, H. Youngren, *Ducted Fan Design Code (DFDC) - Axisymmetric Analysis and Design of Ducted Rotors*, Tech. Rep. (2005) http://web.mit.edu/drela/Public/web/dfdc/.

[58] M. Drela, H. Youngren, *XFOIL - Subsonic Airfoil Develpoment System,* (2013), http://web.mit.edu/drela/Public/web/xfoil/.

[59] W.F. Durand, *Aerodynamic Theory* (Springer, 1935).

[60] T. Sinnige, *The Effects of Pylon Blowing on Pusher Propeller Performance and Noise Emissions*, Degree of Master of Science in Aerospace Engineering, Delft University of Technology (2013).

[61] R. Woroble, M.G. Mayo, *Advanced General Aviation Propeller Study*, Tech. Rep. (Hamilton Standard and National Aeronautics and Space Adiministration (NASA), 1971).

[62] A.J.B. Jackson, *Optimisation of Aero and Industrial Gas Turbine Design for the Environment*, Ph.D. thesis, Cranfield University School of Engineering (2009).

[63] P. Lolis, *Development of a Preliminary Weight Estimation Method for Advanced Turbofan Engines*, Ph.D. thesis, Cranfield University School of Engineering (2014).

[64] P. Giannakakis, *Design Space Exploration and Performance Modelling of Advanced Turbofan and Open-Rotor Engines*, Ph.D. thesis, Cranfield University School of Engineering (2013).

[65] B. Omat and G.W. Klees, *A Method to Estimate Weight and Dimensinos of Large and Small Gas Turbine Engines - Final Report*, Tech. Rep. (National Aeronautics and Space Adiministration (NASA), 1979).

[66] D.C. Giancoli, *Physics for Scientists & Engineers with Modern Physics (4th edition)* (Prentice Hall, 2008).

[67] Aerospace Specification Metals (ASM) inc., *Aluminimum 7075-T6,* http://asm.matweb.com/search/SpecificMaterial.asp?bassnum=MA7075T6, [Online; 04-01-2017].

[68] DuPont, *Kevlar Technical Guide,* http://www.dupont.com/content/dam/dupont/products-and-services/fabrics-fibers-and-nonwovens/fibers/documents/Kevlar_Technical_Guide.pdf, [Online; 04-01-2017].

[69] Y. Bin, *Blade containment evaluation of civil aircraft engines,* Chinese Journal of Aeronautics **26** (2013).

[70] T.H.G. Megson, *Aircraft Structures for Engineering Students (5th edition)* (Elsevier Aerospace Engineering Series, 2013).

[71] J.A. Mulder, W.H.J.J. van Saveren, J.C. van der Vaart, E. de Weerdt, C.C. de Visser, A.C. in 't Veld, E. Mooij, *Flight Dynamics Lecture Notes* (Delft University of Technology, 2013).

[72] H. Youngren, *Athena Vortex Lattice (AVL),* http://web.mit.edu/drela/Public/web/avl/.

[73] E. Obert, *Aerodynamic Design of Transport Aircraft* (Delft University Press, 2009).

[74] A. Elham, *Multidisciplinary Design Optimization of Lifting Surfaces,* Ph.D. thesis, Delft University of Technology (2013).

[75] M.F. Nita, *Aircraft Design Studies Based on the ATR 72,* Degree of Master of Science in Aeronautical Engineering, Hamburg University of Applied Sciences (2008).

[76] Airliners.net, *Ilhushin IL-62M,* http://www.airliners.net/photo/Russia-State-Transport-Company/Ilyushin-Il-62M/623936/L, [Online; 23-03-2017].

[77] Skybrary, *Reducted Thrust Take-Off,* http://www.skybrary.aero/index.php/Reduced_Thrust_Takeoff, [Online; 25-03-2017].

[78] H. G. Visser and R. A. A. Wijnen, *Optimization of Noise Abatement Departure Trajectories,* Journal of Aircraft **38** (2001).

[79] IHS Janes, *Jane's All The World's Aircraft,* https://janes.ihs.com/janes/home.

[80] National Aerospace Laboratory (NLR), *NLR Research Aircraft Cessna Citation II,* http://www.nlr.nl/downloads/e1123-nlr-cessna-citation-ii.pdf, [Online; 27-03-2017].

[81] P.M. Peeters, J. Middel, A. Hoolhorst, *Fuel efficiency of commercial aircraft, an overview of historical and future trends,* Tech. Rep. (National Aerospace Laboratory (NLR), 2005).

[82] American Museum of Aviation, *Douglas DC-3 Technical Specifications,* http://www.prop-liners.com/dc3tech.htm, [Online; 27-03-2017].

[83] Federal Aviation Administration (FAA), *Pilot's Handbook of Aeronautical Knowledge (FAA-H-8083-25B)* (U.S. Department of Transportation, 2016).

A

FUEL EFFICIENCY CALCULATIONS

Table A.1: Performance characteristics of various civil transport aircraft

Parameter	Unit	DC-3 [3]	Comet-4 [4]	A350 [2]
Number of passengers	-	21	81	440
Harmonic range	km	1500	33600	88000
Harmonic fuel	kg	2194	5190	14350
Fuel efficiency	g/pax/km	70	80	14

The fuel efficiency (η_{fuel}, [g/pax/km]) is calculated with:

$$\eta_{\text{fuel}} = \left(\frac{Fuel}{Pax/Range}\right) 1000 \tag{A.1}$$

The harmonic fuel for the Comet is calculated with [42]:

$$FM = MTOM - PM_{\text{max}} - OEM \tag{A.2}$$

The fuel mass (FM, [kg]]) is calculated based on the maximum take-off mass ($MTOM$=73480kg), maximum payload mass (PM_{max}=5670kg), and operational empty mass (OEM =34210kg) [4].

The harmonic fuel for the DC3 is calculated with:

$$FM = (V_{\text{tank}})\left(\rho_{\text{fuel}}\right) \tag{A.3}$$

The fuel mass (FM, [kg]) is calculated based on the tank volume (V_{tank}=3043L [82]) and fuel density (ρ_{fuel}= 0.721kg/L [83]).

B

INITIATOR MODIFICATIONS

In the one year of thesis research, much is updated to the Initiator to first of all improve the modeling of turboprop aircraft, and secondly to implementation of the DUUC concept. This appendix elaborates on the various modifications done to the Initiator.

B.1. MODIFIED FILES

The following files are modified or added during the thesis. It is very well possible that also other files are modified, however the following list contains the most important ones:

1. Modified engine model geometry
   (a) `Geometry/@Engine`
   (b) `Geometry/@Motor` [NEW]
   (c) `Geometry/@Fan` [NEW]
   (d) `Geometry/@Motor` [NEW]
   (e) `Geometry/@Pylon` [NEW]
   (f) `Geometry/@Revolution` [NEW]
2. Modified engine sizing method
   (a) `SizingModules/@GeometryEstimation/estimateEngines.m`
   (b) `SizingModules/@GeometryEstimation/estimateControlSurfaces.m`
   (c) `SizingModules/@GeometryEstimation/EstimatePylons.m` [NEW]
   (d) `SizingModules/@GeometryEstimation/getHorizontalTailEffectiveness.m` [NEW]
   (e) `SizingModules/@GeometryEstimation/getPylonCleanArea.m` [NEW]
   (f) `SizingModules/@GeometryEstimation/getTailArm.m` [NEW]
   (g) `SizingModules/@GeometryEstimation/positionEngines.m`
   (h) `SizingModules/@GeometryEstimation/run.m`
3. New ducted fan system sizing methods
   (a) `SizingModules/@GeometryEstimation/estimateDuctedFanSystem.m`
   → optimizes AR_{duct} and RPM for certain horizontal tail effectiveness (η_{H})
   (b) `SizingModules/@GeometryEstimation/estimateDuctedFanSystemManual.m`
   → manually varies AR_{duct} and RPM until (η_{H}) requirement is met
   (c) `SizingModules/@GeometryEstimation/estimateDuctedFanSystemNewton.m`
   → uses Newton-Raphson method to choose AR_{duct} and RPM which satisfy the η_{H} requirement
   (d) `SizingModules/@GeometryEstimation/estimateDuctedFanSystemInterpolate.m`
   → uses "$1/x$" method to choose AR_{duct} and RPM which satisfy the η_{H} requirement
   (e) `SizingModules/@GeometryEstimation/estimateDuctedFanSystemFast.m`
   → mix between Newton and "$1/x$"-Interpolation methods, to get a fast result for AR_{duct} and RPM which satisfy the η_{H} requirement
   (f) `SizingModules/@GeometryEstimation/estimateDuctedFanSystemSimple.m`
   → this function modifies AR_{duct} and RPM until a certain reference ($S_{\text{H}} \cdot C_{L_\alpha}$) product is met
   (g) `SizingModules/@GeometryEstimation/estimateDuctedFanSystemAR.m`
   → [DEFAULT METHOD] this function just uses the AR_{duct} and RPM of the settings file to model the DFS

4. New detailed propeller model
   (a) `AnalysisModules/@PropellerModel` [NEW]
5. Implemented the Ducted Fan Design Code (DFDC) tool
   (a) `AnalysisModules/@DFDC` [NEW]
6. Modified Class 2 Weight Estimation for the engine
   (a) `AnalysisModules/@Class2WeightEstimation/getDuctMass.m` [NEW]
   (b) `AnalysisModules/@Class2WeightEstimation/getEngineWeight.m`
   (c) `AnalysisModules/@Class2WeightEstimation/getPropMass.m` [NEW]
   (d) `AnalysisModules/@Class2WeightEstimation/getPropMotorMass.m` [NEW]
   (e) `AnalysisModules/@Class2WeightEstimation/getPylonMass.m` [NEW]
   (f) `AnalysisModules/@Class2WeightEstimation/run.m`
7. Modified Parasite Drag Estimation
   (a) `AnalysisModules/@ParasiteDragEstimation/engineDrag.m` → Modified for DUUC
   (b) `AnalysisModules/@ParasiteDragEstimation/fuselageDrag.m` → Included main landing gear fairing drag
8. Modified Drag Module
   → `AnalysisModules/@DragModule`
   (a) `AnalysisModules/@DragModule/run.m` → Modified for DUUC with tail trim drag
   (b) `AnalysisModules/@DragModule/getDFSInducedDrag.m` [NEW]
9. Modified propeller efficiency calculation in MissionAnalysis for turboprop aircraft, linked it to `@PropellerModel`
   (a) `AnalysisModules/@MissionAnalysis/climbprop.m`
   (b) `AnalysisModules/@MissionAnalysis/cruiseprop.m`
   (c) `AnalysisModules/@MissionAnalysis/descentprop.m`
   (d) `AnalysisModules/@MissionAnalysis/holdprop.m`
   (e) `AnalysisModules/@MissionAnalysis/landingprop.m`
   (f) `AnalysisModules/@MissionAnalysis/takeoffprop.m`
10. Modified the Horizontal Stability Estimation with a DUUC specific implementation
    (a) `DesignModules/@HorizontalStabilityEstimation/run.m`
    (b) `DesignModules/@HorizontalStabilityEstimation/InputVariables.m` → modified inputs for the DUUC
    (c) `DesignModules/@HorizontalStabilityEstimation/LoadingDiagramDuctedFan.m` [NEW]
    (d) `DesignModules/@HorizontalStabilityEstimation/PlotHorizontalStabilityResults.m` [NEW]
    (e) `DesignModules/@HorizontalStabilityEstimation/StabilityAero.m` → modified inputs for the DUUC
    (f) `DesignModules/@HorizontalStabilityEstimation/TailObjective.m` → Implemented trim diagram
    (g) `DesignModules/@HorizontalStabilityEstimation/TailObjectiveDUUC2.m` [NEW]
    (h) `DesignModules/@HorizontalStabilityEstimation/UpdateDFS.m` [NEW]
    (i) `DesignModules/@HorizontalStabilityEstimation/UpdateTailEffectiveness` [NEW]
11. Modified XML reader such that a "DUUC"-type aircraft is correctly defined
    (a) `WorkflowModules/@XMLReader`

The specific DFPE implementation is done in `estimateControlSurfaces.m`. The reason why the DFPE is sized in this specific file, is that normally this file sizes the horizontal and vertical stabilizers. Because the DFPE also functions as a horizontal and vertical stabilizer, it was found more convenient to implement the DFPE in the same file. The function `estimateControlSurfaces.m` calls one of the `estimateDuctedFansystem.m` functions to size the DFS of the DUUC.

As can be seen in the list, there exist many functions to estimate the sizes of the DFS. The reason for this is that a long period of time it was believed that the best way to come up with an initial size of the DFS is to vary AR_{duct} and fan RPM to acquire a predefined horizontal tail efficiency (η_{H}), which is basically the tail volume coefficient method appended with the lift gradient (C_{L_α}) of the horizontal stabilizer. The initial DFS estimate would then be overwritten by the higher-order horizontal stability estimation (HSE) method, later in the aircraft design convergence process. However, it turned out that the $\eta_{\text{prop}_{\text{H}}}$ method only works with a good reference value, and secondly modifying the AR_{duct} influences the (C_{L_α}) of the duct which results in dynamic behavior of the solution in the HSE-module. Therefore it is decided to always use the `estimateDuctedFansystemAR.m` function, since this sizes the DFS based on the AR_{duct} and RPM as defined in the aircraft settings file.

The DUUC definition is implemented in the XML reader module. Any aircraft becomes a type "DUUC" if all of the following conditions are satisfied:

DUUC Aircraft Type Definition

- Engine-types = "DuctedFan"
- No horizontal tail is defined in the aircraft definition file
- No vertical tail is defined in the aircraft definition file

The settings file for turboprop aircraft and the DUUC now contain the following settings:

- MaxPropTipMach
- RPM
- SpinnerFanRatio
- FanTipClearanceRatio
- NacelleAspectRatio
- NacelleTcRatio
- FanDuctOffset
- PylonEstimationAirfoil
- MotorLocation (nacelle or fuselage)
- CLaDFSfactorDesign (only used by `estimateDuctedFanSimple.m`)
- HTailEffectiveness (reference value, not used by `estimateDuctedFansystemAR.m`)
- FuselageClearance
- PropulsionWeightFactor
- NacelleWeightFactor
- MaxJetVaneDeflection
- PylonStabilityMode (determines if pylon area is used for $S_{H_{proj}}$)
- MainGearFairingDragIncrement

B.2. MODIFIED ENGINE GEOMETRY

A major update to the core of the program had to be done to implement a more sophisticated engine model, such that the user is able to design the various components of the engine to model various types of engine architectures: turbofan, turboprop, ducted fan, electric motors, etc. The engine model now consists of the items: Motor (gas generator or electric motor), Fan, Pylon, Nacelle (duct), and Centerbody. Figure B.1 indicates how the engine geometry is updated from "floating tubes" to a more accurate engine model.

Originally, the Initiator was designed for turbofan aircraft, and only later the turboprop aircraft were added. The old engine model consisted of a single object, named `Engine`, with properties such as, diameter, length, thrust, bypass ratio, etc. Even more, the geometry of this engine model consisted of an airfoil, which was revoluted via the wing geometry-class to get a circular tube, which floated under the wings or near the fuselage. The problem is that for turboprop aircraft the designer needs to have more information about the geometry of the propeller/fan, such as fan diameter and propeller efficiencies at various points in flight. The old engine object included various propeller-specific properties, however this is not a clear way of object-oriented coding. Especially, when ducted fans have to be implemented.

The conclusion was that there existed a significant need to update the definition of the engine model. The `Engine` class now consists of the following geometry sub-classes:

1. `Motor` (i.e. gas generator)
2. `Fan` (same as propeller)
3. `Pylon`
4. `Nacelle` (same as duct, optional)
5. `Centerbody`

An additional geometry-class named `Revolution` is made, which allows the designer to revolute any arbitrary airfoil along a specified radius. By doing so, it becomes very easy to make any type of nacelle, motor, and centerbody geometries. Furthermore, the reference line for the revolute object is the centerline of it. For example, the reference line for a nacelle is always the centerline. In contrary to the previous engine model, which used the wing-class to model nacelles, the reference line was the top airfoil in the geometry.

With these sub-classes, virtually any aircraft engine can be modeled. For example, a turbofan `Engine` consists of all above mentioned engine sub-classes, and a turboprop `Engine` contains all above mentioned engine sub-classes, except for the nacelle. The `Fan` in the case of a turboprop is off course the propeller, but for consistency within the Initiator the naming of the sub-class should not change.

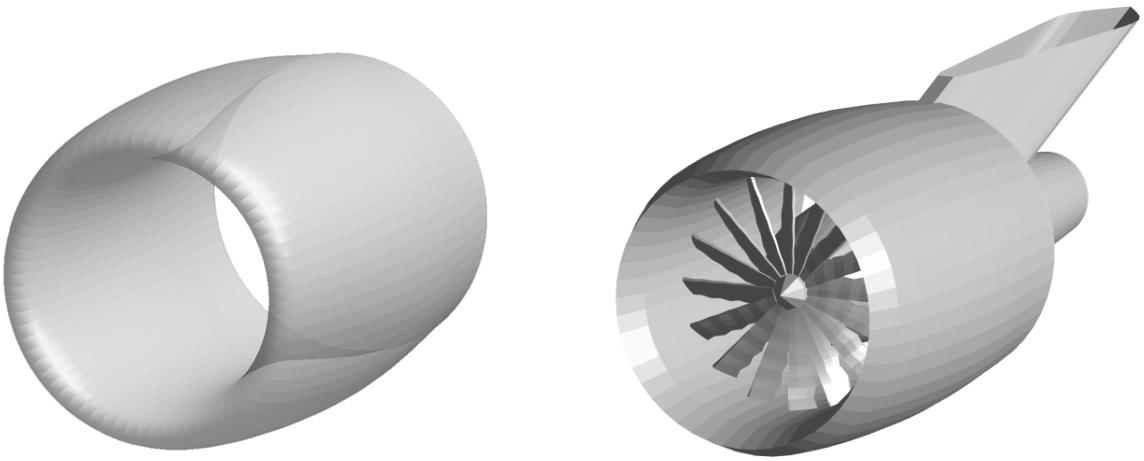

(a) Old Geometry (b) New Geometry

Figure B.1: Comparison of Initiator old vs. new engine geometries

The `Motor` is the gas-generator in all cases. For conventional engines, this class is of type "Turbine". For unconventional engines, such as hybrid-electric configurations, the type of this class can be easily set to "Electric".

Consequently, since the engine model is more refined, the `Class2WeightEstimation` also had to be updated. This analysis module now includes a weight estimation for each of the individual components, as discussed in Chapter 4.

The major benefit of the reconfigured engine model, is that the Initiator has more design freedom in engine architectures, which should prevent a lot of hassle with coding all sorts of aircraft engines.

B.3. PROPELLER IMPLEMENTATION

In addition to the updated engine model, it was required to implement a propeller model to ensure that the propulsive performances of turboprops and ducted fans can be modeled and analyzed properly. Originally the propeller or fan was not even modeled as an existing geometry, merely as an actuator disk. Based on the work on the Propeller Analysis Program, the same geometry definitions are implemented in the Initiator, to ensure that propeller map outputs of PAP can easily be transferred into the Initiator.

Currently 2 additional analysis modules have been included for propellers: `@PropellerModel` and `@DFDC`. These analysis modules are elaborated further.

B.3.1. @PROPELLERMODEL

The geometry of the propeller is based on the radial distribution of the blade pitch β, and chord lengths, see Figure B.2. The geometry of the propeller, i.e. `Fan`-class, is defined via a `Geometry.dat` file of the specific propeller, which can be found in the propeller data-base in the data folder: `\Data\PropellerDB`. The propeller name is defined in the main aircraft file `<aircraft>.xml`. This name corresponds to one of the propellers in the database. `@PropellerModel` is used to acquire the airfoil polars of the propeller blade elements. The propeller analysis program (PAP), see Chapter 3, can be used to get these polars, because the output of PAP is designed in such a manner that it can directly be implemented in the Initiator.

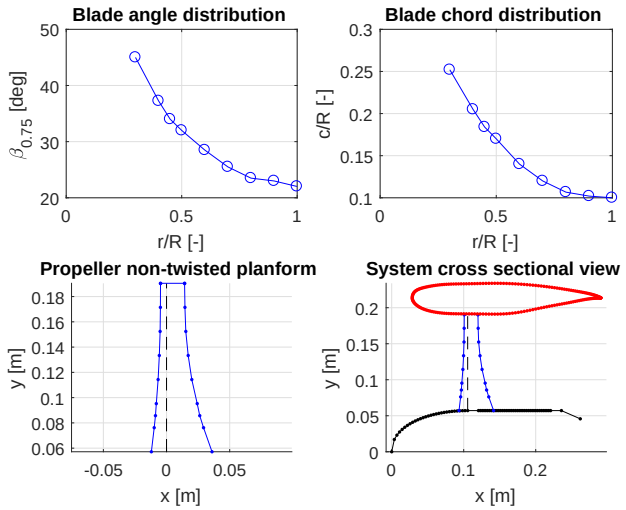

Figure B.2: Example of `DuctedFan` type geometry

B.3.2. @DFDC

Secondly, a DFDC-module is implemented to analyze the performance of the DUUC's DFS. This module returns first of all the propeller performances, which are used in the various Initiator modules, such as for the determination of the fuel consumption in `@MissionAnalysis`. Furthermore, this module is used to determine the pressure distribution inside the duct, which is used to determine the required duct shell thickness and therefore its weight, see Section 4.3.4.

It should be stressed that `@DFDC` only gives reasonable output, if the fan inside the DFS is designed properly. If one decides to put an basic duct around a standard open-rotor propeller, the chances are likely that DFDC does not give output at all, because the solver was not able to find a converged solution. Hence the fan inside the DFS should be designed accordingly for the respective flight conditions.

C

Skin Friction Calculation

This appendix shows the empirical method which is used to calculate the skin friction of the DFPE components. The method is an existing method within the Initiator, and is based on Roskam Aircraft Design Volumes [42].

In case of a laminar flow, the friction coefficient is solely depending on the Reynolds number (Re), and is calculated with:

$$C_{f_{\text{laminar}}} = \frac{1.328}{\sqrt{Re}} \tag{C.1}$$

In case of a turbulent flow, two methods exist to calculate the turbulent friction coefficient $C_{f_{\text{turbulent}}}$. The first method is to interpolated a digitalized version of Figure C.1.

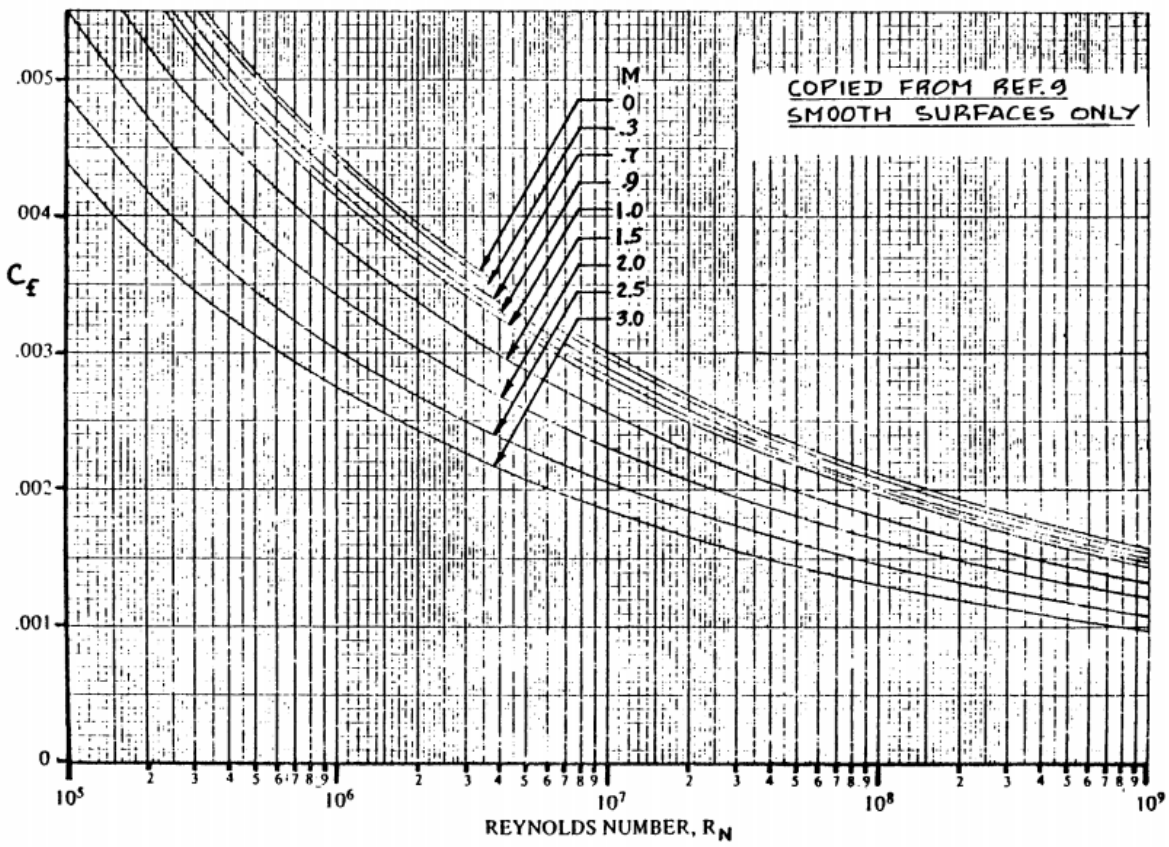

Figure C.1: Turbulent mean skin-friction coefficient, acquired from Roskam volume VI, Chapter 4, figure 4.3. [42]

Another manner to calculate the turbulent friction coefficient is:

$$C_{f_{sg}} = \frac{0.074}{Re_{sg}^{0.2}} \tag{C.2}$$

The Reynolds number which is used to calculate $C_{f_{sg}}$ is calculated with:

$$Re_{sg} = 39.5 \frac{c}{k_{sg}^{1/0.94}} \tag{C.3}$$

Where the characteristic length of the object in the streamwise direction is given by (c, [m]), and the equivalent sand grain thickness is $k_{sg} = 0.001\text{in} = 2.54\text{e}^{-5}\text{m}$.

Based on Roskam's fit of Figure C.1, and the equivalent sand grain thickness given by Equation (C.2), the maximum value is chosen for $C_{f_{\text{turbulent}}}$.

Once all friction coefficients are determined, the correct one will be chosen based on the Reynolds number. The actual Reynolds number will be compared to a transition Reynolds number, which has a default setting of $Re_{tr} = 1\text{e}^6$. If $Re_{tr} > Re$, the flow is laminar and therefore $C_F = C_{f_{\text{laminar}}}$. If the flow is turbulent, the friction coefficient becomes:

$$C_f = \frac{Re_{tr} C_{f_{\text{laminar}}} + (Re - Re_{tr}) C_{f_{\text{turbulent}}}}{Re} \tag{C.4}$$

D

PROPELLER ANALYSIS PROGRAM

This appendix contains various flow diagrams which describe all processes within the propeller analysis program (PAP). This program is developed during the thesis to compare the propulsive performances between ducted and unducted fans, and secondly to perform a parametric study to the main ducted fan design parameters.

The following program protocols are presented:

1. `SingleAnalysis`: the user performs a point analysis with the fan system, for specific free-stream conditions
2. `MultiAnalysis`: the user performs an analysis for a range of advance ratios, where one of the fan system design parameters is modified
3. `MapAnalysis`: similar to *MultiAnalysis*, only the fan system design parameter which is modified is the blade pitch $\beta_{0.75}$

Each propeller in the PAP propeller database has a separate folder. The essential files which determine the basic propeller geometry, are the following:

1. `Design.dat`
2. `Geometry.dat`
3. `CenterBody.dat`
4. `DuctAirfoil.dat` (only for ducted fans)

The blade airfoil coordinates (`Section.dat`) are not necessary, as long as the 2D aerodynamic properties of the blade elements are provided (`Polars2D.mat`). If the 2D airfoil polars are not present, XFOIL will be used to make `Polars2D.mat`.

Since the propeller analysis tools do not work with the actual 2D airfoil polars, a conversion is needed to generate the airfoil characteristic properties. These properties are basically extracted from the actual 2D airfoil polars, such as the maximum lift coefficient, lift gradient, etc.

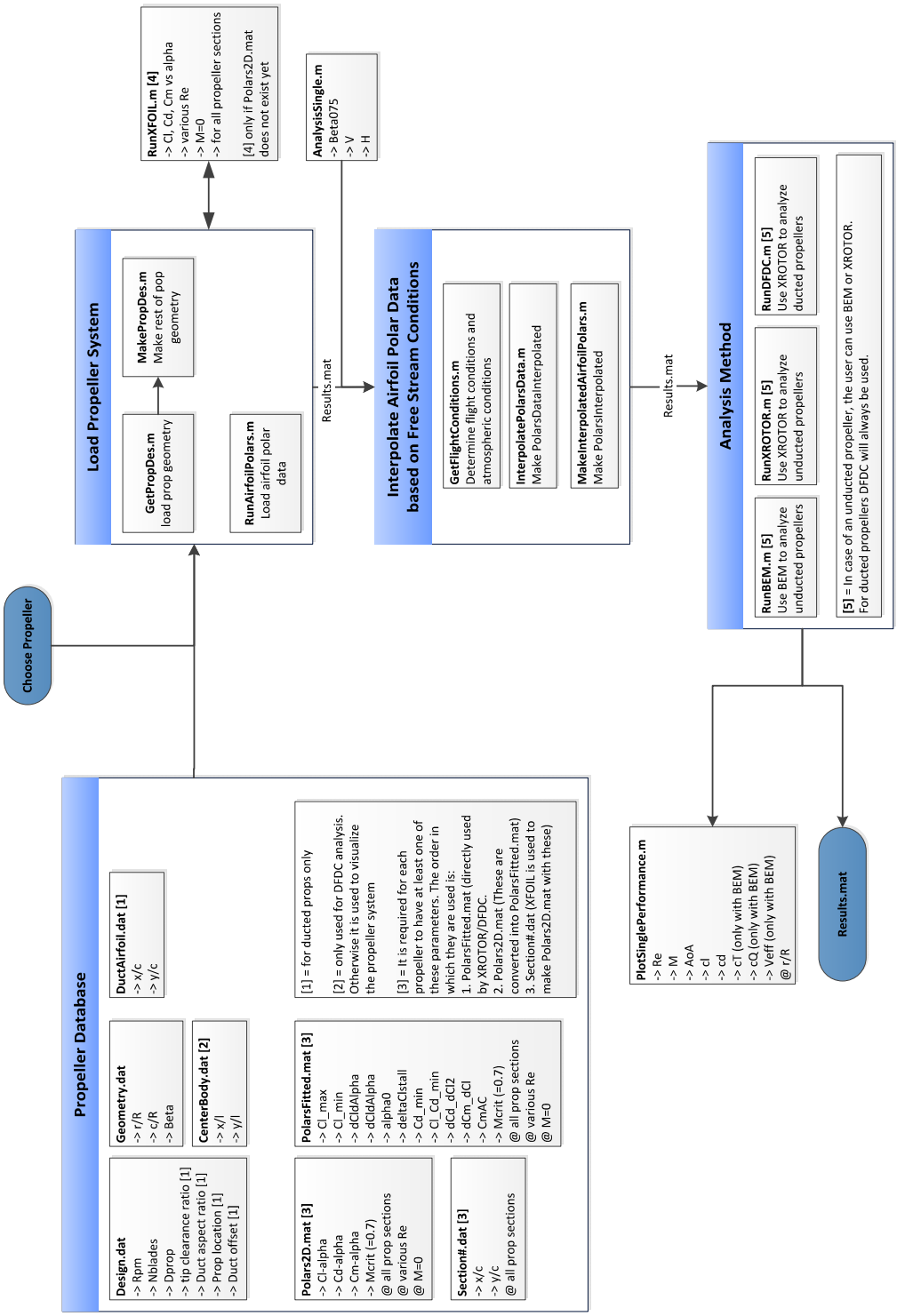

Figure D.1: PAP single analysis flow diagram

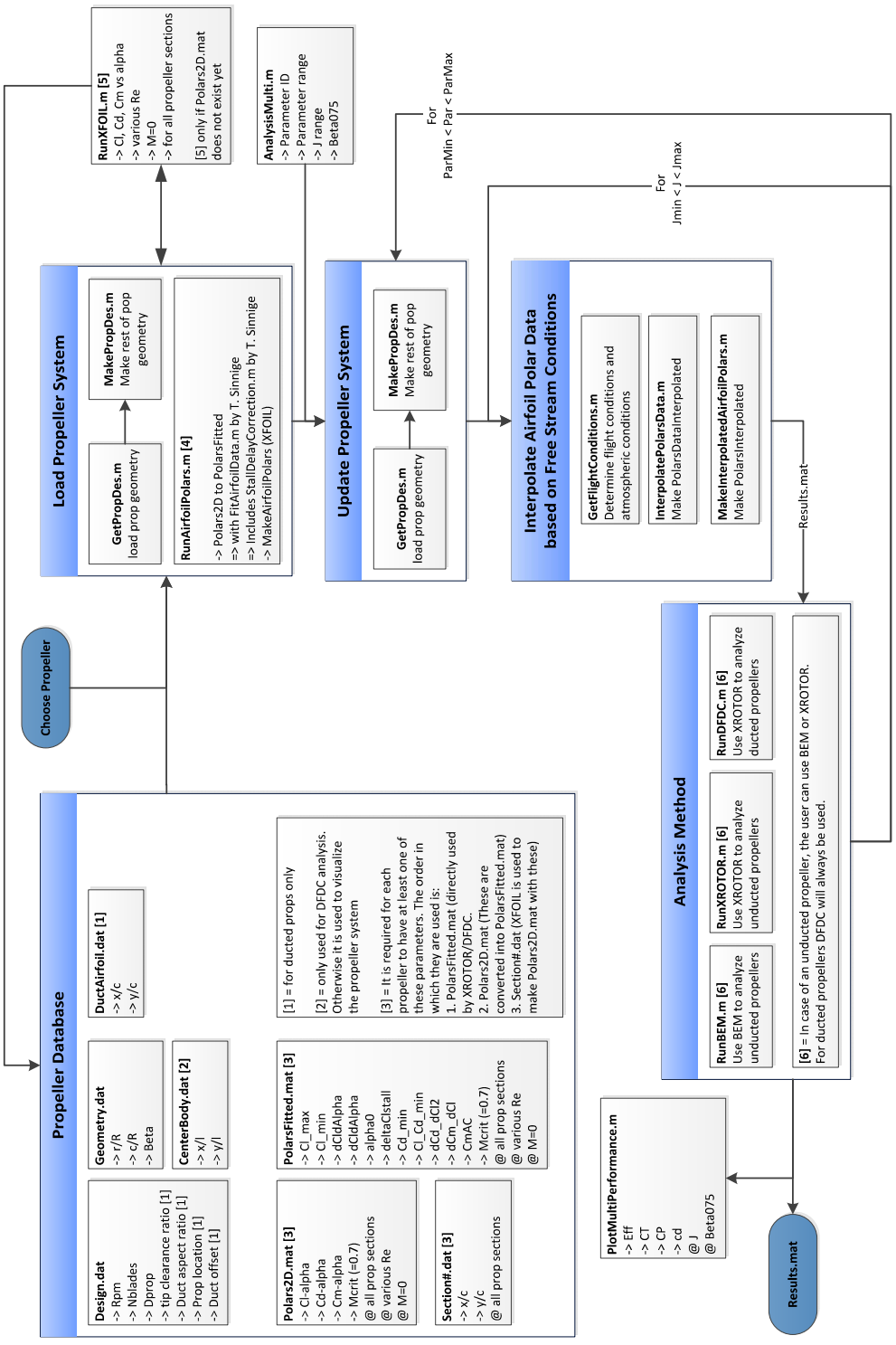

Figure D.2: PAP multi analysis flow diagram

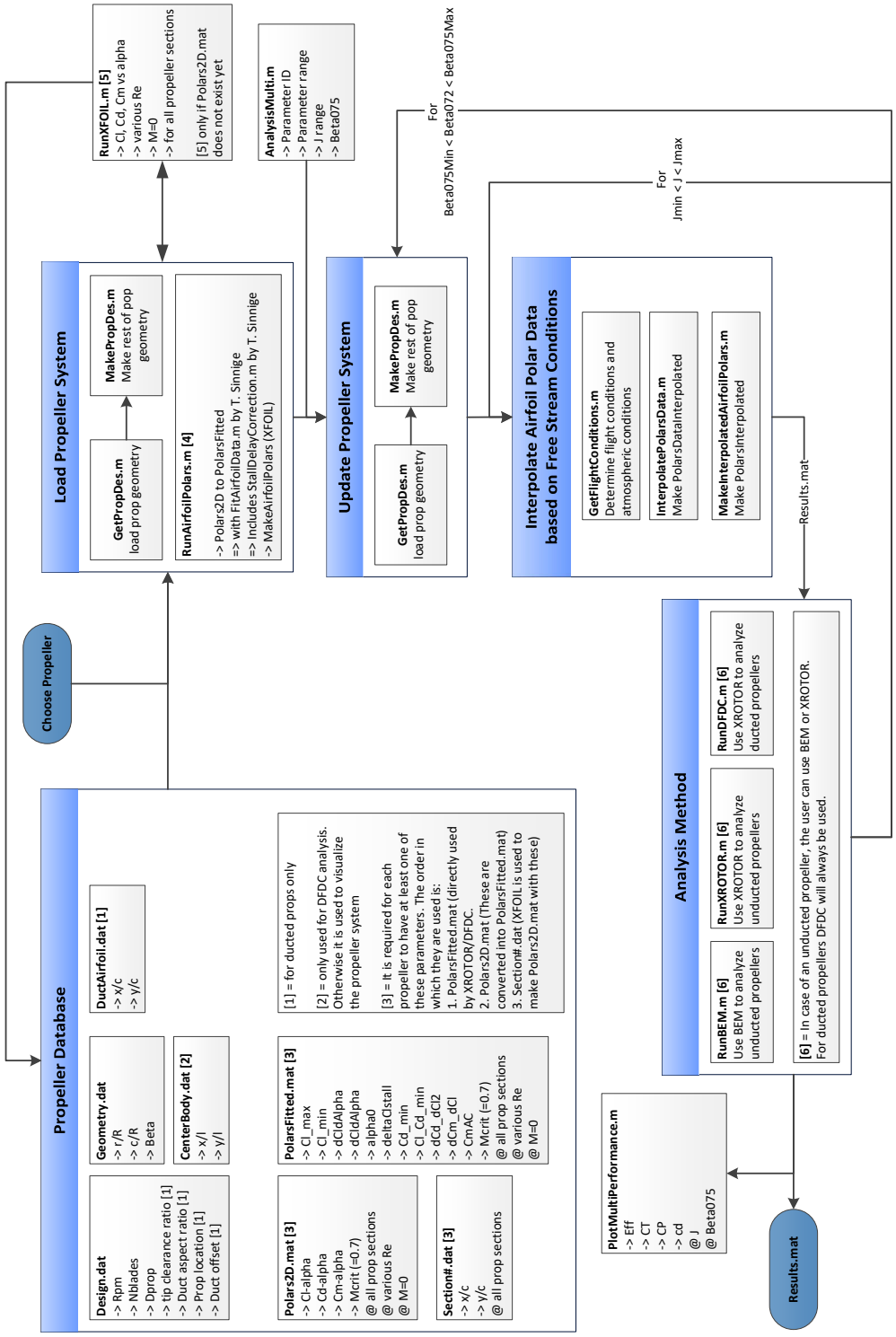

Figure D.3: PAP performance map analysis flow diagram

E

TURBOPROP REFERENCE DATA

The reference data presented in this appendix is used to compare various turboprop mass estimation methods.

Table E.1: Turboprop statistical data, acquired from Jane's All The Wolrd's Aircraft online database [79].

Type	**Power** [kW]	**Dry mass** [kg]	**Length** [m]	**Diameter** [m]
Pratt-Whitney PW118	1127	391	2.057	1.011
Pratt-Whitney PW118A, 118B	1127	394	2.057	1.011
Pratt-Whitney PW119B	1293	416	2.134	1.011
Pratt-Whitney PW120	1231	418	2.134	1.011
Pratt-Whitney PW121	1268	425	2.134	1.011
Pratt-Whitney PW123, 123B, 123AF, 123C, 123D, 123F	1514	450	2.134	1.067
Pratt-Whitney PW150A	2942	690	2.423	1.345
Ivchenko-Progress TV3-117VMA-SBM1	2089	570	2.954	1.561
Ivchenko-Progress AI-25 1075	1857	370	3.096	1.450
Rolls-Royce Dart Mk 21	1425	575	2.500	0.963
Rolls-Royce Dart Mks 525	1342	560	2.480	0.963
Rolls-Royce Dart Mks 529	1484	560	2.480	0.963
Rolls-Royce Dart Mks 536	1368	561	2.480	0.963
Rolls-Royce Dart Mks 552	1581	561	2.480	0.963
Rolls-Royce Dart Mk 542	2051	628	2.527	0.963
Rolls-Royce Dart Mk 201	2215	675	2.527	0.963

Table E.2: Propeller statistical data for large twin engine aircraft, acquired from an advanced general aviation propeller study [61]. Activity Factor is presented for the entire propeller. The power is presented for one engine.

Aircraft	**Model**	**Blades**	**RPM**	**Speed** [m/s]	**Diameter** [m]	**AF** -	**Power** [kW]	**Mass** [kg]
Twin Otter Prototype	23LF-321	3	2200	82.26	2.59	110	410	67.6
Handly Page HP 137	23LF-329	3	1783	89.41	2.59	110	597	68.9
Handly Page HP 137	23LF-333	3	1783	89.41	2.44	120	597	65.3
Aero-Commander	33LF-307	3	2000	111.76	2.13	109	429	54.4
Aero-Commander	33LF-327	3	2000	111.76	2.36	96	429	54.4
1500 HP	1500 HP	3	1563	136.35	3.35	133	1119	161.0
1500 HP	1500 HP	3	1563	136.35	3.35	133	1119	140.2
DHC-7	DHC-7	4	1210	120.70	3.43	116	855	171.0
DHC-7	DHC-7	4	1210	120.70	3.43	116	850	145.1

F

TORENBEEK CLASS 2 WEIGHT ESTIMATION

This appendix presents an overview of the Torenbeek Class 2 Weight Estimation method, which is implemented in the Initiator to calculate the aircraft component masses. The following material is extracted from Roskam's aircraft design handbook part V, which are valid for light commercial transport propeller aircraft [42].

F.1. DESIGN DIVE SPEED

$$V_D \geq 1.25 V_C \tag{F.1a}$$

$$M_D \geq 1.25 M_C \tag{F.1b}$$

$$EAS = TAS\sqrt{\frac{\rho}{\rho_0}} \tag{F.1c}$$

$KEAS$ = Equivalent airspeed $[kts]$
V_C = Cruise speed $[KEAS]$
V_D = Dive speed $[KEAS]$
M_C = Cruise Mach number $[-]$
M_D = Dive Mach number $[-]$
TAS = True airspeed $[kts]$
ρ = Air density at cruise altitude $[kg/m^3]$
ρ_0 = Air density at sea level $[kg/m^3]$

F.2. STRUCTURAL WEIGHT ESTIMATION

$$W_{struct} = W_{wing} + W_{fuselage} + W_{ht} + W_{vt} + W_{ng} + W_{lg} \tag{F.2}$$

F.2.1. WING GROUP

$$W_{wing} = 0.0017 W_{MZF} (b/\cos\Lambda_{0.5c})^{0.75} \left[1 + \sqrt{6.3\cos\Lambda_{0.5c}/b}\right] (n_{ult})^{0.55} (bS/t_r W_{MZF} \cos\Lambda_{0.5c})^{0.30} \tag{F.3}$$

b = Wing span $[ft]$
n_{ult} = ultimate load factor, (=1.5 × limit load factor) $[-]$
S = Wing surface area $[ft^2]$
t_r = Maximum airfoil thickness at the wing root $[ft]$
$\Lambda_{0.5c}$ = Sweep angle at half of the wing chord $[deg]$
W_F = Fuel weight $[lb]$
W_{MZF} = Maximum zero fuel weight = $W_{TO} - W_F$ $[lb]$
W_{wing} = Wing weight $[lb]$

NOTES

1. Equation (F.2.1) includes the weight of normal hight lift devices as well as ailerons

2. For spoilers and speed brakes 2 percent should be added.
3. If the airplane has 2 wing mounted engines, reduce the wing weight by 5 percent.
4. If the landing gear is not mounted under the wing, reduce the wing weight by 5 percent.

F.2.2. TAIL GROUP

The following equations for the horizontal and vertical tail, h.t. and v.t., are valid for aircraft with a design dive speed above $250 kts$.

$$W_{ht} = K_{ht} S_{ht} \left[3.81 \left(S_{ht}^{0.2} V_D\right) / \left(1000 \cos \Lambda_{0.5c_h}{}^{0.5}\right) - 0.287\right] \tag{F.4}$$

$$W_{vt} = K_{vt} S_{vt} \left[3.81 \left(S_{vt}^{0.2} V_D\right) / \left(1000 \cos \Lambda_{0.5c_v}{}^{0.5}\right) - 0.287\right] \tag{F.5}$$

b_{vt} Span of the vertical tail $[ft]$
K_{ht} = 1.0 for fixed incidence stabilizers; 1.1 for variable incidence stabilizers $[-]$
K_{vt} = 1.0 for fuselage mounted horizontal tails $[-]$;
= $1 + 0.15 (S_{ht} z_{ht} / S_{vt} b_{vt})$ for fin mounted horizontal stabilizers $[-]$
S_{ht} = Surface area of the h.t. $[ft^2]$
S_{vt} = Surface area of the v.t. $[ft^2]$
V_D = Design dive speed $[KEAS]$
W_{ht} = Weight of the horizontal tail (h.t.) $[lb]$
W_{vt} = Weight of the vertical tail (v.t.) $[lb]$
z_{ht} = Distance from the v.t. root to where the h.t. is mounted on the v.t. $[ft]$
$\Lambda_{0.5c_{ht}}$ = Sweep angle at half of the h.t. chord $[deg]$
$\Lambda_{0.5c_{vt}}$ = Sweep angle at half of the v.t. chord $[deg]$

F.2.3. FUSELAGE GROUP

$$W_{fuselage} = 0.021 K_{fuselage} \sqrt{V_D l_h / \left(w_f + h_f\right)} (S_{fgs})^{1.2} \tag{F.6}$$

h_f = Fuselage height $[ft]$
K_f = 1.08 for pressurized fuselage $[-]$
= 1.07 for a main gear attached to the fuselage $[-]$
= 1.10 for a cargo aircraft with a cargo floor $[-]$
These effects are multiplicative for aircraft equipped with all of the above
l_h tail arm, distance between 0.25MAC of the h.t. to 0.25MAC wing $[ft]$
S_{fgs} = fuselage gross shell area $[ft^2]$
V_D = Design dive speed $[KEAS]$
w_f = Fuselage width $[ft]$
$W_{fuselage}$ = Fuselage weight $[lb]$

F.2.4. NACELLE GROUP

$$W_{ng} = 0.065 T_{TO} \tag{F.7}$$

T_{TO} = Take-Off thrust $[lb]$

NOTES

The nacelle weight is assumed to consist of the following components:

1. For podded engines: the structural weight associated with the engine external ducts and or cowls and pylon weight is included.
2. For propeller driven aircraft: the structural weight associated with special cowling and or ducting provisions (other than the inlet duct which is included in the air induction system under the power plant weight) and any special engine mounting provisions
3. The equation is valid for high bypass ratio turbo fan engines

F.2.5. LANDING GEAR GROUP

$$W_{lg} = K_{gr}\left(A_g + B_g(W_{TO})^{0.75} + C_g W_{TO} + Dg(W_{TO})^{3/2}\right) \tag{F.8}$$

K_{gr} = 1.0 for low wing; 1.08 for high wing

Airplane Type	Gear Type	Gear Comp.	A_g	B_g	C_g	D_g
Jet Trainers and Business Jets	Retr.	Main	33.0	0.04	0.021	0.0
		Nose	12.0	0.06	0.0	0.0
Other civil airplanes	Fixed	Main	20.0	0.10	0.019	0.0
		Nose	25.0	0.0	0.0024	0.0
		Tail	9	0.0	0.0024	0.0
	Retr.	Main	40.0	0.16	0.019	1.5×10^{-5}
		Nose	20.0	0.10	0.0	2.0×10^{-6}
		Tail	5.0	0.0	0.0031	0.0

Figure F.1: Constants in Landing Gear Weight Equation (F.8) [40]

NOTES

1. The constants for the landing gear weight equation can be determined with Figure F.1
2. It is assumed that the constants for other civil aircraft with a retractable landing gear are valid for turboprop aircraft.

F.3. POWERPLANT WEIGHT ESTIMATION

$$W_{power} = W_{engine} + W_{ai} + W_{propeller} + W_{fs} + W_{ps} \tag{F.9}$$

F.4. FIXED EQUIPMENT WEIGHT ESTIMATION

F.4.1. FLIGHT CONTROLS

$$W_{fc} = 0.64(W_{TO})^{2/3} \tag{F.10}$$

W_{TO} = Take-Off weight $[lb]$

NOTES

1. This result is multiplied with a factor of 1.2 in case of leading edge high lift devices are employed
2. This result is multiplied with a factor of 1.15 in case of lift dumpers are employed

F.4.2. HYDRAULIC/PNEUMATIC SYSTEM

$$W_{hps} = 0.0120 W_{TO} \tag{F.11}$$

W_{hps} = Weight of the hydraulic/pneumatic system $[lb]$
W_{TO} = Take-Off weight $[lb]$

F.4.3. ELECTRICAL SYSTEM

$$W_{hps} + W_{elec} = 0.325 W_E^{0.8} \tag{F.12}$$

W_E = Aircraft empty weight $[lb]$
W_{elec} = Weight of the electrical systems $[lb]$
W_{hps} = Weight of the hydraulic and pneumatic systems $[lb]$

F.4.4. INSTRUMENTATION, AVIONICS, AND ELECTRONICS

$$W_{iae} = 120 + N_e + 0.006 W_{TO} \tag{F.13}$$

N_e = Number of engines [−]
W_{iae} = Weight of the instrumentation, Avionics, and Electronics [lb]
W_{TO} = Take-Off weight [lb]

F.4.5. AIR-CONDITIONING, PRESSURIZATION, ANTI-ICE AND DE-ICE SYSTEMS

$$W_{api} = 6.75 (l_{pax})^{1.28} \tag{F.14}$$

l_{pax} = Length of the passenger cabin [ft]
W_{api} = Weight of the air-conditioning, pressurization, anti-ice, and de-ice systems [lb]
W_{TO} = Take-Off weight [lb]

F.4.6. OXYGEN SYSTEMS

The following equation is valid for aircraft with a flight level below 25000 ft.

$$W_{ox} = 20 + 0.5 N_{pax} \tag{F.15}$$

N_{pax} = Number of passengers [−]
W_{ox} = Weight of the oxygen system [lb]

F.4.7. FURNISHING

$$W_{fur} = 0.211 \, (W_{TO} - W_{Fuel})^{0.91} \tag{F.16}$$

W_F = Fuel weight [lb]
W_{fur} = Furnishing weight [lb]
W_{TO} = Take-Off weight [lb]

G

ATR42 Weight Breakdown by Obert

The table presented in this appendix shows the component masses of the ATR42, determined by Obert [73]. This data is used to compare the Class 2 Weight Estimation results of the ATR72-600 generated with the Initiator.

Table G.1: Weight breakdown of the ATR42 by Obert [73]

Item	*Weight [kg]*	*% MTOM*
Wing	1565	9.69
Fuselage	2587	
Horizontal tailplane	220	
Vertical tailplane	322	
Landing gear	534	
Engine nacelles	366	
Flight controls	195	
Structure	**5788**	**35.84**
Equipped engines	1212	
Engine controls	37	
Engine instrumentation	10	
Fuel system	89	
Propulsion	**1347**	**8.34**
Hydraulic generation	91	
Hydraulic distribution	50	
Air conditioning	287	
De-icing	75	
Fire protection	25	
Cockpit furnishing	79	
Auto-flight system	26	
Navigation	164	
Communication	94	
Electric generation	310	
Electric distribution	213	
Systems	**1414**	**8.76**
Furnishing	845	
Oxygen	31	
Lighting	90	
Water installation	11	
Furnishings	**977**	**6.05**
Manufacturer's Empty Weight	***9526***	***58.98***
Party structure	45	
Passenger seats	322	
Other standard items	34	
Standard items	**401**	**2.48**
Delivered empty mass	***9927***	***61.47***
Operational items	**326**	**2.02**
Operational empty mass (OEM)	***10253***	***63.49***
Maximum take-off Mass (MTOM)	***16150***	***100***

H

INITIATOR RESULTS

This chapter contains the exact results of all analysis done with the Initiator. All results are given for the harmonic range. The results are based on the main mission requirements, as provided in Table H.1:

Table H.1: Top level mission requirements for the harmonic mission, based on the ATR72-600 [37]

Parameter	Unit	Value
Payload mass (68 pax)	kg	7500
Range at max payload	km	1528
Design Cruise Altitude	m	7500
Design Cruise Mach	-	0.45

In Section H.1 the baseline results of the reference aircraft and the Initiator models of the ATR72-600 and DUUC are presented. The other sections in this appendix contain the results of the DUUC sensitivity analysis.

H.1. BASELINE RESULTS

Table H.2: Comparison of reference aircraft, and Initiator baseline models of the ATR72-600 and DUUC

		Reference	Initiator Baseline Models	
Parameter	**Unit**	**ATR72-600**	**ATR72-600**	**DUUC**
MTOM	kg	22800	22263	24774
OEM	kg	13311	13215	15526
Harmonic fuel	kg	1989	1548	1748
Harmonic fuel fraction	-	0.0872	0.0695	0.0705
Fuel efficiency	g/pax/km	19.1	14.9	16.8
Power loading	N/W	0.0606	0.0497	0.0504
Wing loading	N/m^2	3667	3792	3795
Engine T-O power	kW	3692	4399	4823
Wing surface area	m^2	61.0	57.6	64.1
Fan RPM	1/min	1200	1200	1500
$N_{\mathbf{bl}}$	-	6	6	8
M_{tip}	-	0.916	0.916	0.99
D_{fan}	m	3.93	3.91	3.48
$\overline{X}_{\text{LE}_{\text{wing}}}$	-	0.420	0.420	0.508

H.2. DUCT ASPECT RATIO

Table H.3: Effect of fan duct aspect ratio on the DUUC converged design

Parameter	Unit	DUUC Models				
		$AR = 1.5$ *exceeds fuselage*	$AR = 2.0$ *Baseline*	$AR = 2.5$	$AR = 3.0$	$AR = 3.5$ *Instable*
MTOM	kg	25283	24774	24515	24350	24196
OEM	kg	15952	15526	15309	15166	15028
Harmonic fuel	kg	1831	1748	1706	1684	1668
Harmonic fuel fraction	-	0.0724	0.0705	0.0696	0.0692	0.0689

H.3. MACH TIP NUMBER

Table H.4: Effect of fan tip Mach number on the DUUC converged design

Parameter	Unit	DUUC Models		
		$M_{tip} = 0.99$ *Baseline*	$M_{tip} = 0.95$	$M_{tip} = 0.90$ *Instable*
MTOM	kg	24774	24622	24407
OEM	kg	15526	15389	15198
Harmonic fuel	kg	1748	1733	1710
Harmonic fuel fraction	-	0.0504	0.0704	0.0700
D_{fan}	m	3.48	3.30	3.09

H.4. FAN RPM VARIATION

Table H.5: Effect of fan revolutions per minute on the DUUC converged design

Parameter	Unit	DUUC Models			
		RPM = 1400	RPM = 1500 *Baseline*	RPM = 1600	RPM = 1700 *Instable*
MTOM	kg	25025	24774	24572	24411
OEM	kg	15751	15526	15345	15206
Harmonic fuel	kg	1774	1748	1726	1708
Harmonic fuel fraction	-	0.0709	0.0504	0.0703	0.0700
D_{fan}	m	3.73	3.48	3.26	3.07

H.5. NUMBER OF FAN BLADES

Table H.6: Effect of number of fan blades on the DUUC converged design

Parameter	Unit	DUUC Models			
		$N_{bl} = 8$ *Baseline*	$N_{bl} = 6$	$N_{bl} = 4$	$N_{bl} = 3$
MTOM	kg	24774	24717	24643	24602
OEM	kg	15526	15473	15402	15363
Harmonic fuel	kg	1748	1744	1741	1739
Harmonic fuel fraction	-	0.0504	0.0705	0.0706	0.0707
$\overline{X}_{LE_{wing}}$	-	0.508	0.507	0.506	0.505
$\Delta\overline{X}_{LE_{wing}}$	-	0.0135	0.0041	0.0144	0.0149

H.6. TAKE-OFF PROPULSIVE EFFICIENCY

Table H.7: Effect of propulsive take-off efficiency on the DUUC converged design

Parameter	Unit	DUUC Models		
		η_{TO} = 0.80 *Baseline*	η_{TO} = 0.75	η_{TO} = 0.70 *Same as reference*
MTOM	kg	24774	24775	24776
OEM	kg	15526	15527	15526
Harmonic fuel	kg	1748	1748	1750
Harmonic fuel fraction	-	0.0695	0.0706	0.0706

H.7. TAKE-OFF DISTANCE

Table H.8: Effect of design take-off distance on the DUUC converged design, with $\eta_{prop}TO = 0.80$

Parameter	Unit	DUUC Models		
		s_{TO}=1333m *Baseline*	s_{TO}=1150m	s_{TO}=1000m
MTOM	kg	24774	25041	25977
OEM	kg	15526	15733	16435
Harmonic fuel	kg	1748	1808	2042
Harmonic fuel fraction	-	0.0705	0.0722	0.0786
Power loading	N/W	0.0504	0.0482	0.0417
Wing loading	N/m^2	3795	3800	3821
Engine T-O power	kW	4823	5096	6113
Wing surface area	m^2	64.1	64.7	66.7

H.8. PROPULSION WEIGHT FACTOR

Table H.9: Effect of propulsion weight correction factor the DUUC converged design

Parameter	Unit	DUUC Models				
		PWF = 1.75 *Instable*	PWF = 1.50	PWF = 1.00 *Baseline*	PWF = 0.75	PWF = 0.50
MTOM	kg	26781	26111	24774	24189	23562
OEM	kg	17390	16766	15526	14974	14387
Harmonic fuel	kg	1891	1845	1748	1715	1676
Harmonic fuel fraction	-	0.0706	0.0707	0.0705	0.0709	0.0711
Fuel efficiency	g/pax/km	18.2	17.8	16.8	16.1	16.5

H.9. ENGINE LONGITUDINAL LOCATION

Table H.10: Effect of fan tip Mach number on the DUUC converged design

Parameter	Unit	DUUC Models		
		$\overline{X}_{eng}$ = 0.839 *Baseline*	$\overline{X}_{eng}$ = 0.800	$\overline{X}_{eng}$ = 0.739 *Instable*
MTOM	kg	24774	24189	23562
OEM	kg	15526	14974	14387
Harmonic	kg	1748	1715	1676
Harmonic fuel fraction	-	0.0705	0.0709	0.0711
$\overline{X}_{LE_{wing}}$	-	0.508	0.504	0.490

H.10. IDEAL AIRCRAFT

Table H.11: Effect of ideal propulsive efficiency η_{prop} = 1.0 with a super lightweight duct design with W_{duct} =0kg

		Initiator Ideal Aircraft	
Parameter	**Unit**	**ATR72-600**	**DUUC**
MTOM	kg	21639	22692
OEM	kg	12830	13780
Harmonic fuel	kg	1309	1413
Harmonic fuel fraction	-	0.0605	0.0622